OCCLUSIVE ARTERIAL THROMBOSIS AND THROMBOLYSIS

A Dissertation
Presented to
The Academic Faculty

by

Dongjune A. Kim

In Partial Fulfillment
Of the Requirements for the Degree
Doctor of Philosophy in Mechanical Engineering

Georgia Institute of Technology
Dec 2020

OCCLUSIVE ARTERIAL THROMBOSIS AND THROMBOLYSIS

Approved by:

Dr. David N. Ku, Advisor
George W. Woodruff School of Mechanical Engineering
Georgia Institute of Technology

Dr. Jorge Di Paola
Pediatrics
Washington University School of Medicine in St.Louis

Dr. Andrés J. García
George W. Woodruff School of Mechanical Engineering
Georgia Institute of Technology

Dr. Keith Neeves
Bioengineering and Pediatrics
University of Colorado

Dr. Yuhang Hu
George W. Woodruff School of Mechanical Engineering
Georgia Institute of Technology

Date Approved: Dec 4, 2020

To my parents

ACKNOWLEDGEMENTS

It is surprising that it has already been more than four years since I started the Ph.D. program at Georgia Tech. As a mechanical engineer from industry, I had certain expectations and goals when I entered the program. Initially, I considered the Ph.D. program an extended version of the master's program and, in my case, a chance to change focus from mechanical engineering to bioengineering. However, my experience throughout the program has been so much more than what I expected. Of course, the journey was not an easy one. I know that I couldn't have come this far without great lab mates, collaborators, friends, and family support, as well as an excellent advisor.

Before joining the Ku lab, my career had nothing to do with bioengineering nor thrombosis. I still remember being so confused by similar words like thrombus, thrombi, and thrombosis, which are now very familiar. However, under Dr. Ku's guidance, I was able to make a smooth transition into the field of bioengineering and thrombosis. Dr. Ku has made this journey very special, not only by providing various perspectives on my Ph.D. project as a clinician, scientist, mechanical engineer, bioengineer, and entrepreneur but also by encouraging me to think about how science advances. He recommended books such as *The Beginning of Infinity* and *The Structure of Scientific Revolutions*, which inspired me to think about current science as a part of big paradigm shifts. His way of advising and motivating students was also amazing, and I took notes just in case I have a chance to mentor someone in the future. I continue to learn so much from him and know that I will retrace his lessons in the future. I would also like to give a special thanks to Seungman Park, who introduced me to Dr. Ku and the Ku lab.

The Ku lab members – Susan, Joav, Michael, Chris, Leo, Britt, Qing, Patricia, Viviana, and Gian – also helped me adapt to the field of bioengineering. For me, this adaption involved not only learning about the field but also how to perform experiments. In my previous work, I had primarily conducted simulations rather than experiments, and I learned a significant amount from Susan and Michael. The reader of this thesis will be surprised to find out that most of it is experimental work. Discussions with Chris and Leo gave me new insights and questions that motivated me to think in depth.

Outside the Ku lab, I was very fortunate to have excellent collaborators: Katrina, Dr. Di Paola, Dongjing, and Dr. Hu. Certainly, there is a limit to how much one person can do with a restricted timeframe. However, through them, I expanded my knowledge and interests. I would also like to thank the IBB facility managers who taught me to use a variety of equipment – Aqua, Laxmi, Andrew, and Yolande. As I needed blood to work on my thesis, I visited the abattoir regularly, and I am particularly thankful to Hollifield farm and Riverview farm for giving an extra effort to provide porcine blood.

Stress can occur for many reasons including a Ph.D. degree, and it is very important to learn how to be relax and relieve stress. In my case, I played sports to blow off steam. I am grateful to GTKSA basketball, ALTA tennis, and Peach climbing members who gave me lasting memories.

Last but not least, I am grateful to my younger brother, my parents, and my wife. People around me always asked me about the fancy shoes I was wearing, and I had to say that they are all from my younger brother, Dongsoo. I really feel sorry but appreciative that he was left to take care of my parents while I was abroad. My parents, the biggest

supporters of this study, pushed and motivated me to challenge this research. It is inspiring to realize how much my parents, especially my farther, care about raising an engineer and advancing science. Thinking back on it now, there are few people like my father. I hope that my parents like what they read here. Finally, I would like to thank my wife, Dayeon, who married me this summer and has supported me throughout a rough period this year. Especially over the last few months, she must have had a hard time bearing with me. I am looking forward to beginning the next chapter of our lives together.

TABLE OF CONTENTS

LIST OF TABLES

LIST OF FIGURES

downstream of the elongated thrombus colored in gray. (D) Shear strain rate around the thrombus. A maximum shear of 15,000 s^{-1} (red) was observed in the throat of stenosis. (E) Drag force acting on the thrombi surface. The thrombus 2 fragment experiences a maximum force of > 4 nN.

LIST OF SYMBOLS AND ABBREVIATIONS

a	Arterial thrombosis model constant
A	Clot cross sectional area
ADAMTS13	A Disintegrin and Metalloproteinase with a Thrombospondin Type 1 Modtif, Member 13
ANOVA	Analysis of variance
b	Arterial thrombosis model constant
c	Arterial thrombosis model constant
CFD	Computational Fluid Dynamics
d	Arterial thrombosis model constant
D	Channel diameter
DAQ	Data Acquisition System
Δ	Differential
DI	Deionized
DiNAC	N, N'-diacetyl-L-cystine
d_p	Pore channel diameter
ε	Porosity
F	Force
FDA	Food and drug administration
FE	Finite element
FSI	Fluid structure interaction
FV	Factor V
FVIII	Factor VIII
GPS	Gray platelet syndrome

GT45	Stenosed glass tube
GT85	Stenosed glass capillary tube
h	Channel height
H&E	hematoxylin and eosin
ID	Inner diameter
IV	Intravenous
IVC	Inferior Vena Cava
J	Platelet accumulation rate
J_{MIN}	Minimum platelet accumulation rate
J_{AVG}	Average platelet accumulation rate
J_{MAX}	Maximum platelet accumulation rate
κ	Permeability
k_{on}	Kinetic on rate
L	Clot length
μ	Viscosity
NAC	N-acetylcysteine
Nbeal2	neurobeachin-like 2 gene
Nbeal2$^{-/-}$	neurobeachin-like 2 gene knock-out
n_p	Number of channels
MC98	Microfluidic chamber
P	Pressure
Pa	Pressure upstream
Pb	Pressure downstream
PF	Platelet factor
PBS	Phosphate-buffered saline

PDMS	Polydimethylsiloxane
PRP	Platelet-rich plasma
Q	Flow rate
RBC	Red blood cell
ROI	Region of interest
Rc	Hydraulic resistance by permeable clot
R_p	Hydraulic resistance by pore channel
S	Wall shear rate
SEM	Scanning electron microscope
SEOM	Standard error of mean
SIPA	Shear induced platelet aggregation
τ	Stress
τ_{MAX}	Maximum stress
t_{Lag}	Lag phase time
TEG	Thromboelastography
tPA	Tissue plasminogen activator
ULVWF	Ultra-long VWF
v	Superficial velocity
VWF	von Willebrand Factor
w	Channel width
WB	Whole blood
WBC	White blood cell
WT	Wild type

SUMMARY

Occlusive arterial thrombosis in a stenotic vessel can cause the cessation of blood flow to the brain or heart, which can result in a patient's death. Following the incident, the patient may be given a thrombolytic agent or undergo a thrombectomy to recanalize the occluded vessel and to regain blood flow. The current standard for thrombolytic treatment involves the administration of tissue plasminogen activator (tPA), which has shown limited efficacy and creates a bleeding risk.

An arterial thrombus differs from a venous thrombus in terms of both its mechanism of formation and composition. The von Willebrand Factor (VWF)-platelet-rich arterial thrombus forms by shear induced platelet aggregation (SIPA), and can occlude the vessel in harsh hemodynamic environments consisting of high shear rates and high blood pressure. It is critical to know what key factors affect the formation of occlusive SIPA clots, how these clots stabilize under arterial conditions, and which agents should be used for a lysis. The overall goal of this thesis is to investigate these three important aspects of arterial thrombosis formed under a pathological high shear.

VWF is a protein that plays a critical role in forming SIPA clots under high shear conditions. Platelet α-granules contain 50 times more concentrated VWF compared to plasma VWF. The role of α-granules in forming occlusive arterial thrombi was studied using *Nbeal2*$^{-/-}$ mice that do not release α-granules. Without α-granule release, there was no rapid platelet accumulation and no subsequent channel occlusion occurred. Thus, α-granules could be a potential new target for the prevention of arterial thrombosis.

An occlusive SIPA clot formed with α-granule release was VWF-platelet-rich. SIPA clots formed using arterial-like hemodynamic conditions *in vitro* were compared to coagulation clots generated under static conditions. SEM images of the SIPA clot revealed densely packed platelets, which can be converted into 1.23 billion platelets in the total clot. Histological images showed distinctive structural features that were different upstream, near the apex, and downstream of the stenosis. The upstream region showed mountain-like platelet aggregates protruding to the central lumen that left a large hole in the center, while RBCs trapped in valleys. Near the apex, a uniformly dense platelet mass formed throughout the lumen to fully occlude the channel. In the upstream part of the occlusive mass, platelets were amorphous consistent with activation. In the downstream part of the mass, spherical platelets dominated, consistent with no activation. The thrombus ended abruptly in the expansion past the throat of the stenosis and did not extend to the walls located in the flow separation zone. Measurements of pressure and flow could be used to characterize the SIPA clot as three orders of magnitude more permeable than a coagulation clot. However, although the SIPA clot was more porous and permeable, it was two times stiffer and seven times stronger than the coagulation clot, which would make it capable of occluding a stenosed coronary artery within a 2-mm clot length.

Different types of clots may require different thrombolytic agents for lysis and vessel recanalization. Five different thrombolytic agents were tested on SIPA and coagulation clots in an *in vitro* model. A fibrinolytic agent, tPA lysed the coagulation clots but not the SIPA clots. Meanwhile, a novel thrombolytic agent, N,N'-Diacetyl-L-cystine (DiNAC) significantly lysed the SIPA clots without dissolving the coagulation clots.

The results of this study may lead to the development of a new antithrombotic agent that inhibits formation or release of VWF from α-granules of platelets, thrombectomy devices that account for SIPA clot permeability and strength, and a new thrombolytic treatment using DiNAC.

CHAPTER 1. INTRODUCTION

1.1 Arterial Thrombosis

Acute arterial thrombosis is a pathological condition where a blood clot forms in a stenotic artery. The clot can interrupt or even stop the blood flow once the clot becomes occlusive. Occlusive arterial thrombosis in a carotid or coronary artery can result in an ischemic stroke or myocardial infarction, which are the leading causes of death worldwide (Adams, 2003; Xu, Murphy, Kochanek, & Arias, 2020).

Arterial thrombosis begins with plaque development in the arteries, which takes place over many decades via the process of atherosclerosis. The plaque narrows the lumen of the vessel, generating a stenosis. The stenotic region can have wall shear rates ranging from 5,000 to 400,000 s^{-1}, which are much higher than the typical shear rates of $< 1{,}000\ s^{-1}$ in arteries (Bark Jr & Ku, 2010; Shaun P Jackson, 2007). At a certain point, a plaque-cap rupture occurs, and the endothelial cell layer can be disturbed to expose its pro-thrombogenic collagen surface (Davies & Thomas, 1985). The collagen layer provides a surface for the von Willebrand Factor (VWF) to tether to and elongate, and for platelets to adhere to and aggregate (Santoro, 1981; Savage, Ginsberg, & Ruggeri, 1999). Platelet aggregation under such a high shear rate is called shear-induced platelet aggregation (SIPA), which results in an occlusive blood clot formation in under an hour and cessation of the blood flow in the arteries (Casa, Deaton, & Ku, 2015).

1.2 The Mechanism of SIPA Clot Formation

It is counter-intuitive as to how SIPA occurs under such pathologic high shear rates of 400,000 s^{-1}, as this generates a very strong hydrodynamic force that acts on the platelets and platelet aggregates. The magnitude of this hydrodynamic force acting on the platelets exceeds 10,000 pN (Wellings & Ku, 2012), resulting in harsh flow conditions for the formation of SIPA clots. Not only do SIPA clots need to overcome such a severe flow conditions, they also need to accumulate billions of platelets to occlude an artery. Histology studies have demonstrated that SIPA clots consist of approximately 80% platelets by volume (Ku & Flannery, 2007), and billions of platelets must be captured to occlude an artery with a diameter > 4 mm (Mehrabadi, Casa, Aidun, & Ku, 2016). These clot-formation conditions can be achieved via VWF elongation under high shear rates and rapid platelet accumulation (RPA) via a positive feedback loop suggested by Casa and Ku (2017).

After the rupture of the plaque cap, the collagen surface is exposed to the blood flow, and marginated soluble VWF can bind to fibrillar collagen type 1 or 3 through the A3 domain, mediated by the A2 domain (Rack et al., 2017; Sakariassen, Houdijk, Sixma, Aarts, & de Groot, 1983; Wei et al., 2018). The adsorption of the VWF onto the collagen-coated surface can be enhanced with higher molecular weight VWF (Santoro, 1981), and those shear rates above 5,000 s^{-1} can unfold the VWF molecule (Schneider et al., 2007). The VWF then becomes the dominant molecule that mediates platelet binding for shear rates over 1,000 s^{-1} (Aarts, Steendijk, Sixma, & Heethaar, 1986). The VWF can bind to platelets via glycoprotein Ib-A1 (GPIb-A1) without activation or via integrin GPIIb/IIIa-C1 post-activation (Ruggeri, Orje, Habermann, Federici, & Reininger, 2006). The high

shear rate leads to not only to VWF margination but also to platelet margination, where the hematocrit and shear rate can increase the platelet concentration near the vessel wall by as much as 2.5 folds (Aarts et al., 1988). The marginated platelets can be captured by the VWF at the vessel wall, but the high wall shear rate only allows microseconds for the platelets to react with the surface (Wellings & Ku, 2012). Based on the platelet activation curve given by Hellums (1994), microseconds are not sufficient for platelets to activate. In addition, Ruggeri et al. (2006) found that SIPA clots form without platelet activation when shear rates exceed 10,000 s^{-1} and when soluble VWF is present. Thus, it is platelet activation-redundant GPIb-A1 binding that is important for the SIPA clot formation under pathological high shear rates (Casa & Ku, 2017).

GPIb is a glycoprotein receptor on the membrane of unactivated platelets that can bind to the VWF A1 domain (Ruggeri et al., 2006). A single GPIb-A1 bond has a strength of approximately 100 pN; thus, there needs to be more than 1,000 bonds under large hydrodynamic forces exceeding 10,000 pN (Tadayuki Yago et al., 2008). Wellings and Ku (2012) demonstrated how many bonds and how fast the binding should be, to capture a platelet under a high shear rate. To form more than 1,000 bonds, the VWF needs to unfold and create a VWF net via self-association to expose the abundant A1 domains. In order to generate VWF nets, a localized high VWF concentration is required via α-granule release from activated platelets. α-granules have a 50-times higher VWF concentration than plasma VWF does (Harrison & Cramer, 1993). Wellings and Ku (2012) concluded that the VWF must bind platelets with a kinetic on-rate (k_{on}) ranging from 10^5 to 10^9 $\mathrm{M^{-1}s^{-1}}$, theoretically. Single VWF molecule studies by Fu et al. (2017) confirmed that the k_{on} of platelets to VWF A1 is greater than 10^6 $\mathrm{M^{-1}s^{-1}}$, experimentally.

After the initial platelet capture, the adhered platelets can be activated to form integrin GPIIb/IIIa-C1 bonds for a stable clot formation. Subsequently, these activated platelets release molecules such as α-granules and dense granules that contain procoagulant molecules: ultra-large VWF (ULVWF), fibrinogen, platelet factor 4 (PF4), thrombospondin, factor V (FV), factor VIII (FVIII), ADP, ATP, serotonin, and calcium. The release of ULVWF creates another reactive surface for more platelet capture on the surface. A repeat of this process results in a positive feedback loop for RPA (Figure 1-1) that recruits billions of platelets into the stenosis.

In summary, occlusive thrombus formation under high shear rate conditions can be described as a three-phase process of (i) initial platelet attachment to a thrombogenic surface (lag phase); (ii) accelerated growth (RPA); and (iii) thrombus stabilization or cessation of blood flow (occlusion phase) (Casa & Ku, 2017). This whole process is summarized in Figure 1-1.

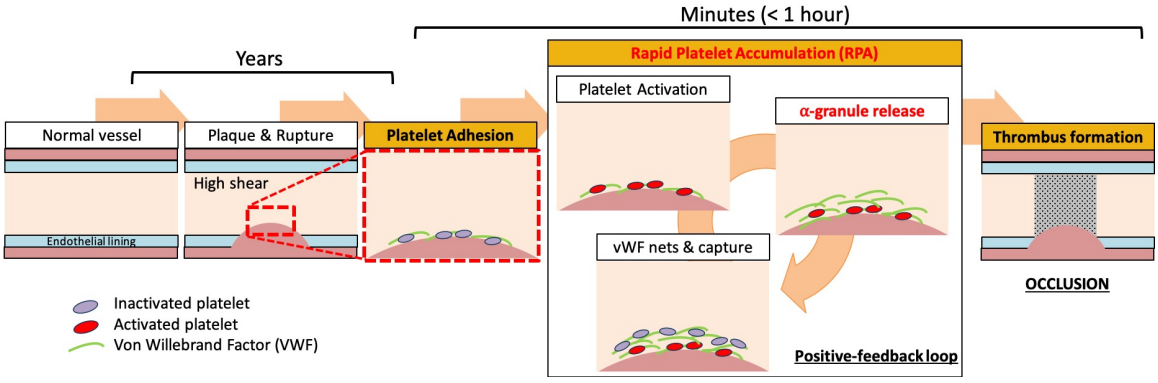

Figure 1-1. Mechanism for high-shear arterial thrombosis.

1.3 Coagulation Clots and SIPA Clots

The mechanism for SIPA clot formation is different from the classic Virchow's triad of coagulation-based red clotting (Figure 1-2). Virchow's triad consists of endothelial disruption, stagnant blood flow, and hypercoagulability (Lefkowitz, 2008). In contrast to Virchow's triad, Casa et al. (2015) suggest an alternative triad necessary for arterial thrombosis: (i) a collagen surface or other substrate for initial VWF absorption, (ii) a pathologically high shear rate for VWF unfolding and elongation, and (iii) platelets and VWF in sufficient concentrations (Figure 1-2).

Due to the distinct formation mechanisms, coagulation clots and SIPA clots are composed of different constituents. The main component of a coagulation clot is fibrin, which is a final product of the coagulation cascade that entraps large amounts of Red Blood Cells (RBCs). The prevalence of RBCs in coagulation clots is the reason why such clots appears to be red, and are often referred to as "red clots." (Cadroy, Horbett, & Hanson, 1989). However, a coagulation clot can be white if the clot is formed from artificially extracted platelet-rich plasma (PRP) that lacks RBCs but is still fibrin-abundant. On the contrary, a SIPA clot consists mostly of platelets and VWFs, as Ku and Flannery (2007) found that 80% of SIPA clot consisted of platelets. Due to the relative absence of RBCs and the prevalence of platelets, SIPA clots appear to be white and are commonly called "white clots." (Narins & Topol, 1997).

Another distinctive factor to distinguish between a coagulation clot and a SIPA clot is the hemodynamic condition – the shear rate (Figure 1-2). The shear rate in a vessel can be defined as the velocity gradient along the vessel's diameter. Cadroy et al. (1989) showed

that SIPA clots form under high shear rates, whereas coagulation clots are created in low-shear regions. These differences in the hemodynamic conditions for clot formation can be used to predict the location of the formation based on the shear rate. Coagulation clots will likely form in the low shear regions of venous system or in stagnant regions of medical devices (Susan M. Hastings, Deshpande, Wagoner, Maher, & Ku, 2016), whereas SIPA clots form in the arterial system or in high-shear regions of medical devices.

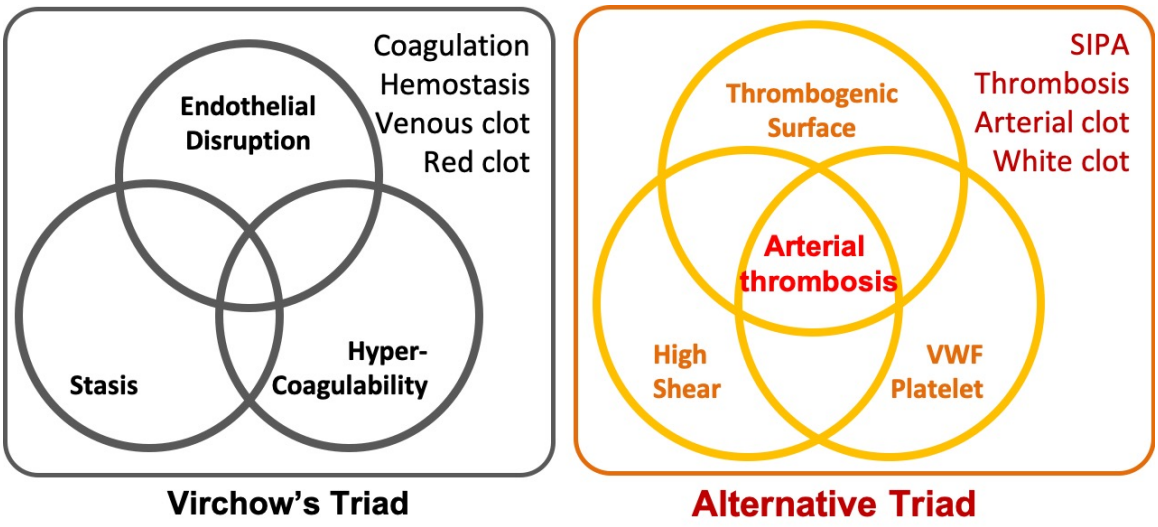

Figure 1-2. Essential triads for coagulation and SIPA clot formation.

1.4 Treatments for Arterial Thrombosis

The main goal of arterial thrombosis treatment is to regain the blood flow by removing the occlusive thrombus. Currently, there are two types of treatments available in the clinical field: thrombolytic therapy and a thrombectomy. Thrombolytic therapy is a chemical

method for removing the thrombus by administrating a lysis agent, for instance, intravenous (IV) tissue Plasminogen Activator (tPA). On the other hand, a thrombectomy utilizes mechanical forces to retrieve the thrombus from an artery (Figure 1-3).

tPA is the only Food and Drug Administration (FDA) approved thrombolytic agent in the United States (Chapman et al., 2014). Astrup and Permin (1947) first discovered tPA, and it was tested with different types of *in vitro* assays: a fibrin plate (Astrup & Müllertz, 1952) and a circulating plasma system (Matsuo, Rijken, & Collen, 1981a). Success in the *in vitro* assays led to multiple *in vivo* studies (Matsuo, Rijken, & Collen, 1981b), a small clinical study (Bergmann, Fox, Ter-Pogossian, Sobel, & Collen, 1983), and large clinical trials (Collen et al., 1984; The GUSTO Angiographic Investigators, 1993; The GUSTO Investigators, 1993). However, patients must receive treatment within a small-time window of 3 hours from the onset of symptoms, and many individuals have contraindications, such as a recent surgery or bleeding (Bivard, Lin, & Parsonsb, 2013; Prabhakaran, Ruff, & Bernstein, 2015). tPA has been shown to have a limited recanalization rate of less than 30% (Bhatia et al., 2010). In addition, a 30% relative risk reduction was found versus the placebo in stroke patients who had tPA administrated, but ultimately, there was no statistically significant improvement in the overall mortality rate with the use of tPA (Chapman et al., 2014). tPA induces the conversion of plasminogen to its active form, plasmin, in the vicinity of a hemostatic plug. Plasmin then cleaves fibrin, thus lysing the thrombus (Bivard et al., 2013; Brenner, 1988). However, thrombi that cause an arterial occlusion are not fibrin-rich, and thus tPA may not be effective in this environment. SIPA clots in arteries are structurally very different from a fibrin gel (Ku & Flannery, 2007).

In order to undertake a thrombectomy, the occlusion site needs to be located first and then a clinician can use a catheter to reach the thrombi. There are many thrombectomy devices on the market, but mainly, there are two types: wire-based devices and aspiration devices (Raychev & Saver, 2012). Wire-based devices (e.g., a coil retriever and stent retriever) poke or wrap the thrombi and then retrieve it into the catheter using frictional force. Meanwhile, aspiration thrombectomy devices use suction force to break and retrieve thrombi. Saver et al. (2015) found in their clinical study (39 centers and 196 patients) that a patient group who had stent retriever with tPA showed 88% recanalization rate and rate of functional independence at 90 days was higher compared to a group who had only tPA (60% vs. 30%, $p < 0.001$). Flynn et al. (2017) did a meta-analysis of eight thrombectomy clinical trials (1,841 patients) and found no significant effect on mortality at 90 days or symptomatic intracranial hemorrhage.

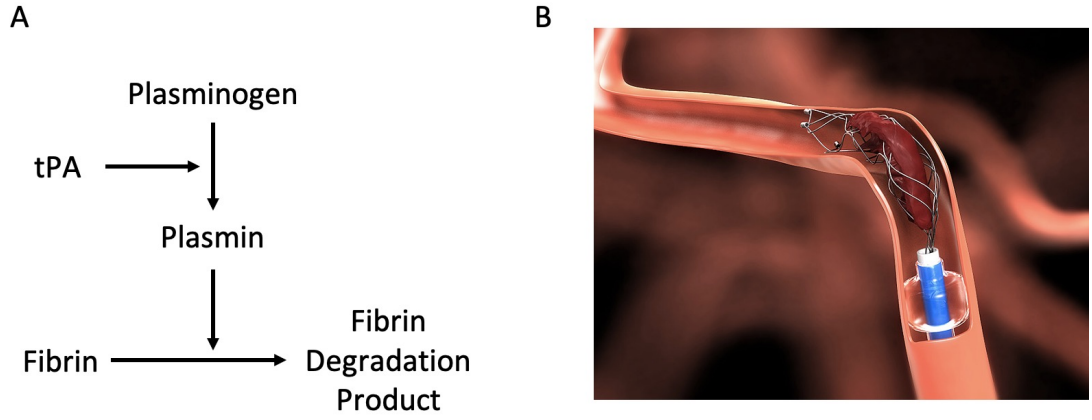

Figure 1-3. (A) Thrombolytic therapy using tPA. (B) thrombectomy device retrieving a blood clot.

CHAPTER 2. CRITICAL ROLE OF α-GRANULES FOR ARTERIAL THROMBOSIS

2.1 Introduction

Mehrabadi et al. (2016) have identified three phases for the SIPA process: (i) a lag phase with limited platelet attachments to the thrombogenic surface, (ii) RPA via explosive platelet aggregation, and (iii) post-occlusion that involves clot stabilization or embolization. During the RPA phase, billions of platelets must be captured onto the thrombogenic surface while traveling through the stenosis in microseconds and under a high hydrodynamic force of over 10,000 pN. Wellings and Ku (2012) used a theoretical analysis to predict that a fast-moving platelet can only be captured only if the VWFs are of sufficient concentration to form many multiple bonds as concave nets and where the k_{on} is greater than $10^8\ M^{-1}s^{-1}$. This analysis suggests that the plasma VWF concentration would be insufficient to capture the large number of platelets needed for RPA. Thus, a source of local VWF would be necessary for RPA and the subsequent occlusive thrombosis.

Such a local source might be the α-granules in platelets, as they contain ULVWF (Fernandez, Ginsberg, Ruggeri, Batlle, & Zimmerman, 1982; Moake, Turner, Stathopoulos, Nolasco, & Hellums, 1988). The α-granule is composed of secretory vesicles inside platelets that contains VWF, thrombospondin, fibronectin, and FV (Whiteheart, 2011). The VWF is the dominant protein that mediates platelet aggregation and thrombosis under pathologically high shear rates (Kim, Bresette, Liu, & Ku, 2019). Coagulation factors are prone to being transported away from the stenosis before the coagulation cascade is completed. However, there are studies showing fibronectin can play a role in platelet

aggregation and thrombus growth under high shear rates (S. P. Jackson, 2007). However, fibronectin concentration in α-granules (0.19 mg/mL) is smaller than the plasma concentration is (0.30 mg/mL) (Harrison & Martin Cramer, 1993), which, in turn, implies a lesser effect is expected on thrombosis in the absence of α-granules. The VWF inside the α-granule has a 50-fold higher concentration than plasma VWF does (Harrison & Martin Cramer, 1993) and is capable of mediating platelet aggregation under high shear rates of 120 dyne/cm^2 (Moake et al., 1988). Platelets release the contents of their α-granules upon activation, which may be stimulated by the high-shear stress or by thrombin. The α-granule may be necessary for RPA, and thus may be a target via which to prevent subsequent occlusive thrombosis. While Wellings and Ku (2012) hypothesized the criticality of the α-granule VWF, to best of the author's knowledge, this has not yet been tested experimentally.

The neurobeachin-like 2 gene (*Nbeal2*)-deficient mouse has been linked to the Gray Platelet Syndrome (GPS) (Albers et al., 2011; Deppermann, Nurden, Nurden, Nieswandt, & Stegner, 2013), which is a rare autosomal-recessive platelet disorder characterized by thrombocytopenia, large gray platelets lacking α-granules, and moderate bleeding. The *Nbeal2* knock-out (*Nbeal2*$^{-/-}$) mouse lacks the α-granule VWF but has a normal plasma VWF level compared to the wild type (WT) (Deppermann, Cherpokova, et al., 2013; Kahr et al., 2013). This difference is exploited in the *Nbeal2*$^{-/-}$ murine model to study the importance of α-granules on the high-shear thrombosis. Kahr et al. (2013) studied the platelet function of *Nbeal2*$^{-/-}$ and found less platelet aggregation compared to the WT in *in vitro* assays with a defect in thrombus formation using a laser-injury cremaster arteriole model. However, they only monitored the blood flow in the arteriole for a limited time of

3 min and no occlusion was found in the vessel. Deppermann, Cherpokova, et al. (2013) showed a similar defect in platelet aggregation and thrombus formation in *Nbeal2*$^{-/-}$. They used two different *in vivo* arterial thrombosis models: a ferric-chloride injury mesenteric arteriole model and a mechanically injured abdominal aorta murine model. Unstable or no occlusive thrombosis was found in *Nbeal2*$^{-/-}$ mice, whereas the WT showed full occlusion. Neither study took into account pathologically high shear rates, and they only tested under physiological arterial shear conditions (1,700 s^{-1} at maximum), which would not force the need for α-granule VWFs.

This study aims to investigate the effect of α-granule VWF presence on the occlusive thrombosis by creating pathological high-shear conditions and using *Nbeal2*$^{-/-}$ mice. First, we predict the occlusion time with normal whole blood (WB); with platelets with no α-granules (*Nbeal2*$^{-/-}$ platelets); and then we test a rescue situation where normal platelets are perfused after *Nbeal2*$^{-/-}$ platelets are. Experimental thrombotic occlusion is tested in a stenotic microfluidic system, that is optimized for the small blood volumes from mice where rescue is possible. Lastly, we test for occlusion in mice by suturing the carotid artery until the flow rate reaches 50% of the baseline. The resulting *in vivo* thrombosis was measured by flow rate and histological analysis. The study then compares the *in vitro* and *in vivo* quantitative data against the *in silico* predictions as a rigorous test of our hypothetical mechanism.

2.2 Methods

2.2.1 Computational Fluid Dynamics analysis

Computational fluid dynamics (CFD) were used to predict the shear-rate distribution within a microfluidic geometry and a mice carotid artery geometry. Simulations were performed using Ansys 19.1 (Ansys Inc, PA, USA). Whole blood flow was assumed to be Newtonian fluid of 3.5 cP, and the flow was presumed to be laminar, incompressible, steady, on a continuum, and isothermal due to the low Reynolds number in the experiments. The microfluidic chamber was modeled as a rectangular channel with a total pressure inlet of 4.8 mmHg and a uniform zero pressure (gage) outlet. The no-slip boundary condition was applied to the walls (Figure 2-3A). A stenosed mouse carotid artery had inner diameter (ID) of 0.45 mm and was modeled as a 60%-diameter constriction of a cylindrical vessel and a 0.25 mL/min flow rate was applied at the inlet with a zero pressure at the outlet (Figure 2-3B). Mesh convergence was achieved at 3.5 million and 4 million tetrahedral cells, yielding a residual error of 10^{-9} for each model, respectively.

2.2.2 Arterial thrombosis model for simulating the occlusion time

Time to occlusion in a stenotic microfluidic test section or mouse carotid artery was predicted using the quantitative, empirical, high-shear thrombosis model by Mehrabadi et al. (2016). The model is composed of a lag phase and RPA phase that are defined by:

$$t_{Lag} = 1.69 \times 10^{6} S^{-1.2} \quad (1)$$

where t_{Lag} is the lag time and S is the wall shear rate. The thrombus growth rate during the RPA phase is expressed by the time and shear rate (S).

$$J = \begin{cases} 0 & , t \leq t_{Lag} \\ ae^{bS} + ce^{dS}, & t > t_{Lag} \end{cases} \quad (2)$$

The constants *a, b, c*, and *d* are given in Table 1. The lower and upper confidence limits of thrombus growth are denoted by J_{MIN} and J_{MAX} respectively.

Table 1. Constants for the RPA phase thrombus growth-rate equation.

	a	*b* ($x10^{-4}$)	*c*	*d* ($x10^{-6}$)
J_{MIN}	-28.3	-1.00	27.4	-10.0
J_{AVG}	-31.3	-1.45	30.7	-6.81
J_{MAX}	-38.2	-1.81	36.6	-5.92

Our high-shear microfluidic device was modeled as a straight rectangular channel. Poiseuille flow was assumed and the shear rate, *S*, was defined by:

$$S_{Rec} = \frac{6Q}{wh^2} \quad (3)$$

The constants *Q*, *w*, and *h* are the flow rate, channel width, and channel height respectively. The geometry values are specified in Figure 2-3.

To model the stenosis of the mouse carotid artery, a 60%-diameter stenosis was applied to a cylindrical channel to cause an approximately 50% reduction in flow rate (Bark Jr & Ku, 2010). The assumptions of Poiseuille flow were applied at the throat, and the shear rate was defined by:

$$S_{Cir} = \frac{32Q}{\pi D^3} \quad (4)$$

where the constants Q, w, and h are the flow rate, channel width, and channel height, respectively, and D denotes the channel diameter.

The channel height/diameter was updated every second as thrombus growth increased in both models.

2.2.3 Mice

Nbeal2$^{-/-}$ and WT control mice were generated from *Nbeal2*$^{+/-}$ mice on a C57/bl6 background (Deppermann, Nurden, et al., 2013) with a targeted deletion region between exons 4-11 of *Nbeal2* (B6;129S5-*Nbeal2tm1Lex*/Mmucd) (Kahr et al., 2013). Equal numbers of 12~20-week-old male and female mice were used. All animal experiments were approved by the university animal care and use committees.

2.2.4 High-shear microfluidic stenosis model

Polydimethylsiloxane (PDMS) microchannels with a stenotic region were used for *in vitro* studies of WB occlusion at the pathological shear rate (Casa, Gillespie, Meeks, & Ku, 2016). Approximately 1~2 mL of blood can be drawn from mouse; thus, microfluidic set-up was optimized to use minimal blood for each run. Previous set-up required 6 mL of blood for each run, but by removing tubes and directly connecting reservoir to the inlet, necessary blood volume is reduced to 1.5 mL for the current set-up (Figure 2-1). WB was collected from the inferior vena cava (IVC) of the *Nbeal2*$^{-/-}$ and WT mice into heparin anticoagulant (15 USP/mL), and the platelets were fluorescently labeled with $DIOC_6$

(Invitrogen, CA, USA). WB was perfused through the microfluidic device at a constant upstream pressure head of 65 mmHg on immobilized type-1 fibrillar collagen (Chronolog, PA, USA). Platelet adhesion and occlusion were captured in real time with an ORCA Flash4 CMOS camera (Orca-ER, Hamamatsu, Japan) and CellSens software (Olympus, PA, USA) with images being acquired every 1 s for the duration of the experiment. The occlusion time was defined for each series when the centerline RBC velocities decreased to less than 100 μm/s.

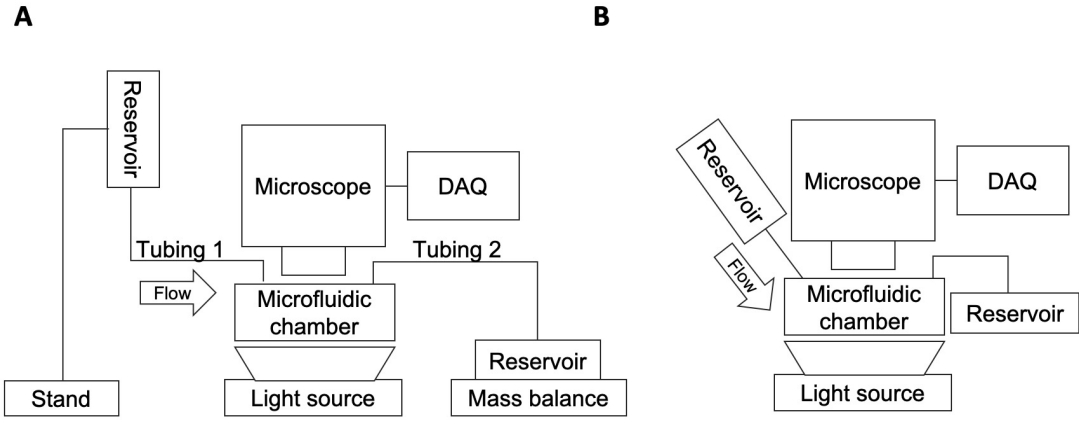

Figure 2-1. Microfluidic set-up (A) before and (B) after the optimization for the minimal blood usage.

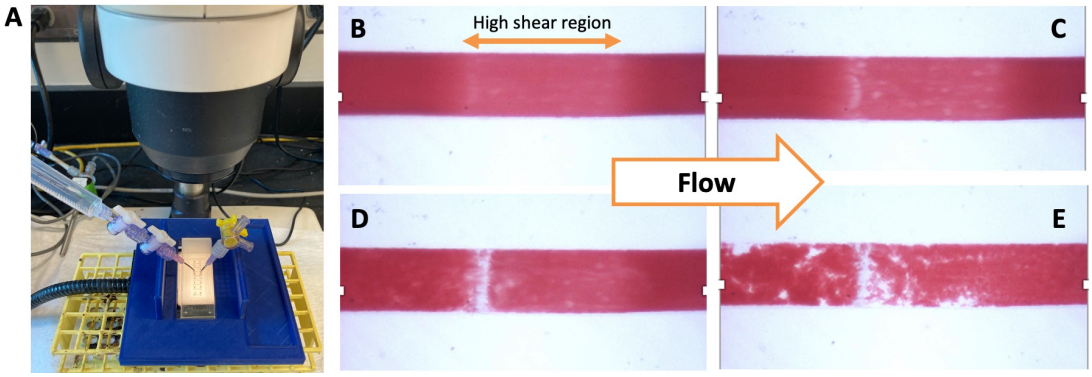

Figure 2-2. (A) Microfluidic set-up optimization using porcine blood before mice blood test. (B) Top-down view of blood flow in microfluidic channel. (C) Platelet

adhesion, (D) SIPA clot formation, and (E) occlusion was achieved with 1.5 mL of blood.

2.2.5 Folts-like arterial stenosis model

In vivo thrombus formation under the pathological shear rate was assessed using the Folts-like model of arterial thrombosis (Sturgeon, Jones, Angus, & Wright, 2006). A 6.0 silk suture was tied around the common carotid artery until the blood flow rate was reduced to approximately 50%, as monitored using a flow probe (Transonic Systems, NY, USA) to create a stenosis region and a high shear-stress environment. The carotid vessel under the stenosis was gently crushed using forceps to expose the subendothelial surface, and the blood flow was continuously monitored. Blood flow data were acquired with Powerlab, and analyzed using LabChart Pro version 8.1 (ADInstruments, CO, USA). Occlusive thrombus formation occurred when blood flow decreased to zero. Following experiments, the carotid artery, including the injury site, was dissected and fixed in neutral buffered formalin fixative overnight. The tissue was embedded in paraffin, sectioned, and stained using either hematoxylin and eosin (H&E) or the Carstairs method (Electron Microscopy Sciences. PA, USA). The histology images were captured using an Olympus BX42 microscope and Olympus DP72 digital camera with CellSens software (Olympus, PA, USA). The thrombus structure and composition were assessed where the platelets stained blue/purple, fibrin stained red, RBCs stained yellow, and the collagen was blue. A detailed protocol is described in Appendix A.

2.2.6 Analysis

The image analysis was performed using FIJI/ ImageJ 1.51n (NIH, USA), and the data were processed with Matlab (Mathworks, Natick, MA). The data analysis was performed

using GraphPad Prism 7 (GraphPad Software, San Diego, CA). Statistical significance ($p < 0.05$) was determined using the unpaired t-test or by one-way ANOVAs with Dunnett's post-tests for multiple comparisons (Upton & Cook, 2006). Data are displayed as mean with error bars denoting standard error of the mean (SEOM).

2.3 Results

2.3.1 Hemodynamic flow through a high shear microfluidic device and stenosed mouse carotid artery

We produced a microfluidic channel that mimics the stenosis of arteries. This system allows for the direct visualization of thrombus growth all the way to flow occlusion. We used the microfluidic channel geometry (Figure 2-3A) from Casa and Ku (2014) to incorporate not just platelet adhesion, but also RPA and the subsequent a massive levels of platelet aggregation. The maximum initial shear rate that occurred in the stenotic region of the channel was > 3,600 s^{-1}, whereas the upstream and downstream regions remained at a shear rate of < 1,000 s^{-1} (Figure 2-3C), comparable to the physiological arterial wall shear rate. The occlusion time for each channel was predicted using a quantitative, empirical high-shear thrombosis model described by Mehrabadi et al. (2016). A constant flow rate was assumed, and the occlusion time was defined as the point where the pressure difference reached the mean arterial pressure of a mouse (100 mmHg) and reached a constant pressure head at the inlet (4.8 mmHg) in the microfluidic set-up. The microfluidic channel occlusion time was predicted to be 264 ± 65 s, including a lag time of 109 s. The simulated thrombus growth and the shear rate build up during high-shear thrombosis formation in each channel is depicted in Figure 2-3E and F. The shear rate was expected to increase to as much as

100,000 s^{-1} and 10,000 s^{-1}, respectively. The mouse carotid artery dimensions were used for separate predictions for the *in vivo* situation. Based on previous studies (Bark Jr & Ku, 2010), a 60%-diameter stenosis in diameter causes an approximately 50% flow-rate reduction. Thus, the carotid stenosed artery is modeled as shown in Figure 2-3D, as a 60% stenosis with axisymmetric geometry. The shear-rate contour is described in Figure 2-3D, showing a maximum shear rate of 4,600 s^{-1} at the apex of the stenosis. No flow separation was seen in the distal area to the stenosis for this mouse artery stenosis. The occlusion time for the mouse was predicted to be 305 ± 77 s with a lag time of 81 s.

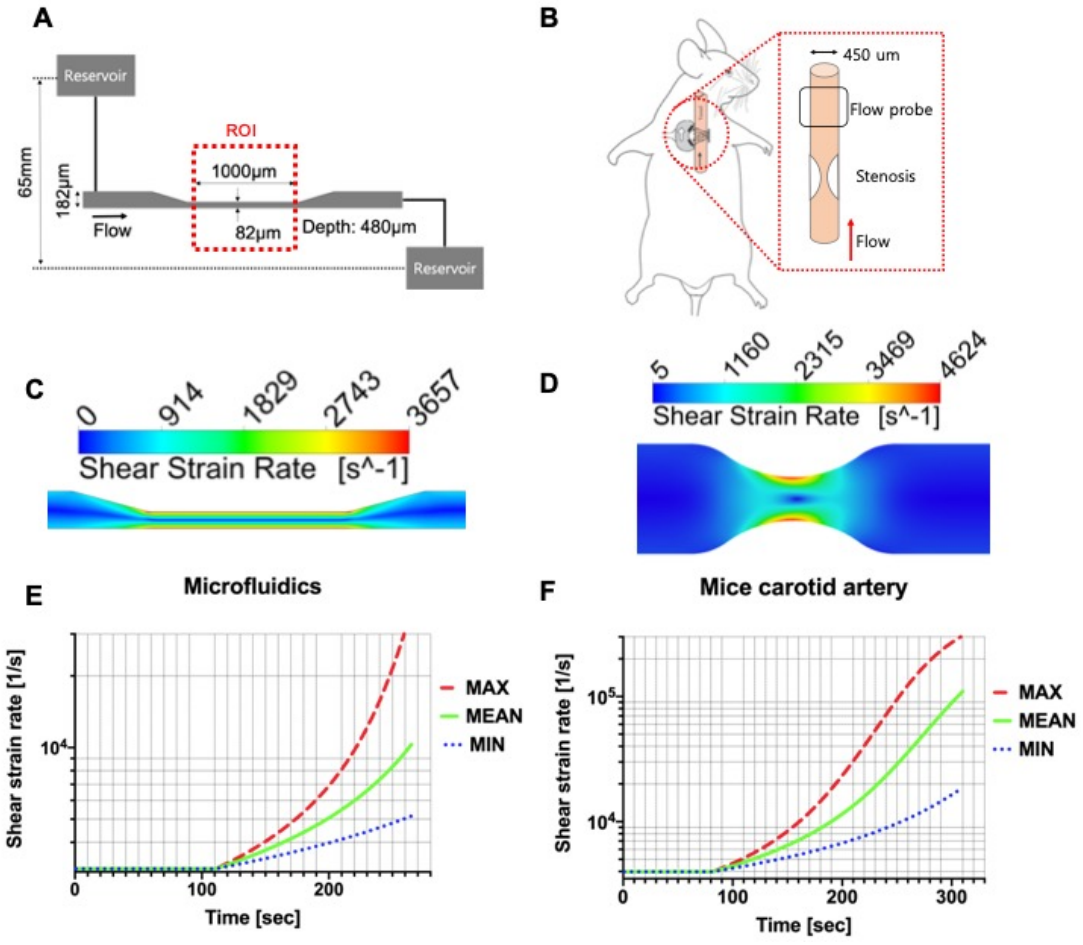

Figure 2-3. Hydrodynamic flow characteristics through a high-shear microfluidic device and stenosed mouse carotid artery. (A) Geometry of the microfluidic model

with a stenotic test section. (B) Schematic of *in vivo* experiments showing a stenotic region relative to flow direction and flow-probe placement. (C) CFD simulations of the microfluidic device. Blood flows from left to right. The color contour shows the shear strain-rate distribution. The solution shows a maximum shear strain rate of > 3,500 s^{-1} in the stenosis region, while the upstream and downstream values are < 1,000 s^{-1}. (D) CFD simulation in a stenosed mouse carotid artery. The large velocity gradient at the stenotic apex leads to initial shear rates that exceed 4,000 s^{-1}. (E) & (F) Thrombus growth was predicted using a high-shear thrombosis model by Mehrabadi et al. (2016). The shear strain-rate estimation over time during high-shear thrombosis formation in a microfluidic assay and mouse carotid artery. Min and Max denote for the lower and upper confidence limits of the model.

2.3.2 Platelet VWF is necessary to form occlusive thrombi

To visualize and conduct a rescue study, we perfused mice blood into the high-shear microfluidic channels. Prior to the mice study, the microfluidic set-up was optimized using porcine blood to reduce the required volume by removing extra tubing and connecting the reservoir directly to the microfluidic channel inlet. As a result, the single perfusion only takes 1.5-2 mL of blood, which is a 3~4 times reduction compared to the previous set-up. We obtained 1-1.5 mL of blood from each mouse and combined blood from two mice for each run. A constant pressure head of 4.8 mmHg was applied at the inlet, and the stenotic region of the channel was visualized by microscope. To enhance the visualization, we labeled the platelets with fluorescent dye. All seven WT mice blood experiments formed RPA and went to occlusion in 326 ± 25 s. In contrast, *Nbeal2*$^{-/-}$ mice blood showed only small amounts of platelet adhesion on the surface and no occlusion after 8 min (Figure 2-4). We then attempted to rescue the non-occluded channels by perfusing them with the WT mice blood. The rescued channels then formed RPA and went to occlusion in 166 ± 48 s (Figure 2-4B).

All the images were post-processed to compare the intensity levels in the test sections. Figure 2-4C describes the normalized intensity of the WT, *Nbeal2*$^{-/-}$, and rescue (WT) mice blood. The intensity of the WT mice blood increased rapidly, but the intensity of the *Nbeal2*$^{-/-}$ blood became saturated at 20%. The intensity in the *Nbeal2*$^{-/-}$ channels again increased rapidly post-rescue. The occlusion times for the WT, *Nbeal2*$^{-/-}$, and rescue blood were significantly different (Figure 2-4D, $p < 0.05$).

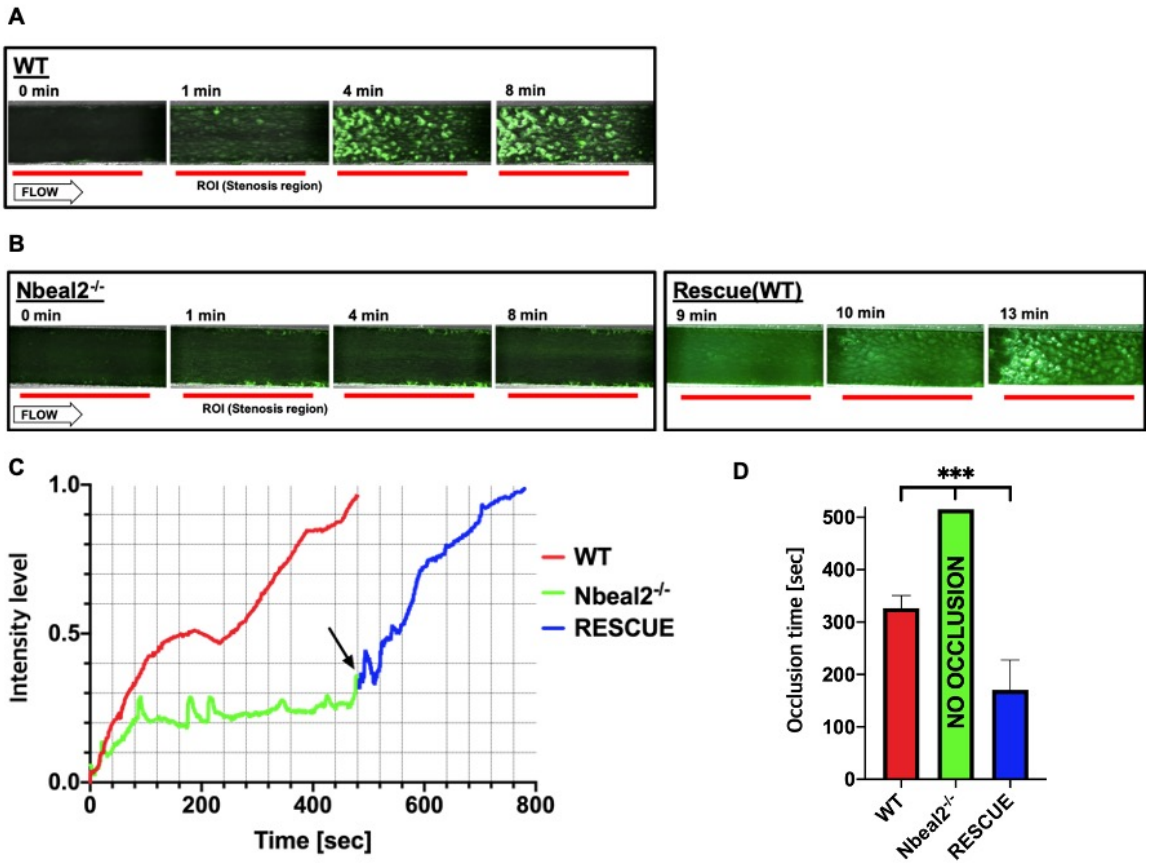

Figure 2-4. Plasma VWF is sufficient for the initial adhesion of platelets to collagen, while locally released platelet VWF is necessary for forming the subsequent occlusive thrombi. Representations of WT and *Nbeal2*$^{-/-}$ platelet adhesion and the subsequent occlusion during the 8-min perfusion period. The progressive accumulation of platelets is observed over time. (A) WT mice blood showed rapid and significant platelet adhesion and aggregation leading to occlusion. (B) *Nbeal2*$^{-/-}$ mice blood did not form occlusive thrombi during the 8-min observation period. Occlusive thrombi formed following the addition of WT whole blood (Rescue) to adherent *Nbeal2*$^{-/-}$

platelets on collagen. The 1-mm stenosis region is marked with a red line under the image. The region of interest (ROI) appears blank before the adhesion of platelets (green, DIOC6). The flow direction is from left to right. Scale bar, 1,000 μm. (C) Normalized fluorescent intensities comparing thrombus growth and occlusion in the control WT (n = 6), *Nbeal2*$^{-/-}$ (n = 6), and Rescue (n = 3) channels. The initial lag phase is quickly proceeded by RPA, demonstrated by a fast increase in thrombus size and intensity at approximately 100 seconds for WT whole blood and at 515 ± 47 s for *Nbeal2*$^{-/-}$ + WT whole blood. Occlusion occurs at the end of the plot for WT and *Nbeal2*$^{-/-}$ + WT whole blood. No occlusion was observed with *Nbeal2*$^{-/-}$ whole blood alone. A black arrow denotes the time point when WT whole blood was added to the *Nbeal2*$^{-/-}$ channels. All images were post-processed and averaged to compare the intensity levels in the test sections. (D) Occlusion times in the microfluidic device for WT (326 ± 25 s), *Nbeal2*$^{-/-}$ (no occlusion), and *Nbeal2*$^{-/-}$ + WT (166 ± 48 s) blood. All three occlusion times are significantly different from each other ($p < 0.001$).

2.3.3 Platelet VWF release induces localized formation of an occlusive thrombi

After platelet activation, a high concentration of ULVWF can be released from the activated platelets. A localized release of VWF could provoke the localized formation of occlusive thrombi. With identical microfluid channels and flow conditions, Griffin, Kim, and Ku (2019) found that a localized thrombus formed with human blood (Figure 2-5). To investigate whether the same outcome would occur for the mouse blood, we split the region of interest (ROI) into three ROIs (Figure 2-6A) and compared the intensity level of each ROI. The final intensity level in the ROI 1 (upstream) was significantly higher than the other 2 ROIs for the WT and Rescue (Figure 2-6B, $p < 0.01$), but there was no significant difference between the ROIs for *Nbeal2*$^{-/-}$. The intensity level of each ROI over perfusion time (Figure 2-6C & D) showed a sudden intensity increase in ROI 1 for the WT (80 s) and Rescue (20 s), but only a small intensity level increase in ROI 2 and 3. Thus, RPA occurs in the confined upstream part of the stenosis (333 μm), and serves as the dominant location for the channel occlusion in the microfluidic system.

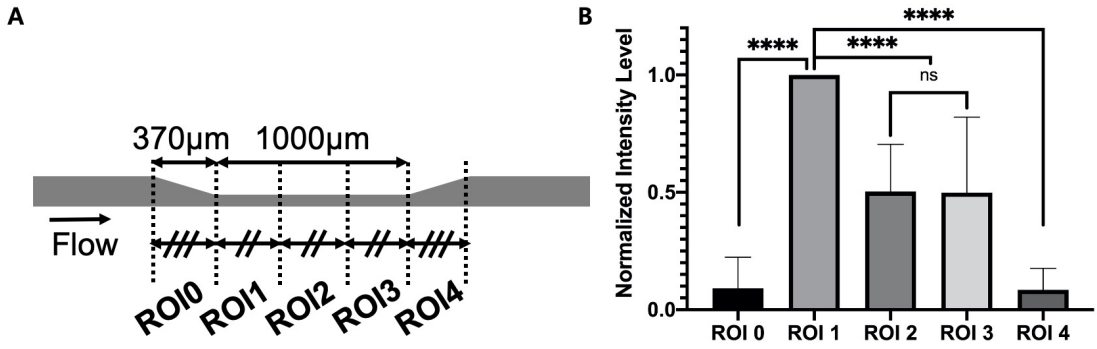

Figure 2-5. Human SIPA clots forms at upstream regions of stenotic section in microfluidics (n = 8). (A) Channel is separated into 5 ROIs. (B) ROI 1 showed significantly higher normalized intensity level compare to the other ROIs ($p < 0.0001$). ROI 2 and 3 had a 50% lower intensity level compare to ROI 1. ROI 0 and 4 had lowest intensity level approximately 10% lower than ROI 1.

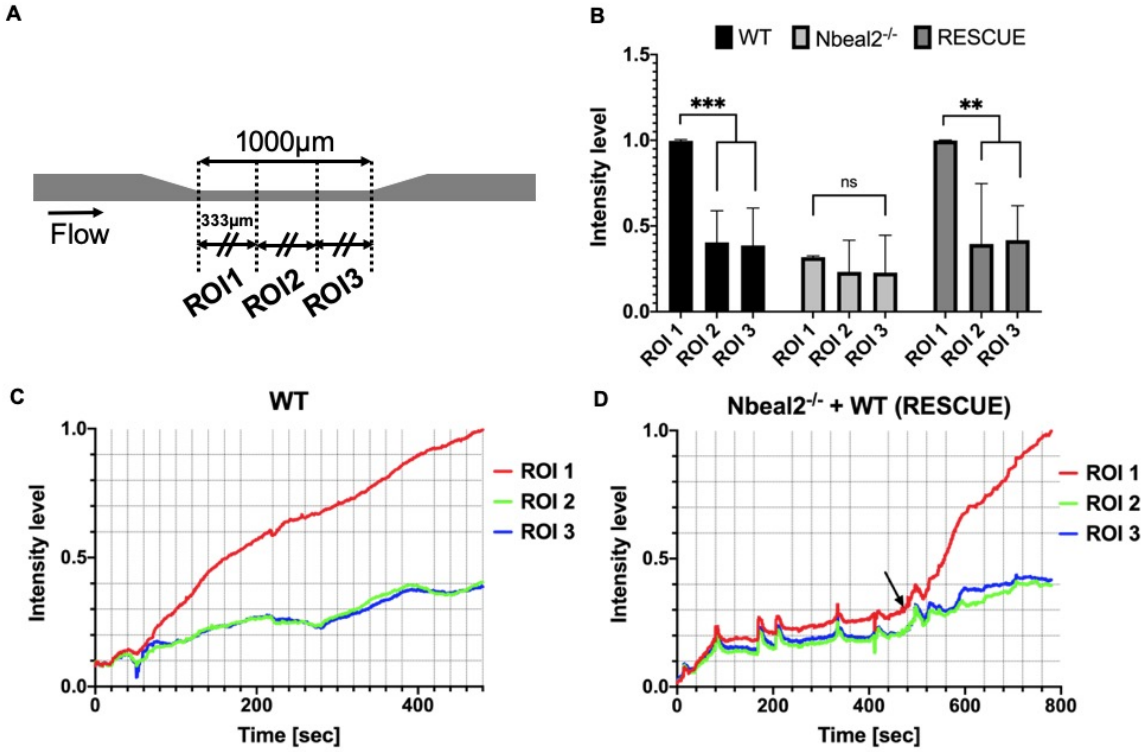

Figure 2-6. The platelet VWF induces the localized formation of occlusive thrombi. (A) The three ROIs for the microfluidic channel test section. (B) Normalized fluorescent intensity level of each ROI after an 8-min perfusion for WT (n = 6) and *Nbeal2*$^{-/-}$ (n = 3), and a 5-min perfusion for the Rescue (n = 3). ROI 1 showed a significantly higher intensity level with WT ($p < 0.001$) and Rescue ($p < 0.01$) compared to ROI 2 and 3. There was no significant increase in ROI 1 with *Nbeal2*$^{-/-}$.

(C) & (D) Intensity levels of each ROI over perfusion time. The black arrow denotes the time point when WT whole blood was added to the *Nbeal2*$^{-/-}$ channels. The intensity level of ROI 1 rapidly increased after 80 s for the WT and 20 s for the Rescue.

2.3.4 Occlusive thrombus did not form in the Folts-like arterial stenosis model without platelet von Willebrand Factor (Nbeal2$^{-/-}$*)*

Using the Folts-like murine model, the distal flow rate was monitored before and after the crush injury, as shown in Figure 2-7A. After suturing the carotid artery to generate the stenosis, we waited for more than 2 min for the flow rate to stabilize. All flow rates for the WT mice eventually decreased to 0 mL/min. In contrast, none of the *Nbeal2*$^{-/-}$ mice showed flow cessation ($p < 0.0005$). The occlusion time in WT mice was 352 s on average following de-endothelization of the stenosed vessel. This is comparable to the predicted occlusion time of 305 ± 77 s. We then collected carotid arteries from the thrombosed mice to perform histology to identify clots and their composition. Figure 2-7C & D shows the platelet-rich thrombus in the WT artery, but no thrombus was observed in the *Nbeal2*$^{-/-}$ mice. These findings support platelet VWF from α-granules being critical for occlusive thrombus formation in a stenosed arteries.

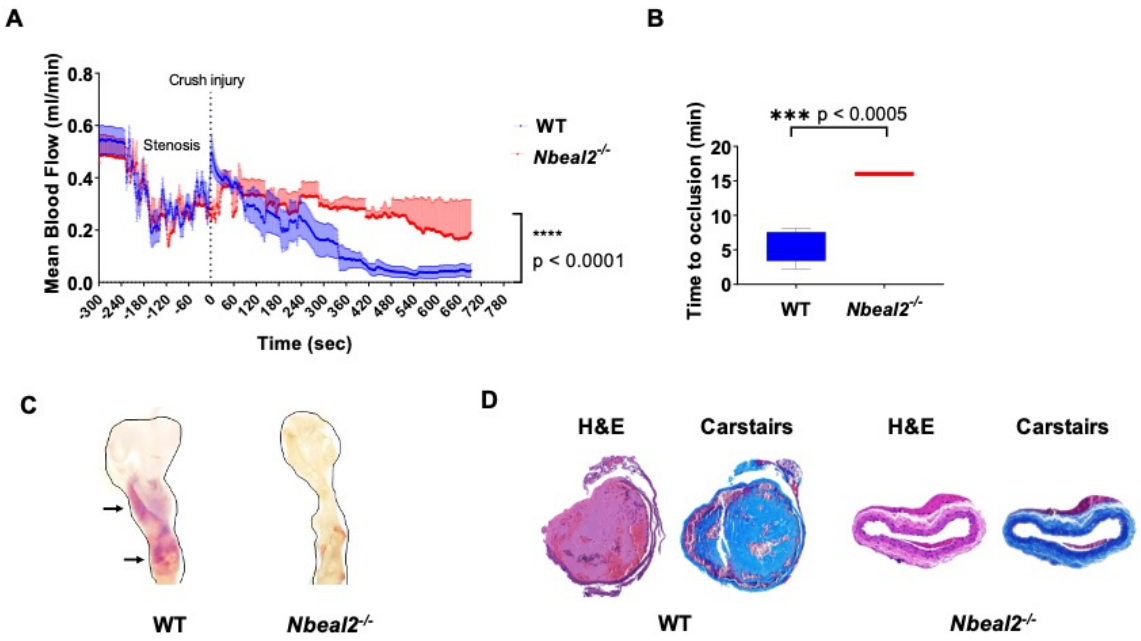

Figure 2-7. The absence of platelet VWF prevents occlusive thrombus formation in the modified Folts arterial stenosis model. (A) Mean blood flow through the carotid artery with an ~50 % stenosis (reduction in blood flow) and crush injury. WT mice consistently formed an occlusive thrombus in response to the stenosis and a crush injury. In contrast, there was no occlusive thrombus formation in the carotid artery of the *Nbeal2*$^{-/-}$ mice (n = 7 ± SEOM, $p < 0.0001$). (B) WT mice formed occlusive thrombi at an average time of 330 sec following de-endothelization of the stenosed vessel. *Nbeal2*$^{-/-}$ mice were unable to form occlusive thrombi *in vivo*. (n = 7 ± SEOM, $p < 0.0005$). (C) Representative macroscopic images of the gross anatomy of an excised carotid artery from WT and *Nbeal2*$^{-/-}$ mice. The WT carotid artery features a prominent clot (arrowheads) within the longitudinal arterial lumen (outlined), suggesting the presence of an occlusion. There is a clear absence of occlusive matter within the lumen of the *Nbeal2*$^{-/-}$ carotid artery (outlined). (D) Carstairs histological staining revealed that WT thrombi were primarily composed of platelets (the blue material occluding in the lumen).

2.3.5 Platelet von Willebrand Factor is essential for the rapid platelet accumulation phase and induces vessel occlusion

We applied the thrombosis growth model by Mehrabadi et al. (2016) for microfluidics and the mouse carotid artery, and compared occlusion times with the experimental results. The

microfluidic channel was predicted to have a lag phase time of 138 s, followed by RPA phase of 109 s, resulting in a total occlusion time of 247 s, which is comparable to the experimental result (326 ± 25 s). *Nbeal2*$^{-/-}$ mice did not advance from the lag phase, and no RPA was observed. However, when WT mouse platelets were perfused through to the same device channel containing *Nbeal2*$^{-/-}$ adherent platelets, the RPA phase occurred almost immediately. The *Nbeal2*$^{-/-}$ lag time was subtracted from the RPA phase time of the rescue (WT), and the experimental results with an occlusion time of 170 ± 57 s were comparable to the predicted values for RPA occlusion of 138 s (Figure 2-8).

In simulations of a 60%-diameter stenosed mouse carotid artery, the modeled occlusion time was calculated as 305 s, which was similar to the WT *in vivo* experiments that exhibited a mean occlusion time of 352 s (Figure 2-8).

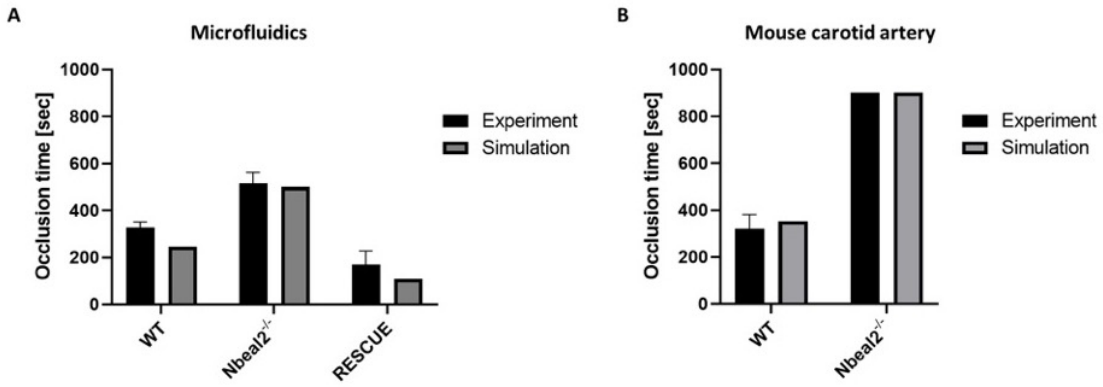

Figure 2-8. Comparison of simulated occlusion times against actual experimental values. (A) *In vitro* microfluidics. (B) *In vivo* mouse carotid artery Folts-like model.

2.4 Discussion

We used the two-phase arterial thrombosis model by Mehrabadi et al. (2016), to predict occlusion times and the shear rate during high-shear thrombosis formation. The model is simplified by assuming a constant flow rate and used pressure as the end point to predict occlusion time. The simulated occlusion times were in good agreement with what was we found in the experiments, and we were able to predict the rescue time by subtracting the simulated lag time. Para and Ku (2013) demonstrated experimentally that the occlusion time is equivalent when they used the same end point as we used in this model.

α-granules are necessary for the initiation of the RPA phase, and the *Nbeal2*$^{-/-}$ mice did not show RPA and occlusion in either the *in vitro* or *in vivo* models. To confirm the result, we rescued *Nbeal2*$^{-/-}$ mice with WT mice blood by perfusing into the same microfluidic channel. We found that there was restoration of large platelet aggregation and RPA, and the occlusion time was significantly faster than for the WT mice blood alone. The plasma VWF levels do allow for the adhesion of some fast-moving platelets to complete the lag phase of surface coverage. However, to reach RPA with the capture of 10x as many platelets at the wall, the α-granules are necessary. The *Nbeal2*$^{-/-}$ murine model verifies *in vivo* the critical role of α-granules for occlusive, high-shear thrombosis. α-granules store high concentrations of ULVWF, the most important protein for the high-shear thrombosis. An occlusive thrombus is only formed in the presence of platelets with normal α-granules. This was seen when collected carotid artery was performed histology.

Nbeal2$^{-/-}$ mice blood has previously been reported to have normal plasma VWF, but a 40% lower platelet counts compared to the WT (Deppermann, Cherpokova, et al.,

2013; Kahr et al., 2013). However, Casa et al. (2016) showed 10% platelet-diluted blood can still form a high-shear thrombosis but not with plasma VWF at a 10% dilution. We found that all of the WT mice carotid arteries went to occlusion, but no occlusion was observed for the *Nbeal2*$^{-/-}$ mice. In the WT vessel, we found platelet-rich thrombi occluding the lumen. Similar results were seen in the microfluidic study, and we found that there was a large aggregation and occlusion with WT mice blood. *Nbeal2*$^{-/-}$ mice blood only showed adhesion on the surface but no RPA or occlusion.

Previous *Nbeal2*$^{-/-}$ mice thrombus formation studies by Kahr et al. (2013) and Deppermann, Cherpokova, et al. (2013) only accounted for maximum physiological arterial shear rates of 1,700 s^{-1} at and not for pathological shear rates over 3,000 s^{-1} and up to 100,000 s^{-1}. Under physiological shear rate, the role of α-granule VWFs on thrombus formation could be subsidiary and not important for the vessel occlusion. Except for the abdominal aorta model by Deppermann, Cherpokova, et al. (2013), both groups used small arterioles that could be prone to occlude with only platelet adhesion during the lag phase and not with RPA. Casa and Ku (2014) suggest that circular channels should be no more than 90 μm in diameter, with a rectangular channel height greater than 50 μm, and with a high aspect ratio to take into account platelet-platelet interaction, which is critical for the RPA phase. In this study, we created a stenotic microfluidic channel and sutured mice carotid artery that satisfied both criteria (high shear rate and a large enough channel) and that can incorporate not only the lag phase, but also the RPA phase.

The VWF is the most important protein that regulates high-shear thrombosis. It originates from endothelial cell-derived plasma VWFs and platelet α-granule-released VWFs. The other α-granule proteins, fibronectin and thrombospondin may help a SIPA

clot to stabilize but are likely not as important as VWF for the SIPA clot to grow under high shear conditions as they are short and in lower concentration. Ruggeri et al. (2006) emphasized the dominant role of plasma VWFs under high shear conditions on large platelet aggregation. They found that an absence of plasma VWFs suppressed platelet aggregation under a 1,500 s^{-1} shear rate but had no impact under 500 s^{-1}. However, platelet VWFs could be more, or at least equivalently important for the high-shear thrombosis and vessel occlusion. Even with the normal plasma VWFs, the *Nbeal2*$^{-/-}$ mice showed no occlusion *in vitro* and *in vivo,* and they were limited to platelet adhesion or small platelet aggregation at the wall. Thus, plasma VWFs could be important for the lag phase but not for the RPA phase, and platelet VWFs are more important for the RPA phase.

Current antithrombotic therapies, such as aspirin (ASA) and Plavix® (Clopidogrel) target different pathways of platelet activation in general. However, inhibiting platelet activation may enhance antithrombotic effects but it can also cause severe bleeding complications (Mauri et al., 2014). On the other hand, hemostasis may not require platelet VWFs, and targeting α-granules or α-granule released VWFs could be a potential novel antithrombotic therapy. Indeed, GPS patients have a mild to moderate bleeding tendency (Gunay-Aygun et al., 2010; Jantunen, Hänninen, Naukkarinen, Vornanen, & Lahtinen, 1994; Nurden & Nurden, 2007), yet even this bleeding could be improved by specifically targeting platelet VWFs while preserving the other α-granule proteins, thrombospondin, fibronectin, and FV.

This study has two main limitations. One limitation is that the animals we used were mice and porcine for the *in vitro* set-up optimization. We could have used GPS patient' blood for the same rescue experiments that we performed with *Nbeal2*$^{-/-}$ mice blood. The

second limitation is that although we emphasized the importance of the platelet VWF, we have not proved experimentally that platelet VWFs are important for the high-shear thrombosis and vessel occlusion; rather, this is limited to the α-granule. These topics are for the future study.

2.5 Conclusion

The critical role of platelet VWF release on the formation of an occlusive thrombus is demonstrated. A combination of *in silico* predictions with *in vitro* and *in vivo* experiments revealed the necessary role of α-granules for RPA phase initiation and SIPA thrombus formation. The essential part of platelet VWF to induce SIPA under high-shear conditions in stenotic arteries makes it a potential new target for pharmacological interventions to prevent SIPA clot formation in myocardial infarction or stroke patients.

2.6 Acknowledgments

This work was a collaborative study with Katrina Ashworth and Dr. Jorgè Di Paola in the Di Paola lab.

CHAPTER 3. THE PERMEABILITY AND MECHANICAL STRENGTH OF A SIPA CLOT

3.1 Introduction

Arterial thrombosis in a coronary artery or carotid artery can lead to a myocardial infarction or an acute ischemic stroke. The formation of an occlusive thrombus in these arteries blocks blood flow and impinges heart or brain function, resulting in the patient's death. To cease the blood flow, the thrombus needs to resist a high shear rate up to 400,000 s^{-1} (Bark & Ku, 2010) and arterial blood pressure over 175 mmHg (Stamler, Neaton, & Wentworth, 1989). Currently, the available treatments for arterial thrombosis are thrombolytic drugs or a thrombectomy.

A thrombolytic agent such as tPA hopefully chemically dissolves clots to regain blood flow in the vessel. It is critical to systemically administer the tPA within three hours of symptom onset to achieve a significant clinical outcome (Bivard et al., 2013). To initiate the chemical reaction, the drug needs to be delivered to the clot. Considering a blood clot as a porous material, its permeability is strongly related to the delivery of the thrombolytic drug via convection and diffusion (Diamond, 1999; Piebalgs et al., 2018). In a clinical trial, Santos Emilie et al. (2016) found that patients had 3.2 times more favourable outcomes and 2.5 times higher recanalization rates when the clot was more permeable. Wufsus, Macera, and Neeves (2013) measured platelet-rich clot permeability under static conditions, finding that the coagulation clot permeability ranges from 1.1×10^{-2} μm^2 to 1.5×10^{-5} μm^2. Meanwhile, Kobayashi, Sekar, and Ku (2016) observed erythrocytes traveling through an occlusive SIPA clot with a distal velocity of 100 μm/s. Thus, SIPA clots might

have significantly high permeability compared to coagulation clots. However, no previous studies have measured the permeability of SIPA clots that are formed under pathological high shear rates. The permeability of the clot is also important for aspirational thrombectomy devices that use fluid force for the clot breakage and retrieval. Mokin et al. (2020) found that clot perviousness was associated with the first pass success of aspiration thrombectomy in a clinical trial. They also found that perviousness had no significant correlation with the stent retriever thrombectomy group.

Stent or coil retrievers are wire-based thrombectomy devices that apply mechanical force to break and retrieve a clot. Thus, the mechanical strength of the clot could be more important that permeability for the success of mechanical thrombectomy devices. While breaking and retrieving a clot, it becomes deformed, elongated, thinned, fractured, and fragmented (Yang et al., 2020). Yeo et al. (2019) suggested that successful thrombectomy depends on clot composition and properties, such as friction (Gunning et al., 2018), maturity (Duffy et al., 2017), and stickiness (Pikija et al., 2016). Clinically, Thromboelastography (TEG) has been used to measure clot strength and predict clinical outcome of ischemic stroke (Yao et al., 2014) and coronary artery disease patients (Bitar & Kreutz, 2013). However, TEG indirectly measures clot strength using the unphysiological swirling motion of a rod in a clot to measure resisting force. Many studies have attempted to measure the mechanical strength of a blood clot using various methods, including the tensile tester, the compression tester, a dynamic mechanical analyzer, a rheometer, dynamic ultrasound viscoelastography, nanoindentation, and a viscometer (Johnson et al., 2017). However, these measurements only examined coagulation clots and resulted in very distinctive values at 10 orders of magnitude (Figure 3-1). The tested

coagulation clots were either collected (Intraluminal thrombus from abdominal aortic aneurism: Di Martino et al. (1998), Gasser, Görgülü, Folkesson, and Swedenborg (2008), Teng et al. (2015), and Ashton, Vande Geest, Simon, and Haskett (2009) / Deep vein thrombus: Xie et al. (2005)) or generated via *in vitro* assays (Chueh et al. (2011), van Dam et al. (2006), Schmitt, Hadj Henni, and Cloutier (2011), Slaboch, Alber, Rosen, and Ovaert (2012), Henderson and Thurston (1993), McCarty et al. (2011), Riha, Wang, Liao, and Stoltz (1999), Ryan, Mockros, Weisel, and Lorand (1999), and Hinnen, Rixen, Koning, van Bockel, and Hamming (2007)).

Coagulation clots and SIPA clots differ in terms of their formation mechanism and composition. A coagulation clot follows the classic Virchow's triad (Figure 1-2), which consists of endothelial disruption, stagnant blood flow, and hypercoagulability (Lefkowitz, 2008). The main component of a coagulation clot is fibrin, which is the final product of the coagulation cascade that entraps large amounts of RBCs. A coagulation clot is often referred to as a red clot because it appears to be red in color due to the presence of a large number of RBCs. However, a coagulation clot can appear to be white in color if the clot is formed from artificially generated PRP that lacks RBCs but is still fibrin abundant. Meanwhile, Casa et al. (2015) suggested that an alternative triad is necessary for SIPA clot formation: (i) a collagen surface or other substrate for initial VWF absorption, (ii) a pathologically high shear rate for VWF unfolding and elongation, and (iii) platelets and VWF in sufficient concentrations (Figure 1-2). Thus, a SIPA clot is mostly composed of platelets and VWFs; this is supported by Ku and Flannery (2007)'s study in which 80% of SIPA clot was consisted of platelets. SIPA clots look white and are commonly called white clots because of the prevalence of platelets and the lack of RBCs. To induce SIPA, many

thousands of GPIb-A1 bonds are required to capture platelets under high shear (Wellings & Ku, 2012). These bonds may give a SIPA clot a high level of mechanical strength so that it can resist the arterial shear rate and blood pressure.

The high permeability and mechanical strength of a SIPA clot could be a key feature that allows it to stabilize in such a high pressure and high shear rate environment and hinder the blood flow. In the present study, we aimed to measure SIPA clot permeability and mechanical strength using *in vitro* flow systems and investigate how a SIPA clot can block blood flow in an artery.

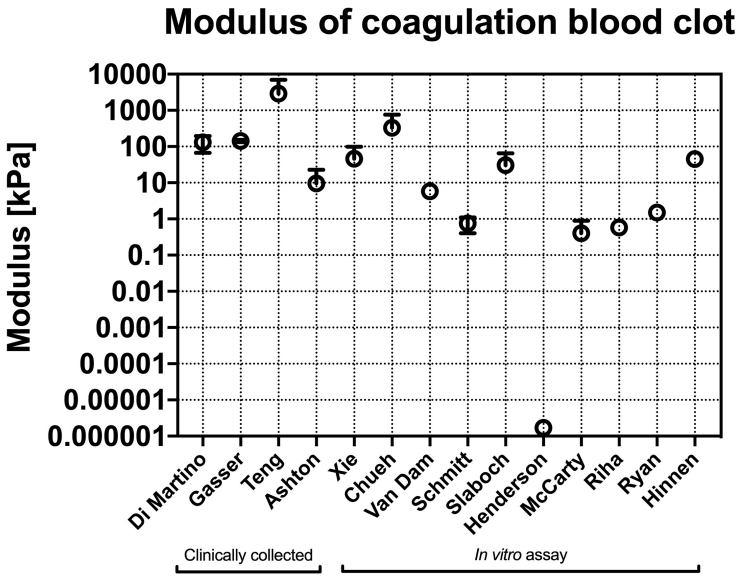

Figure 3-1. Coagulation blood clot modulus from Johnson et al. (2017) and Slaboch et al. (2012).

3.2 Methods

In order to generate SIPA clots and measure its permeability and mechanical strength, controlled flow environments were created via *in vitro* settings. SIPA clots retrieved from the circuits were used to measure modulus and investigate structure. The porous structure was studied by taking scanning electron microscope (SEM) and histologic images. Measured SIPA clot's properties were compared to the coagulation clot's values and applied to a simulation to investigate whether a clot can occlude a stenosed coronary artery or not.

3.2.1 In vitro stenotic chambers

Three different stenotic chambers (Figure 3-2) were used to induce high shear conditions and generate SIPA clots of varying shapes and sizes. Based on coronary artery diameter of 4 mm, each chamber corresponds to 98% stenosis by diameter (microfluidic chamber), 85% stenosis by diameter (stenotic capillary glass tube, ID = 1.5 mm), and 45% stenosis by diameter (stenotic large glass tube, ID = 12 mm) in diameter. Prior to the blood perfusion, the stenotic region of each chamber was coated with type 1 fibrillar collagen and incubated in a container for 24 hours to generate an adhesive surface. The 12 mm large tube (Figure 3-2C) was rotated 180 degrees once after an hour, counting from the moment when a collagen solution was added to the tube.

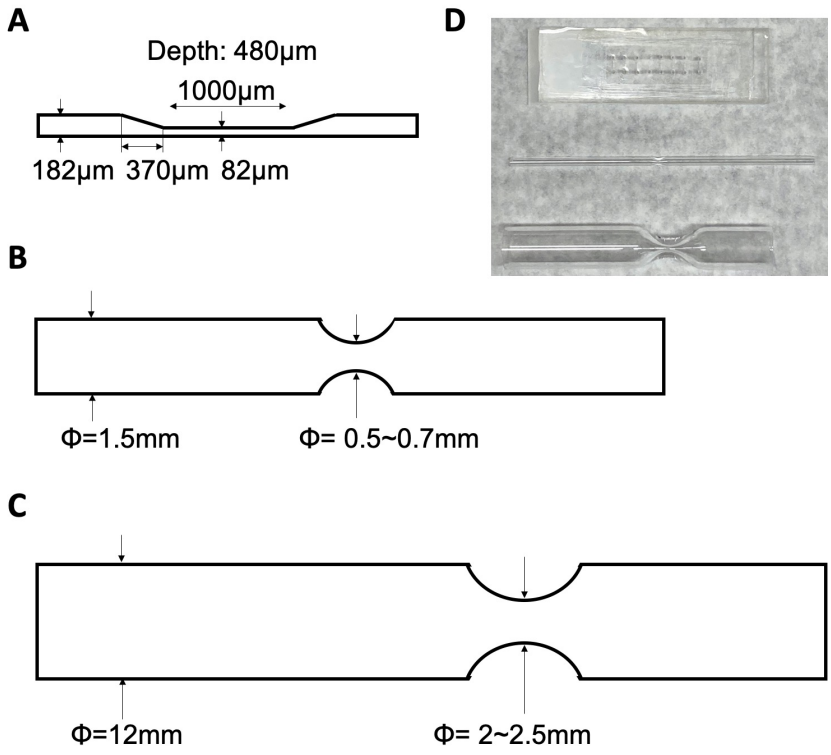

Figure 3-2. Geometry of the stenotic chambers: (A) Microfluidic chamber (55% stenosis by diameter), (B) Capillary glass tube (ID = 1.5 mm, 65% stenosis by diameter), and (C) Large glass tube (ID = 12 mm, 80% stenosis by diameter). (D) Photograph of actual test sections showing the size comparison of the three chambers.

3.2.2 In vitro flow loops for SIPA clot generation

To generate a SIPA clot, lightly heparinized (3.5 IU/mL) porcine WB was perfused through three *in vitro* flow systems with the three different stenotic chambers. PDMS microfluidic and capillary tube were used in single-path *in vitro* flow systems with two different driving protocols: constant pressure or constant flow.

For the constant pressure experiments (Figure 3-3A), blood flow was driven by a constant pressure head of 4.8 mmHg for the microfluidic chamber and 66 mmHg for the 1.5 mm capillary tube (Ku & Flannery, 2007). In these experiments, mass outflow was measured by a precision balance. For the constant flow experiments (Figure 3-3B), the

flow rate was controlled using a syringe pump to generate an initial wall shear rate of 3,500 s^{-1} in the stenosis (Para & Ku, 2013). The pressure proximal to the stenosis was monitored. SIPA clot formation in the stenosis was recorded throughout the experiment using a high-resolution CCD microscope camera. Meanwhile, a high flow rate (~1 L/min) was required to generate a high shear in the large tube (Figure 3-2C). To accommodate this requirement, a closed *in vitro* flow loop was developed with two reservoirs for a constant pressure head (30 mmHg) (Figure 3-3C). As the clot grew in the tube, the flow rate of the roller pump was manually reduced every 1-2 min and recorded. When the roller pump flow rate reached a minimum level (0.05 L/min), the pump was turned off and left the circuit for an additional 30 minutes to achieve the full occlusion.

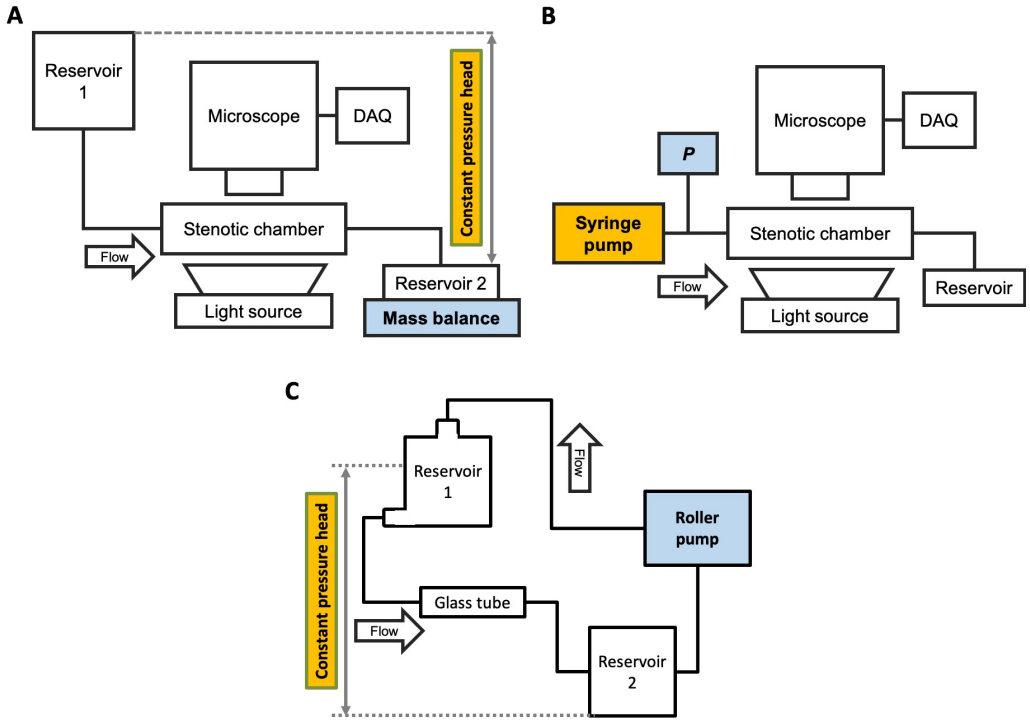

Figure 3-3. *In vitro* flow loops with different flow drivers. A single-path flow driven by (A) a constant pressure head or (B) a constant flow rate was used with the microfluidic chamber and capillary tube to measure clot permeability and breakage strength. (C) A closed loop circuit was developed to generate a clot in a large stenosis

that has diameter greater than 2 mm, in order to investigate clot structure and mechanical strength.

3.2.3 Coagulation clot generation

A non-stenotic capillary tube was coated with type 1 fibrillar collagen and incubated in a container for 24 hours to generate an adhesive surface. Porcine blood was treated with 3.2% sodium citrate (10% in volume) during transportation and recalcified with $CaCl_2$ to a final concentration of 10 mM just before placing the blood in the capillary tube (Griffin et al., 2019; Matsuo et al., 1981b). 20 µl of re-calcified porcine blood was placed in the capillary tube and left still for at least 30 minutes to form a stable red coagulation clot prior to the perfusion studies.

3.2.4 Permeability measurement using Darcy's law

In the high shear flow experiments, SIPA clots grew and eventually occluded the channel. Darcy's law (Whitaker, 1986) was used to quantity permeability of these occlusive SIPA clots:

$$\kappa = \frac{\mu Q L}{A \Delta P} \tag{5}$$

where κ is the clot permeability, μ is the fluid viscosity, Q is the flow rate, ΔP is the pressure difference across the clot, L is the clot length, and A is the clot cross-sectional area. In this calculation, the clot was modeled as a cuboid or cylindrical porous block in the microfluidics chamber or capillary tube, respectively (

Figure 3-4). The values of L and A *are* extracted from the image data and used a constant blood viscosity of 3.5 cP.

For the constant pressure head-driven experiments, outlet mass was measured over perfusion time and corrected by reflecting evaporation at the reservoir surface (Figure 3-5). The flow rate was calculated from the curve-fitted mass outflow for 10 minutes (microfluidic chamber) or 1 hour (capillary tube) after the occlusion. For the constant flow rate experiment, the maximum pressure proximal to the clot was measured by a pressure transducer and used to calculate the permeability. To measure red coagulation clot permeability, air was used as a fluid and perfused by a syringe pump with a constant flow rate of 0.002 mL/min. The pressure proximal to the clot was used to calculate the permeability.

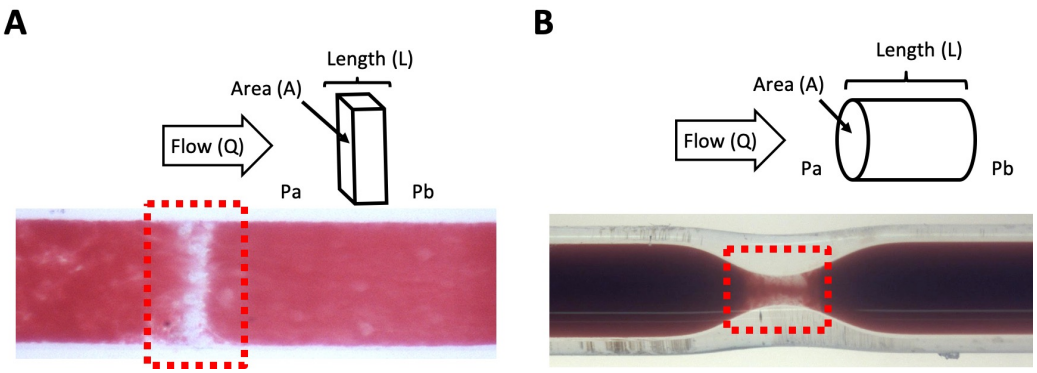

Figure 3-4. Parameters from perfusion images for the permeability calculation using Darcy's law. (A) Cuboid porous medium modeling the clot in the microfluidic chamber. (B) Cylindrical porous medium modeling the clot in the capillary tube.

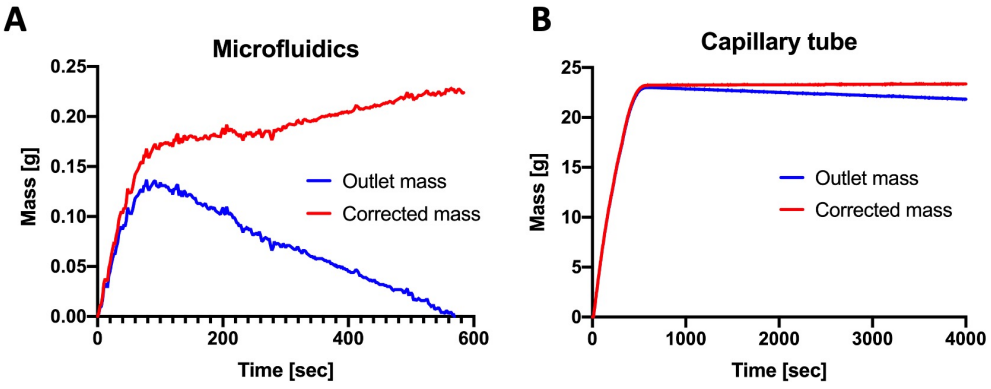

Figure 3-5. Outlet mass measured (blue) along the perfusion time in (A) the microfluidic chamber and (B) the capillary tube. Evaporation at the reservoir surface is reflected, and the corrected outlet mass is shown in red line.

3.2.5 Multi-channel analysis

SIPA clot is modelled as a porous media with multi cylindrical channels. Assuming Poiseuille's flow in each channel, hydraulic resistance of single channel and clot can be expressed as:

$$R_p = \frac{128\mu L}{\pi d_p^4} \tag{6}$$

$$R_c = \frac{\mu L}{A\kappa} \tag{7}$$

where μ is the fluid viscosity, L is the clot length, and d_p is the channel diameter. Pressure drop by a single channel and permeability is equivalent. Thus, the following equation can be acquired:

$$d_p = \sqrt[4]{\frac{128A\kappa}{\pi n_p}} \tag{8}$$

where κ is the clot permeability, A is the cross-section area, and n_p is the number of channels in the clot. The channel number and diameter can be expressed using porosity (ε) as follows (Whitaker, 1986).

$$\varepsilon = \frac{\pi d_p^2 n_p}{4A} \tag{9}$$

Thus:

$$n_p = \frac{4\varepsilon A}{\pi d_p^2} \tag{10}$$

$$d_p = \sqrt{\frac{32\kappa}{\varepsilon}} \tag{11}$$

3.2.6 Breakage strength measurement

With a syringe pump, constant flow was induced into the stenotic chambers to generate a SIPA clot. The pressure upstream increased as the SIPA clot grew at the stenotic region; eventually, the clot broke off was transported to the downstream reservoir. After the breakage, the SIPA clot regrew and reoccluded the chamber. Therefore, the broken part was not the collagen-glass wall interface. The blow-out pressure when the clot was breaking off was used to calculate the breakage strength of the clot. The clot was modelled as a homogeneous material that fully occluded the chamber, as shown in Figure 3-6. The forces acting on the clot were calculated as follows:

$$F_1 = \pi r^2 \cdot \Delta P \tag{12}$$

$$F_2 = \pi r \cdot L \cdot \tau \tag{13}$$

where r denotes radial distance, ΔP is the pressure difference across the clot, L is the clot length, and τ is stress. The balance between these two forces, τ, was calculated using the following equation:

$$\tau = \frac{r \cdot \Delta P}{2L} \tag{14}$$

The maximum stress occurs at the most-outer edge ($r = R$) of the clot; this was confirmed in the experiments, as the clots were found to be broken as a big piece. The following equation was used to calculate the breakage strength of the clot (τ_{MAX}):

$$\tau_{MAX} = \frac{R \cdot \Delta P}{2L} \tag{15}$$

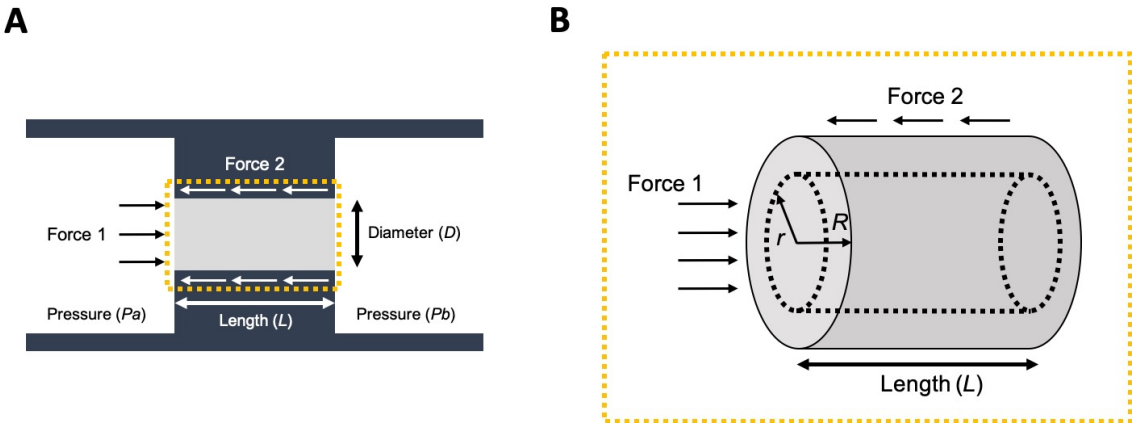

Figure 3-6. Forces acting on an occlusive clot in a stenotic chamber. (A) Two-dimensional and (B) three-dimensional views of forces and parameters on an occlusive clot.

3.2.7 Computational fluid dynamics and finite element analysis

CFD was used to predict the shear rate distribution within the large glass tube. A simulation was performed using Ansys 19.1 (Ansys Inc., PA, USA). Whole blood (WB) flow was assumed to be a Newtonian fluid of 3.5 cP, and the flow was presumed to be laminar, incompressible, steady, continuum, and isothermal based on the Reynolds number (=1,400) of the experiments. The no-slip boundary condition was applied to the walls, and a 0.66 L/min flow rate was applied at the inlet with zero pressure at the outlet (Figure 2-3B). Mesh convergence was achieved at 0.6 million hexagonal cells. To simulate pressure distribution and flow rate after a SIPA clot formation, a porous media was added to the CFD model

(light blue, Figure 3-7). With the clot, the simulation converged with 2.6 million hexagonal cells. The calculated pressure distribution was transferred to Ansys Static Structural module (Ansys Inc., PA, USA) for a finite element (FE) analysis. The analysis was simplified by applying a 2-D axisymmetric condition (Figure 3-8). A fixed support boundary condition was applied at the interface between the clot and channel wall and the pressure distribution from CFD results was applied at the upstream and downstream clot surfaces. Mesh convergence was achieved at 0.1 million tetragonal cells.

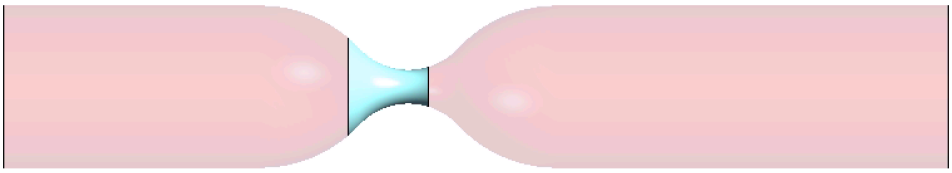

Figure 3-7. A porous media CFD model with a clot (light blue) located at the stenosis.

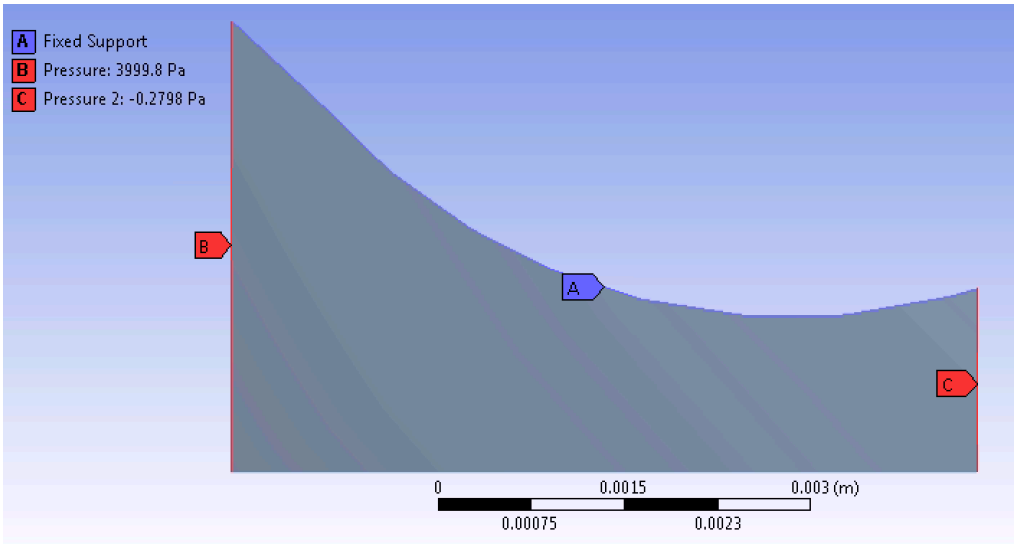

Figure 3-8. A 2-D axisymmetric model for a simulation of clot deformation and stress distribution. (A) A fixed support boundary condition was applied at the interface

between the clot and channel wall. Calculated pressure was applied on (B) proximal and (C) distal clot surfaces.

3.2.8 Histology and immunohistochemistry

Blood clots were fixed in formalin and embedded in paraffin for further histological and immunohistochemical analyses. The paraffin block holding the clot was cut into 5 μm-thick slices and deparaffinized. Using Carstairs's staining method, platelets were colored in light blue, fibrins in red, RBCs in yellow, and white blood cells (WBCs) in black. VWF was stained in brown using immunohistochemistry, and counterstaining was performed using Meyer's haematoxylin.

3.2.9 Scanning electron microscope imaging

Blood clots were fixed in a 10% formalin solution for more than 24 hours. A fixed blood clot was submerged into successive ethanol solutions of 25%, 50%, 75%, 80%, and 90% concentrations for 15 min each and rinsed with DI water. After an overnight air dry, the sample was sputter coated with Au and imaged using a SEM (Hitachi SU8230).

3.2.10 Dynamic mechanical analysis

Dynamic mechanical analysis (DMA) was performed on blood clots using an ElectroForce 3100 (TA instruments, New Castle, DE). Three displacements (0.1 mm, 0.2 mm, and 0.5 mm) and three different frequencies (0.1 Hz, 1 Hz, and 10 Hz) were applied to observe the displacement dependency and quantify the frequency response (Figure 3-9). The compressive modulus was calculated from the magnitude of displacement curve and the force response curve per the usual definitions for DMA.

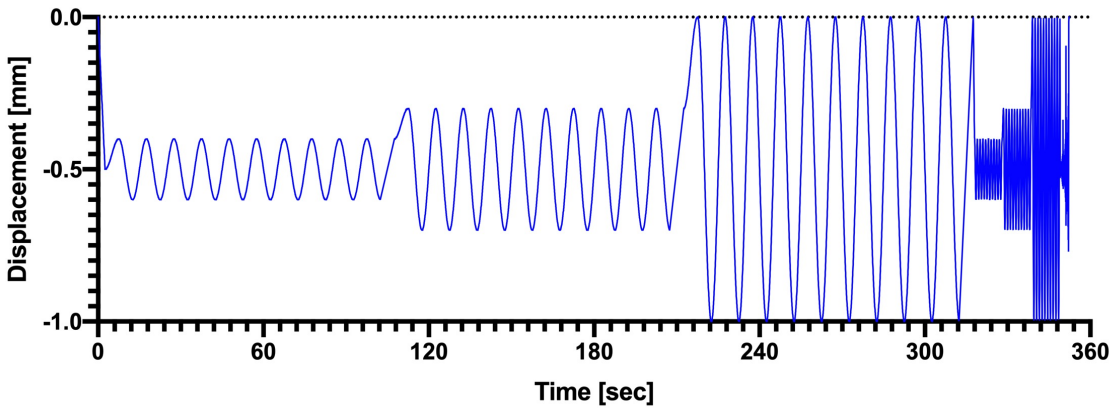

Figure 3-9. Input displacement for DMA of the blood clots.

3.2.11 Analysis

A one-way ANOVA was used to test for statistical differences between groups with the significance set at $p < 0.05$ (GraphPad Prism 7, GraphPad Software, San Diego, CA). All data are presented as the mean ± standard deviation unless otherwise noted.

3.3 Results

3.3.1 A SIPA clot is more permeable than a coagulation clot

The SIPA clots were all significantly more permeable than the coagulation clots (Figure 3-10). Wufsus et al. (2013) quantified the permeability of platelet-rich clots formed under static conditions with platelet volume fractions ranging from 0.31 to 0.61. The coagulation clot permeability measured in the present study was $5\times10^{-4} \pm 5\times10^{-4}$ μm^2, which fits in the permeability range reported by Wufsus et al. (2013) ($1.5 \times 10^{-5} \pm 3.3 \times 10^{-6}$ to $6.1 \times 10^{-3} \pm 1.1 \times 10^{-3}$ μm^2). On average, the SIPA clot was three orders of magnitude more permeable (0.3 ± 0.4 μm^2) than the red coagulation clot ($5 \times 10^{-4} \pm 5 \times 10^{-4}$ μm^2).

Kobayashi et al. (2016) used the same microfluidic chamber design and a constant pressure head of 4.8 mmHg and observed RBCs passing through the SIPA clot that developed. The velocity of the RBCs moving through the channels in the clot can be used to calculate its permeability. The velocity of the RBCs traveling in the central part of the channel was used as a superficial velocity ($v = Q/A$) in equation (5) to estimate the permeability (Figure 3-10; Kobayashi 2016). There was no statistical difference between the permeability calculated using Kobayashi et al. (2016)'s measurements and those obtained in our microfluidic chamber with a constant pressure head.

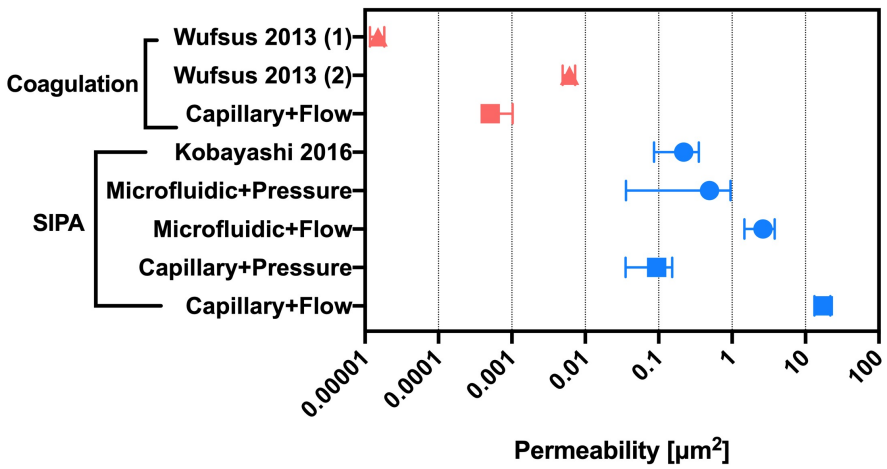

Figure 3-10. Permeability measurement results of the SIPA clot and coagulation clots. Wufsus et al. (2013) measured the permeability of coagulation clots with platelet concentrations of (1) 61% and (2) 31%. Compared to the coagulation clots, the SIPA clots showed significantly higher permeability ($p < 0.05$).

The permeabilities of the SIPA clots formed in the constant pressure experiments were lower than the permeabilities of those formed in the constant flow experiments. For the microfluidic chamber, the permeability was 0.5 ± 0.46 μm^2 for the constant pressure experiments but 2.6 ± 1.2 μm^2 for the constant flow experiments; for the capillary tube, the

permeability was $9.4 \times 10^{-2} \pm 5.9 \times 10^{-2}$ μm^2 vs. 17.5 ± 4.3 μm^2 for the constant pressure and flow experiments, respectively.

Under the constant flow condition, extremely high shear rates can be generated as a clot grows over time, and these extremely high shears may limit the thrombus growth. Limited thrombus growth can generate a gap (microfluidic chamber) or a hole (capillary tube) in the thrombus, which increases its average permeability (Figure 3-11A&B). The average hydraulic resistance is the parallel sum of the SIPA clot resistance (*Rc*) and the resistance of the large hole at the center (*Rp*). Thus, assuming Poiseuille's flow, the effect of the gap or the hole was excluded by simulating the gap height or measuring the hole diameter and subtracting its hydraulic resistance from the total value. When the effect of the gap or the hole was excluded, the permeability decreased and became close to the constant pressure results (Figure 3-11C).

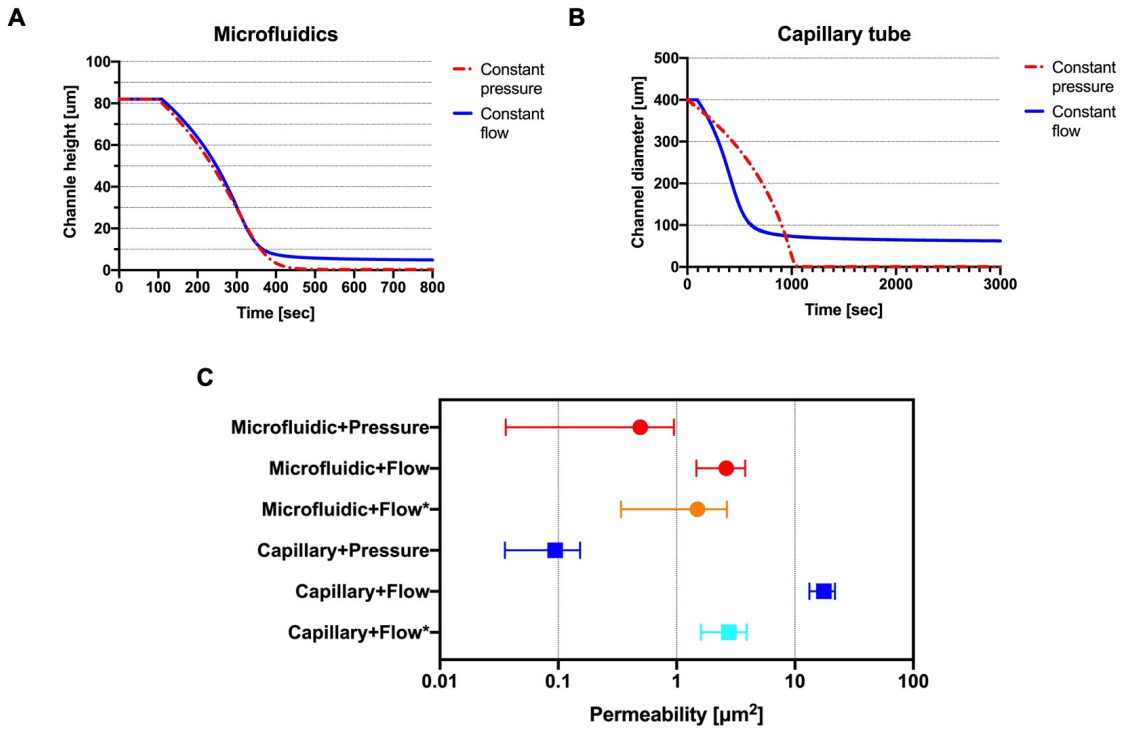

Figure 3-11. SIPA clot growth simulation of (A) the microfluidic chamber and (B) the capillary tube showing that the constant pressure condition completely occludes the channels, while the constant flow condition leaves (A) a gap or (B) a hole at the center. (C) SIPA clot permeability with the reflected effect (i.e., gap or hole) (*).

3.3.2 Porous structure of SIPA clot

Average values of measured clot length, cross section area, pressure head, and mass flow rate are summarized in Table 2. In microfluidic chamber, the clot length was more than 3 times longer when constant flow condition was applied compared to constant pressure. Mass flow rate was 3 to 5 orders of magnitude higher with constant flow condition than constant pressure for both high shear chambers. Multi-channel analysis was performed using values from Table 2, showing pore diameters ranging from 1 to 100 and pore numbers ranging from 1 to 100,000 (Figure 3-12). Kobayashi et al. (2016) observed RBCs (diameter = 6-8 μm) traveling through the SIPA clot, thus pore diameters are approximately 8 μm giving a porosity of about than 60% from ~5,000 pores.

Table 2. Average values of measured clot parameters and calculated permeability.

	Length [mm]	Area [mm^2]	Pressure [mmHg]	Mass flow rate [μL/min]	Permeability [μm^2]
Microfluidics + Pressure	0.09	0.039	4.78	0.04	0.49
Microfluidics + Flow	0.31	0.039	160	1.67	2.63, 1.5*
Capillary + Pressure	0.89	0.12	66	0.03	0.09
Capillary + Flow	0.83	0.1	260	1252	17.5, 2.76*

* SIPA clot permeability with the reflected effect of gap or hole (Figure 3-11C).

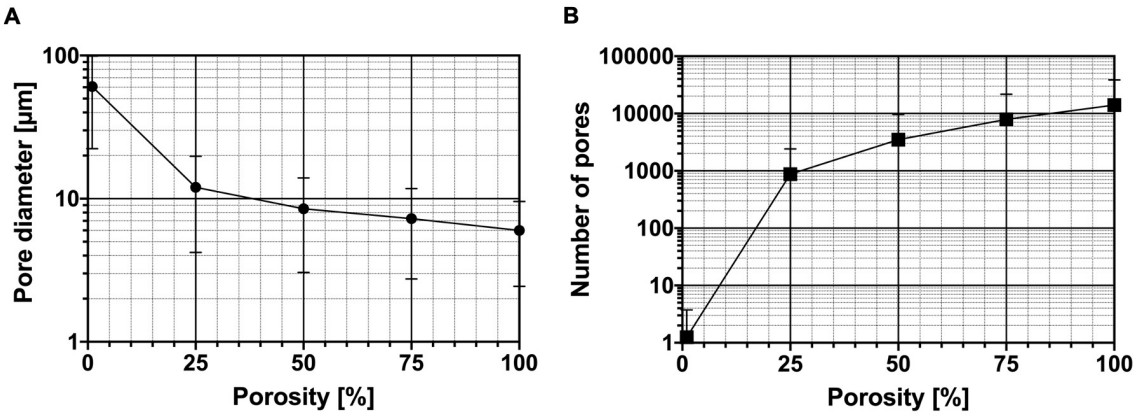

Figure 3-12. Multi-channel analysis result of SIPA clot. (A) Pore diameter ranged from 1 to 100 and (B) pore number ranged from 1 to 10,000.

3.3.3 SIPA clot has greater breakage strength than coagulation clot

In average, SIPA clot resisted pressure gradient of 160 mmHg for microfluidics and 260 mmHg for capillary tubes. In turn, the SIPA clots demonstrated an breakage strength of 4.6 ± 1.3 kPa, which was 7 times significantly stronger than the coagulation clots, which had an breakage strength of 0.63 ± 0.3 kPa (Figure 3-13, $p < 0.05$). The type of stenotic chamber difference did not significantly change the breakage strength of the SIPA clots (microfluidic vs. capillary tube). And the surface with or without collagen type 1 did not significantly impact the breakage strength of the coagulation clots.

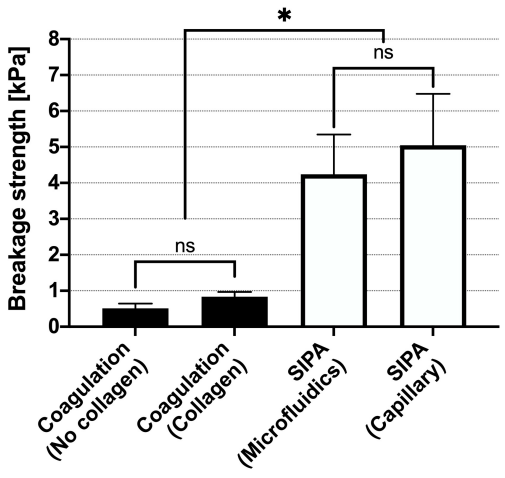

Figure 3-13. The SIPA clots showed significantly higher breakage strength (* $p < 0.05$) than the coagulation clots. The presence (n = 3) or absence (n = 3) of a collagen surface did not significantly impact coagulation clot strength. Whether the stenotic chamber was a microfluidic chamber (n = 7) or a capillary tube (n = 7) did not significantly changed SIPA clot breakage strength.

3.3.4 A SIPA clot generation in a closed flow loop

Porcine WB was perfused into a closed *in vitro* flow loop (Figure 3-3C) to generate a large SIPA clot in order to investigate its structure and mechanical strength. The large glass tube (Figure 3-14A) had an inner diameter of 12 mm and 80% stenosis in diameter. Reynolds number was 334 (Table 3) and flow separation was seen during perfusion similar to the capillary tube experiment where Re = 162. Flow separation was not found in the microfluidic experiment where Re = 2.5. The white SIPA clot grew over time at the stenosis (Figure 3-14B), and the roller pump was manually adjusted to reduce the flow rate (Figure 3-15A). The maximum shear rate reached over 10,000 s^{-1} with the initial flow rate (Figure 3-15B), which is higher than microfluidics (Figure 2-3) or capillary tube but still in the range where RPA can occur (Mehrabadi et al., 2016). Eventually, the clot occluded the chamber and ceased the blood flow in 60 ± 17 minutes. All occlusive SIPA clots had a similar trumpet-like shape with the mouth opened against the flow (Figure 3-14C). Using

Mehrabadi et al. (2016)'s high shear thrombosis model (described in Ch2.2.2), the flow rate was simulated with the initial flow rate value from the experimental data (0.66 L/min). The simulated flow rate was lower in the 10-60-minute time frame but fell in the range of error and reached flow rate below 5 mL/min in 71 minutes (Figure 3-15A).

Table 3. Reynolds number and occlusion time of three high shear chambers with constant pressure head driven flow.

	Microfluidics	Capillary tube	Large tube
Minimum length scale [mm]	0.082	0.4	2
Reynolds number	2.5	162	334
Occlusion time [min]	1.4 ± 0.22	9.3 ± 0.9	60 ± 17

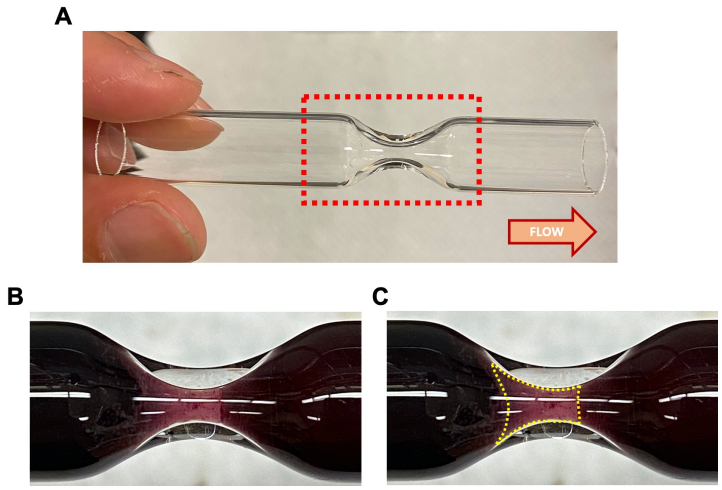

Figure 3-14. (A) Stenosed large glass tube coated with collagen type 1. (B) The SIPA clot shown in white formed at the stenosis region. (C) The SIPA clot boundary is highlighted in yellow.

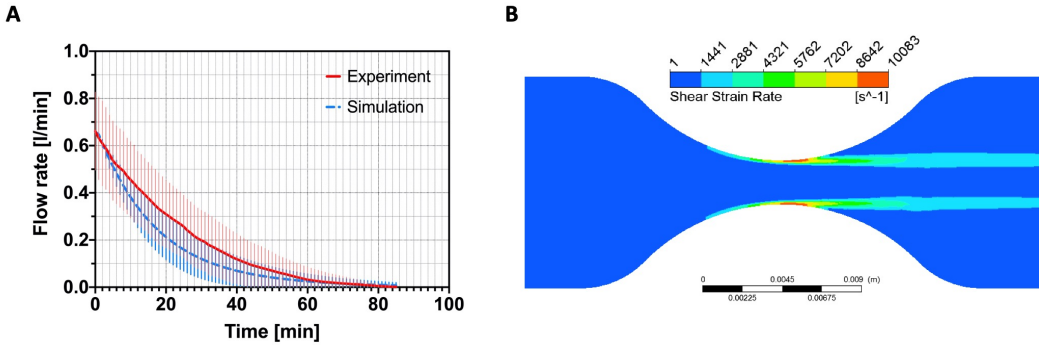

Figure 3-15. (A) Flow rate over time from the experiment (red, n = 11) and the simulation (blue). (B) Using the average value of the initial flow rate, CFD showed a maximum shear rate of 10,083 s^{-1} at the initial stage of perfusion.

3.3.5 Platelets are tightly packed in a SIPA clot

After the flow circuit was drained, the SIPA clot was retrieved (Figure 3-16A) from the large glass tube for the SEM imaging. The retrieved clot had a similar trumpet-looking shape to the one observed during the blood perfusion (Figure 3-14) and had different colors in characteristic regions. At the upstream and the downstream, there were transparent yellow parts that were originally detached from the glass wall. These parts initially had sheet-like morphology but were folded and tangled after the detachment. Right next to these regions were dark red colors that were expected to contain many RBCs. Lastly, the central part where the stenosis had been located had a light red or pink color. This stenotic region was expected to incorporate billions of platelets because SIPA was expected to occur here. After formalin fixation and dehydration (Figure 3-16B), the clot was cut in half in the flow direction to image the inner part of the clot (Figure 3-16C). The cross-section showed a finger- or mountain-like structure protruding towards the lumen (Figure 3-16D & E). This mountain structure was not found in the SEM images. To compare each region, the clot was split into four regions for low magnification images and nine ROIs (A-I) for moderate to high magnification images (Figure 3-16F). Geological shapes were seen in the low magnification images (Figure 3-17 to Figure 3-20) with layers of aggregates and some fibers. Meanwhile, the moderate magnification images displayed aggregates of numerous spheres that were approximately 2 μm in diameter, which were expected to be platelets (Figure 3-21 to Figure 3-38). The platelet aggregates were well captured in the high magnification images. Regions E, F, and G, where SIPA was expected to be maximal,

showed tightly packed platelets. To quantify how many platelets were packed in the clot, recognizable spheres with a diameter greater than 1.5 µm were manually counted in the high magnification SEM images. The G region had the highest density of spheroid platelets (0.23 platelets/µm^2), while the I region had the lowest (0.01 platelets/µm^2) (Figure 3-39). In the stenotic region (C-G), D region showed the lowest platelet density compared to the other regions. In Figure 3-28, D region is occupied with smooth surfaces and small granules that have a diameter less than 1 µm, presumably activated platelets and platelet-released granules. Assuming 2 µm platelet thickness and an average value of 0.1 platelets/µm^2, platelet density per volume is 0.05 platelets/µm^3 and the total SIPA clot was calculated to contain 1.23 billion platelets.

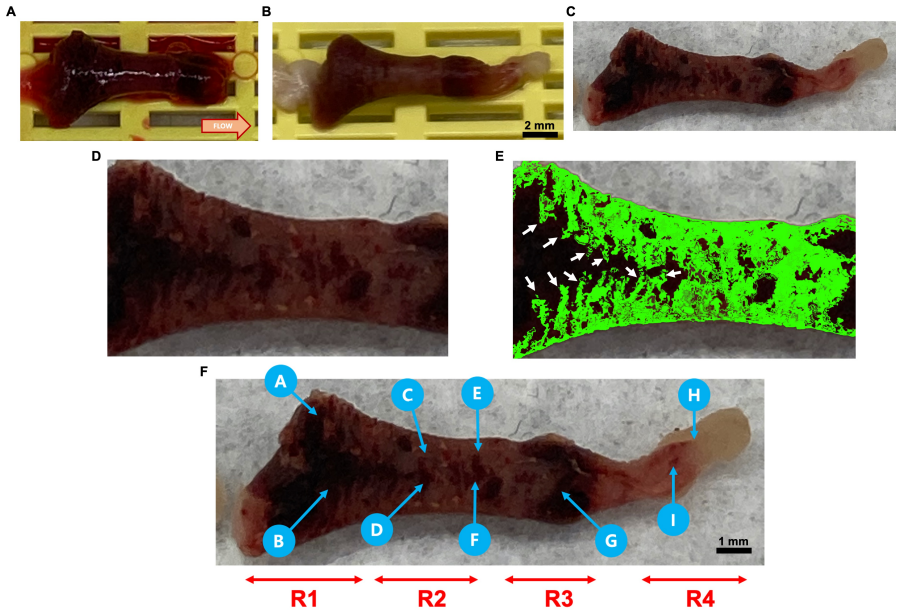

Figure 3-16. (A) A SIPA clot retrieved from the large glass tube was (B) formalin fixed and (C) dehydrated using ethanol and cut in half to expose cross section. (D) Magnified view of stenotic part of the clot. (E) Platelet-rich white region is highlighted in green showed mountains of platelet aggregates (white arrows). (F) Regions of interest are specified in.

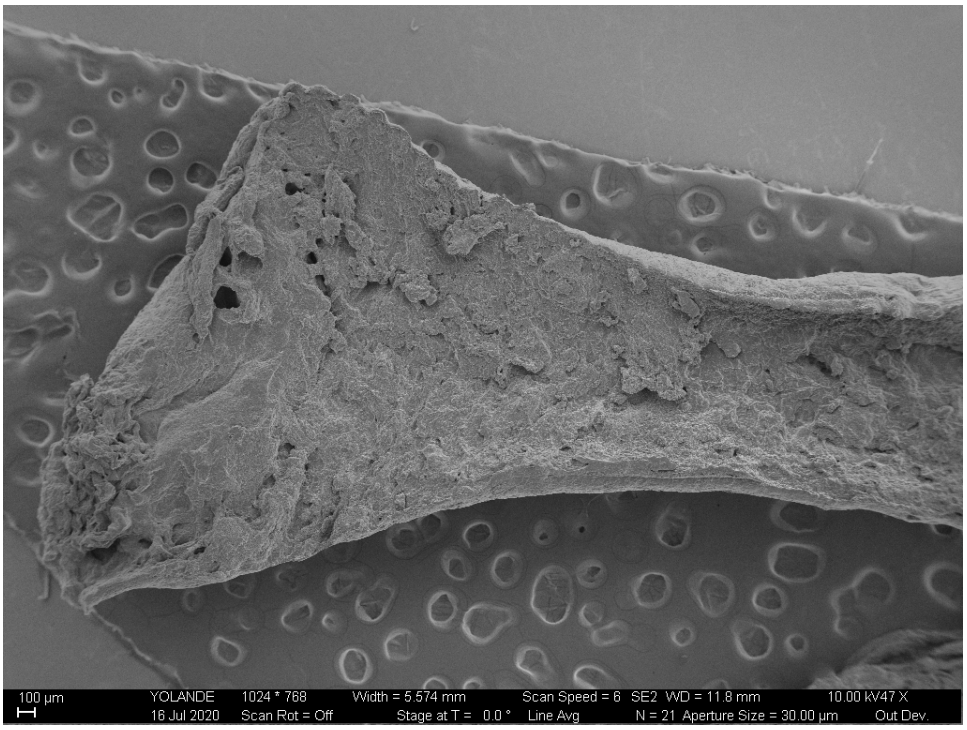

Figure 3-17. SEM image of the SIPA clot (R1).

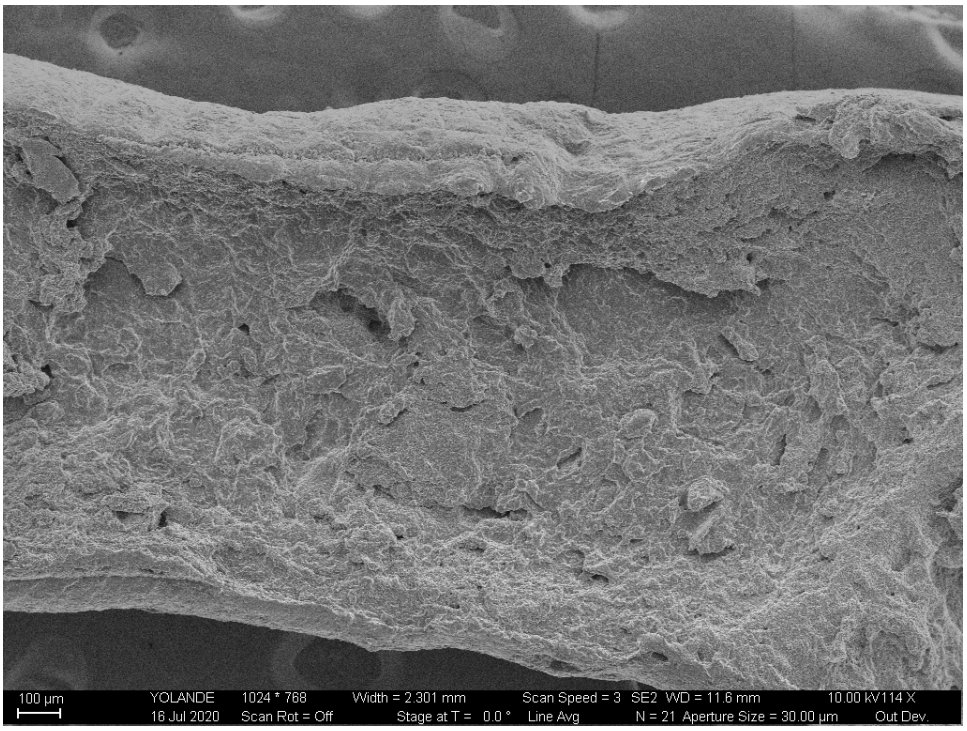

Figure 3-18. SEM image of the SIPA clot (R2).

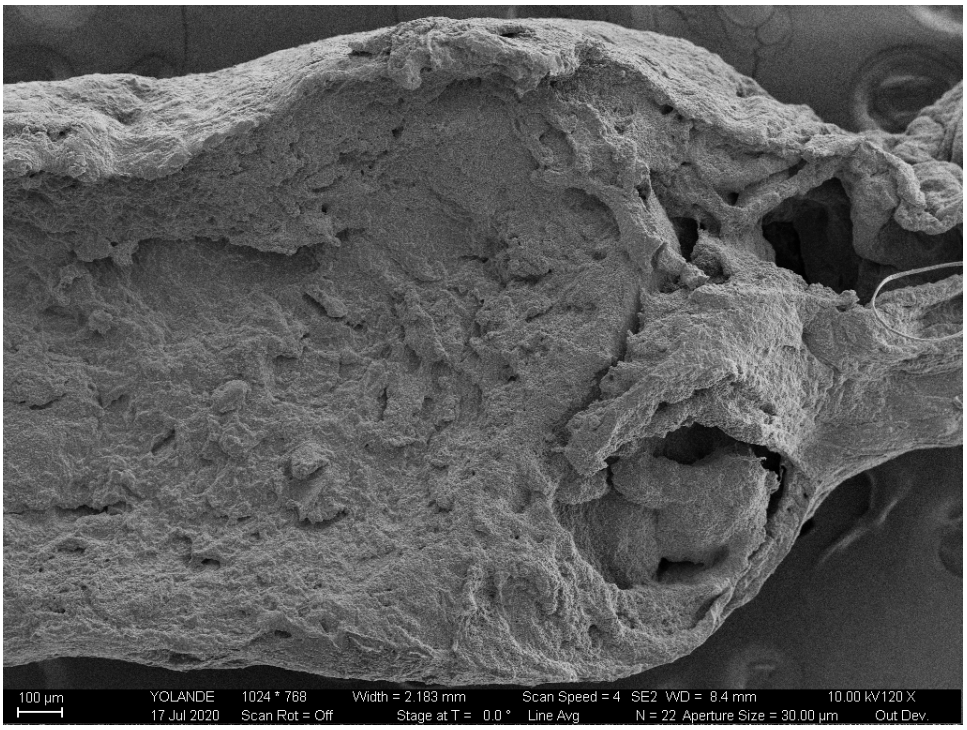

Figure 3-19. SEM image of the SIPA clot (R3).

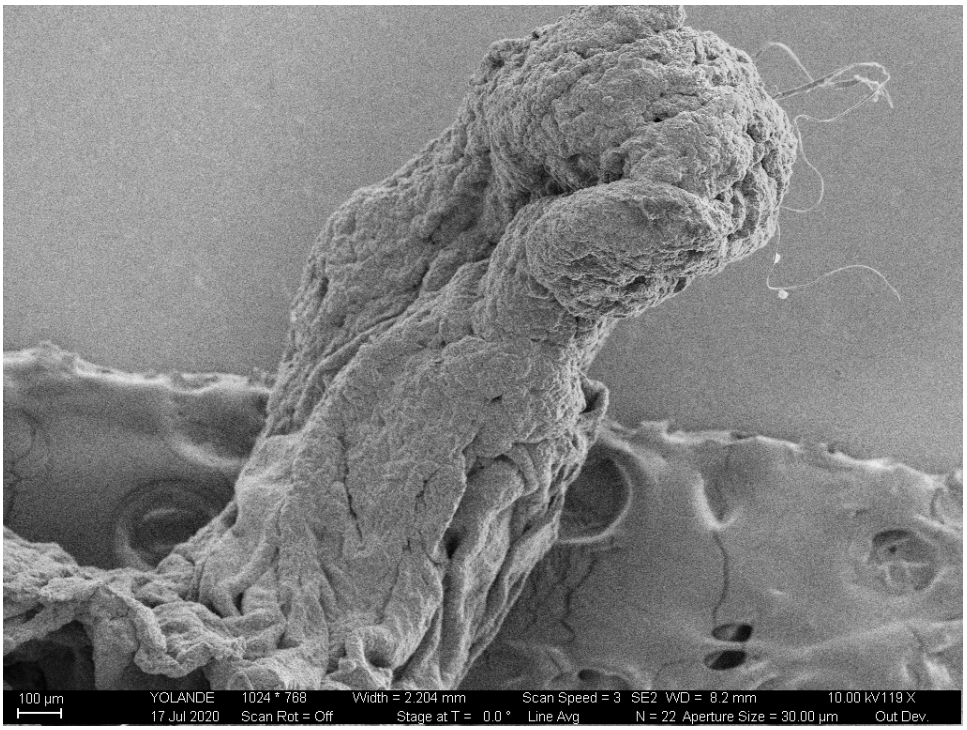

Figure 3-20. SEM image of the SIPA clot (R4).

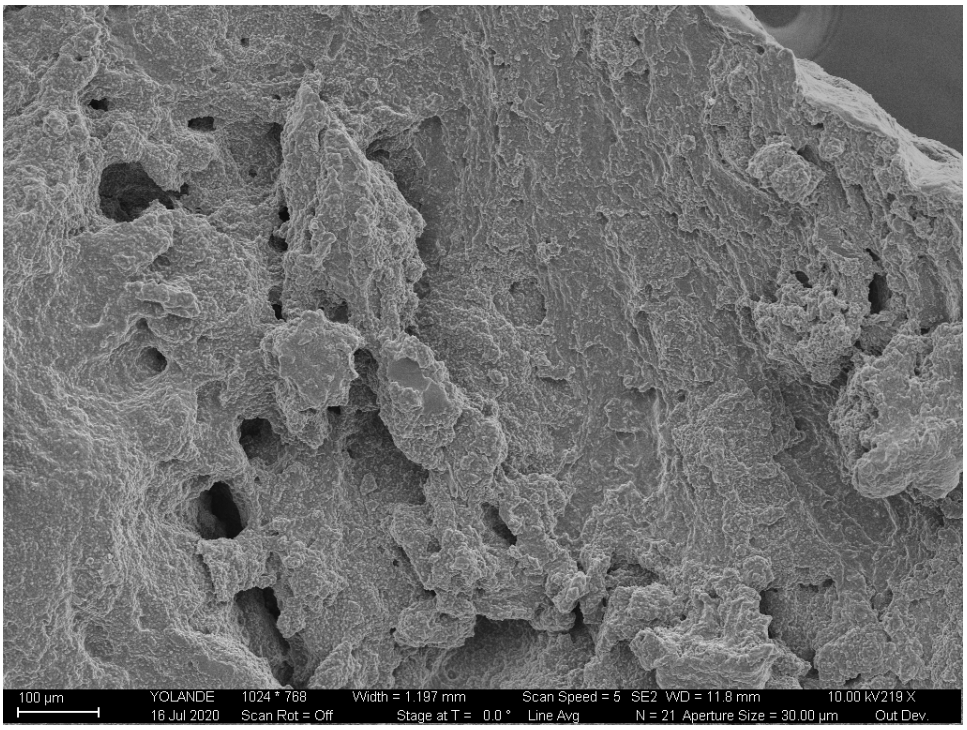

Figure 3-21. SEM image of the SIPA clot (A).

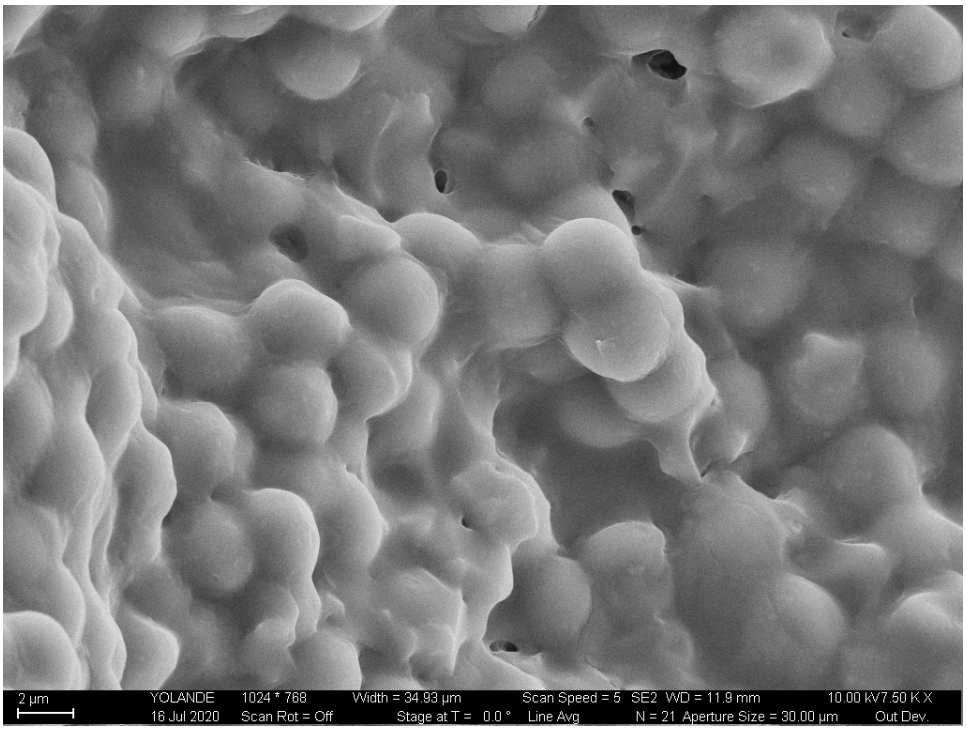

Figure 3-22. SEM image of the SIPA clot (A) with high magnification.

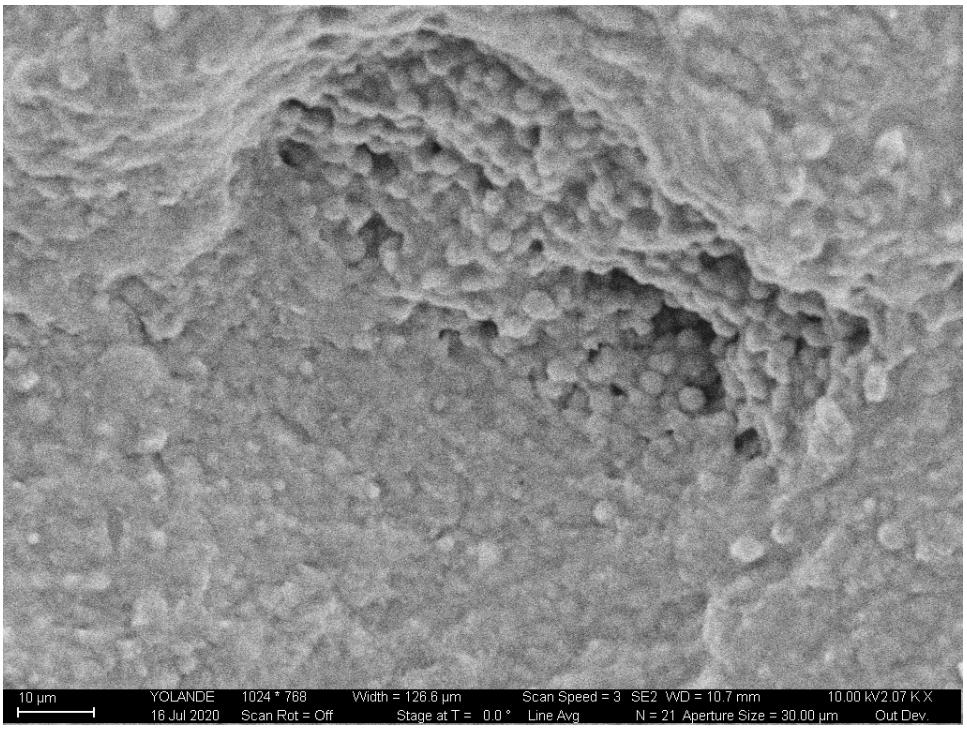

Figure 3-23. SEM image of the SIPA clot (B).

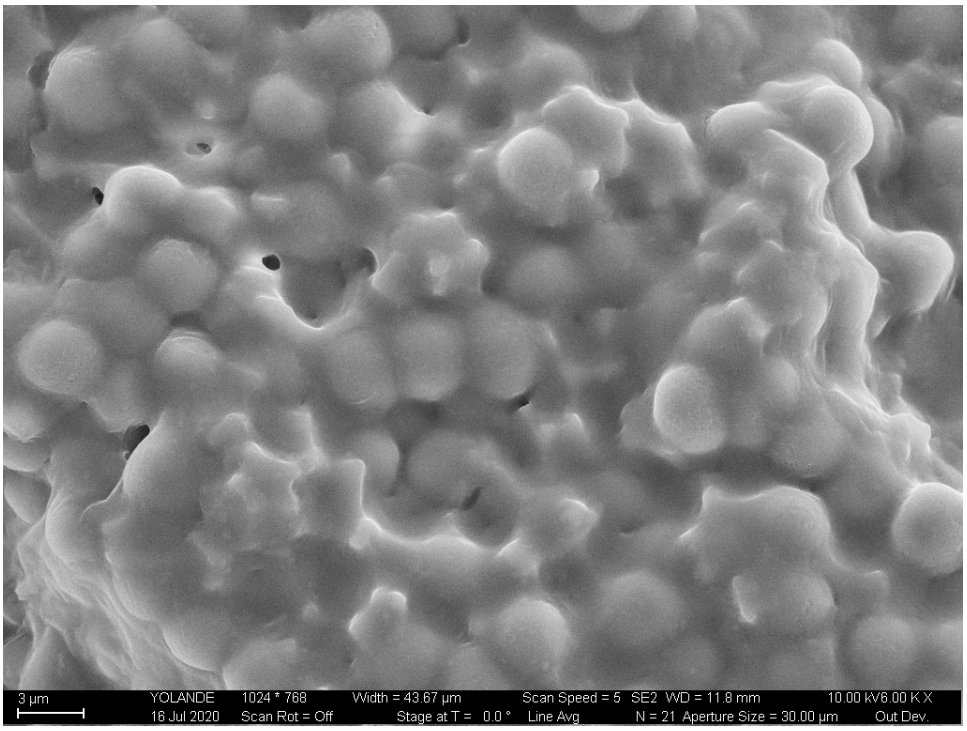

Figure 3-24. SEM image of the SIPA clot (B) with high magnification.

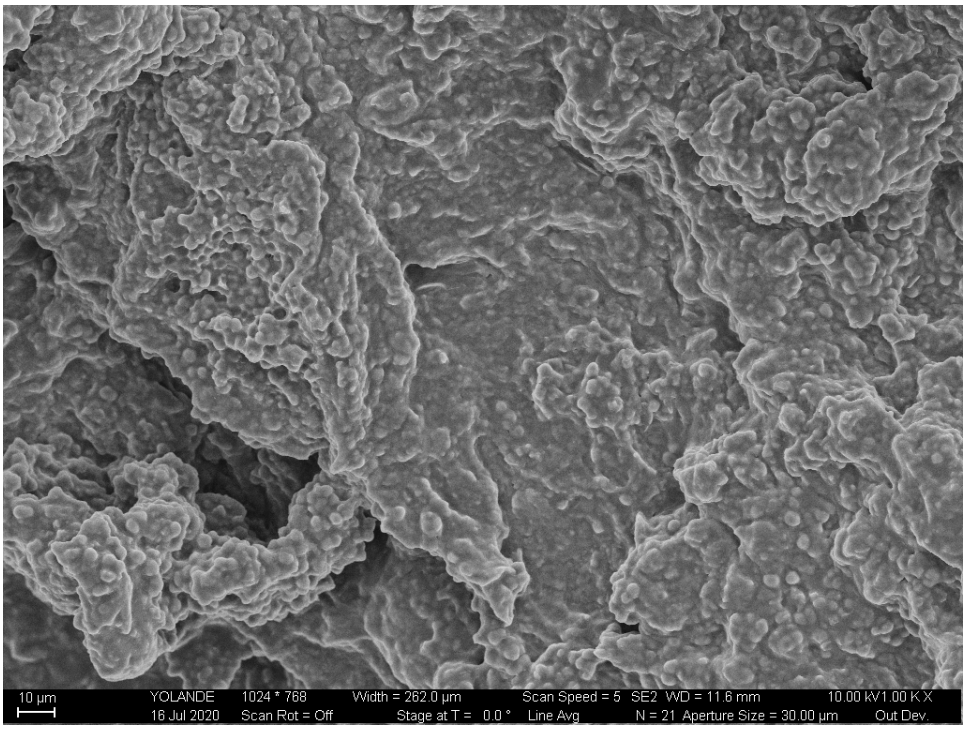

Figure 3-25. SEM image of the SIPA clot (C).

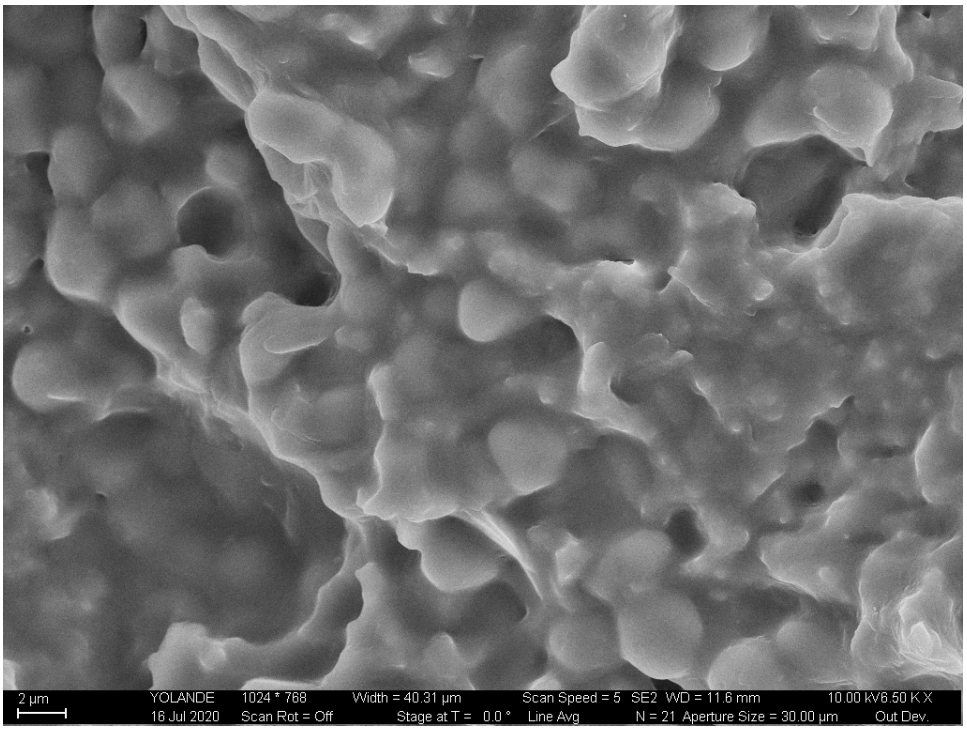

Figure 3-26. SEM image of the SIPA clot (C) with high magnification.

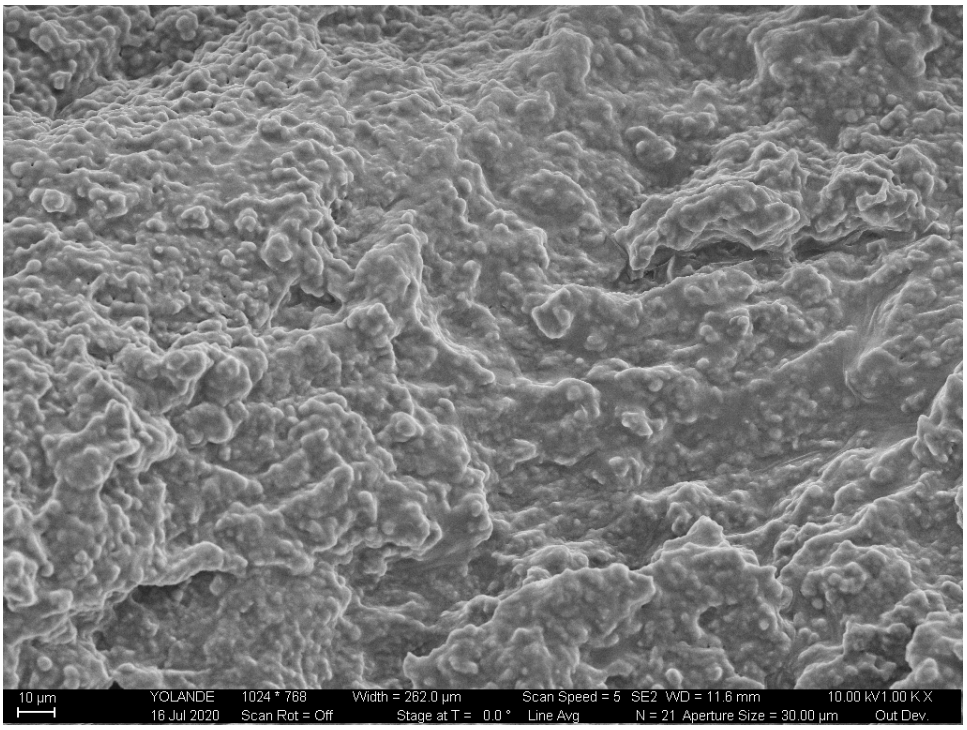

Figure 3-27. SEM image of the SIPA clot (D).

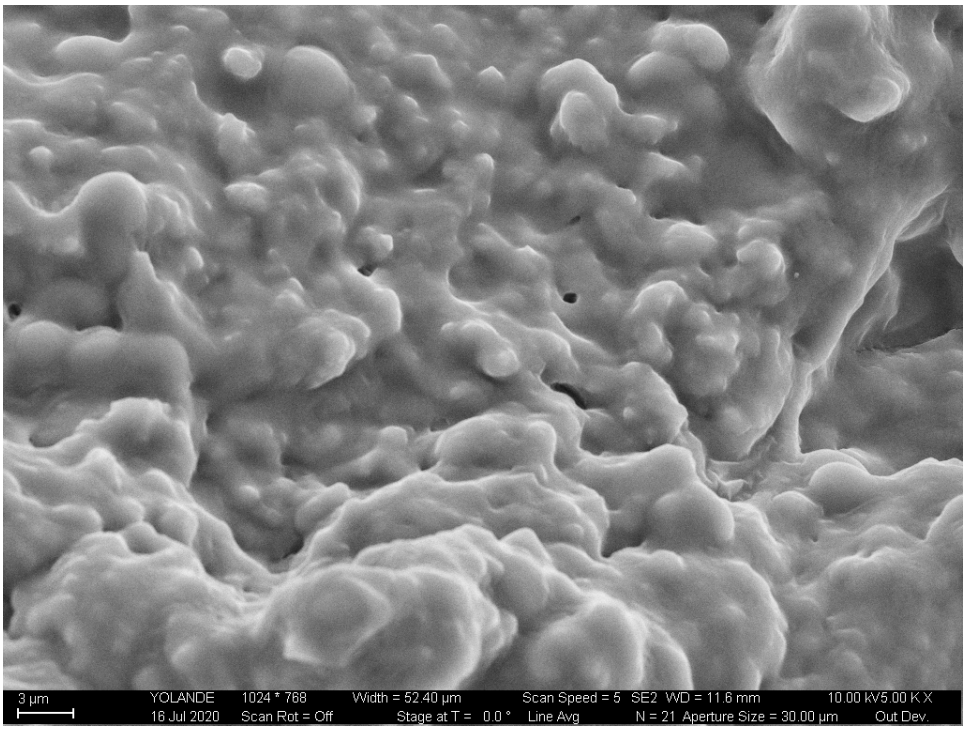

Figure 3-28. SEM image of the SIPA clot (D) with high magnification.

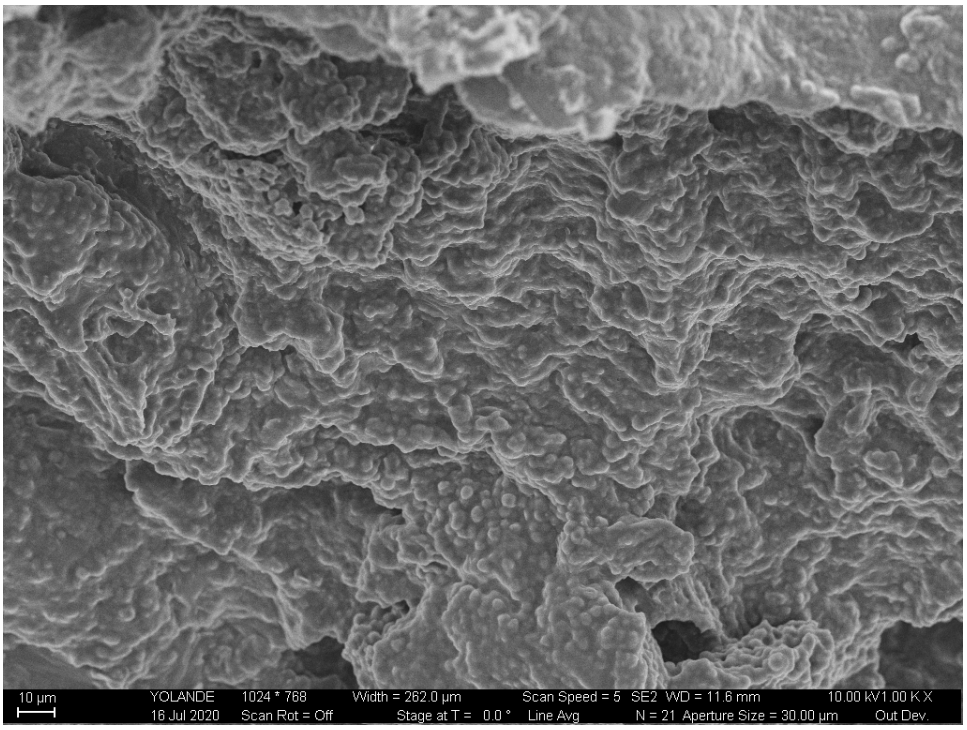

Figure 3-29. SEM image of the SIPA clot (E).

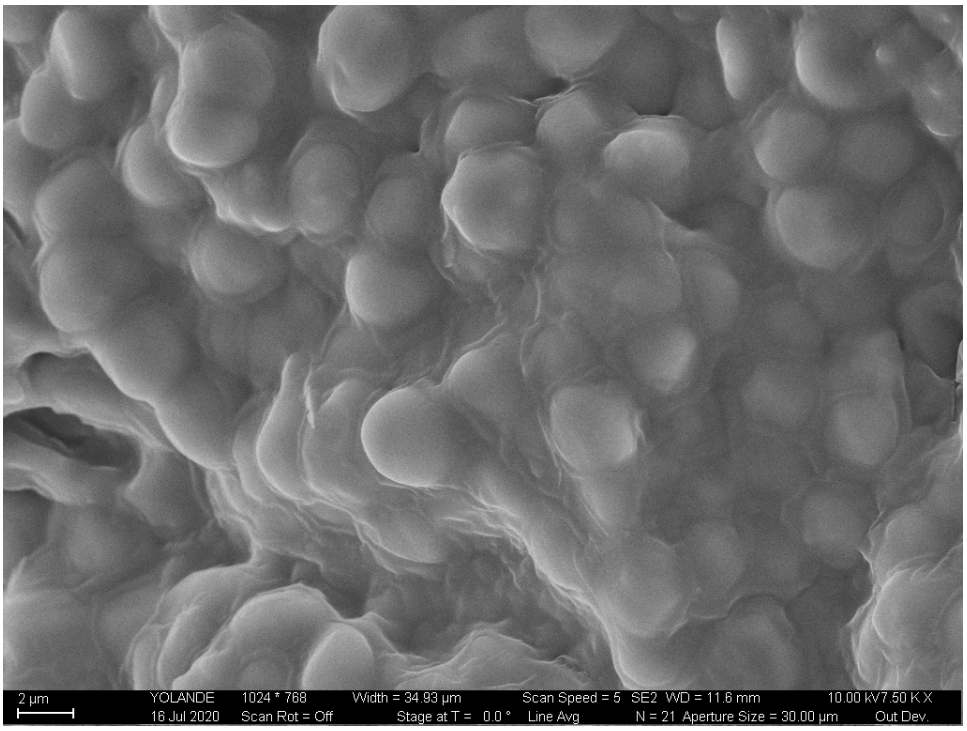

Figure 3-30. SEM image of the SIPA clot (E) with high magnification.

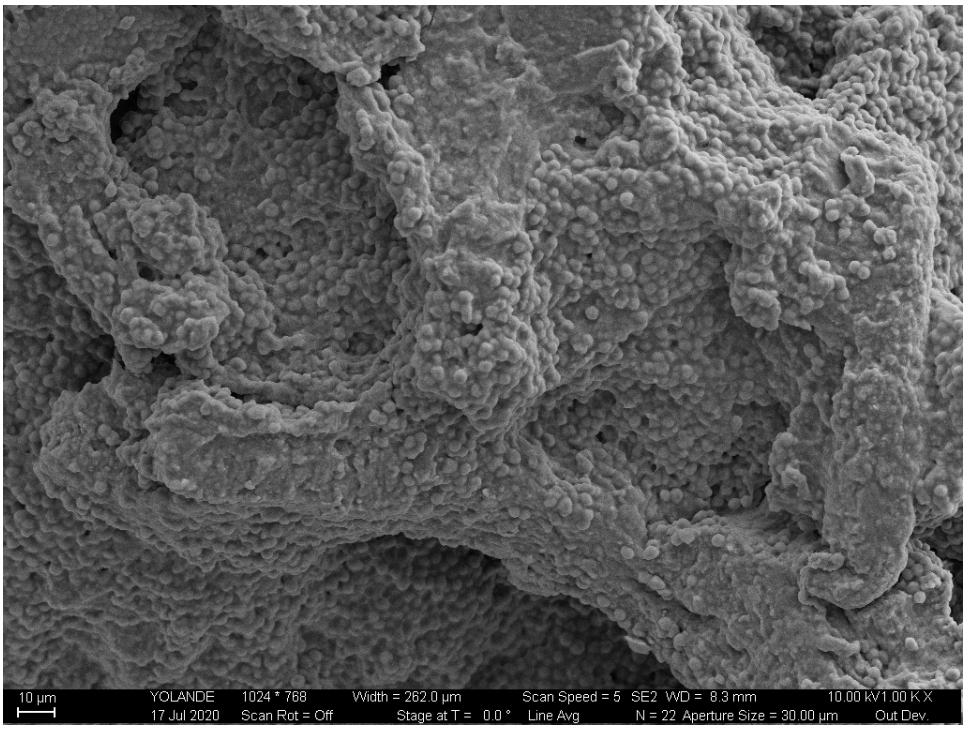

Figure 3-31. SEM image of the SIPA clot (F).

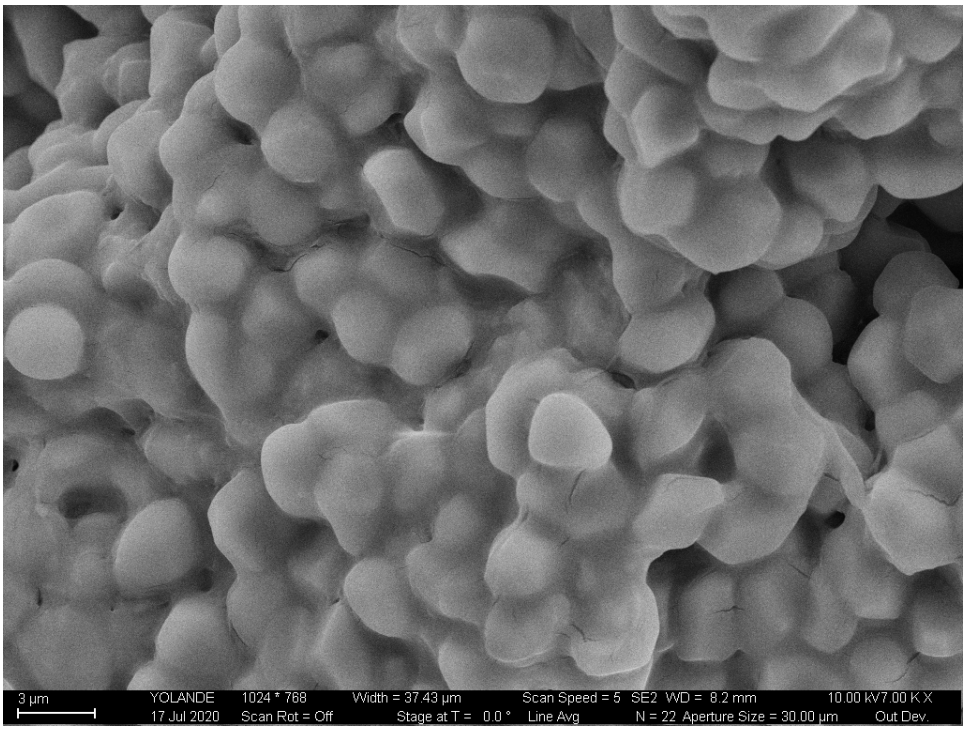

Figure 3-32. SEM image of the SIPA clot (F) with high magnification.

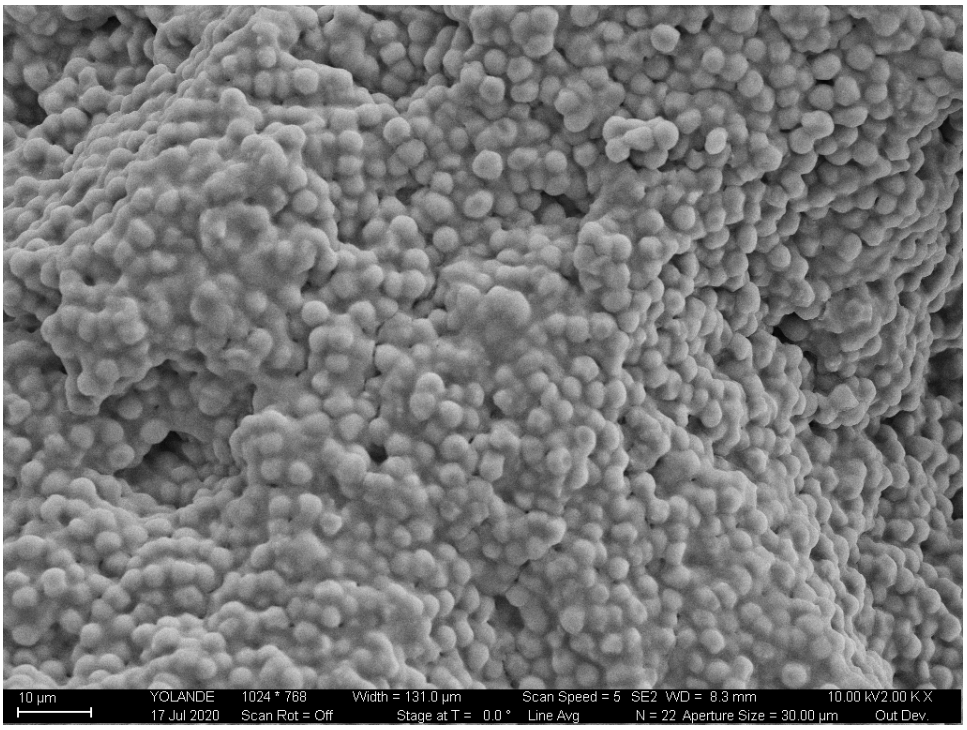

Figure 3-33. SEM image of the SIPA clot (G).

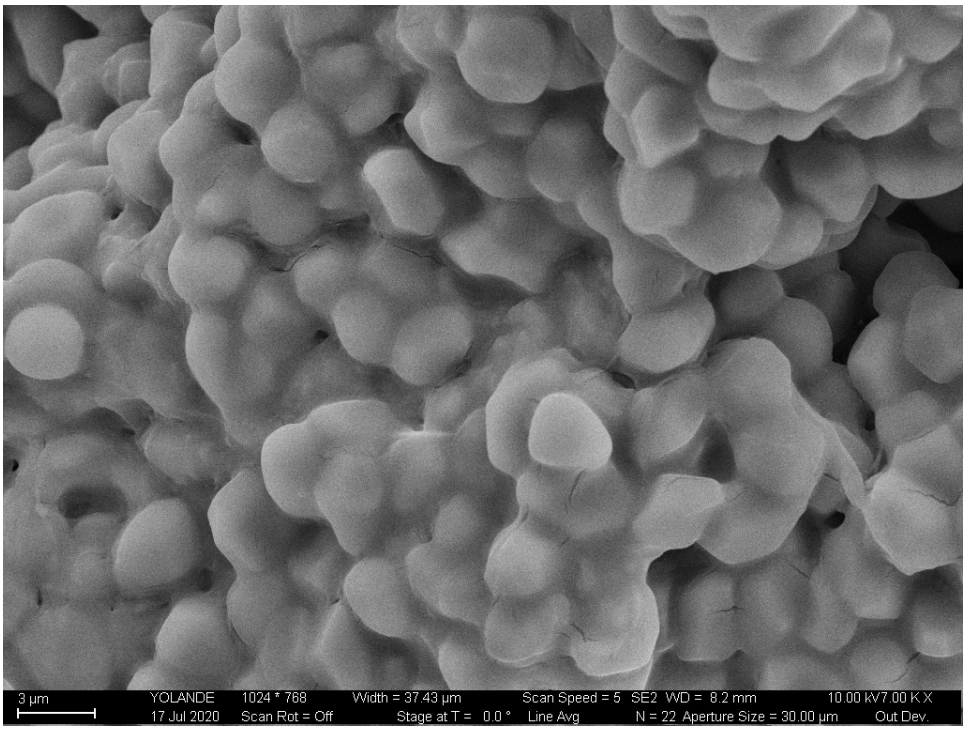

Figure 3-34. SEM image of the SIPA clot (G) with high magnification.

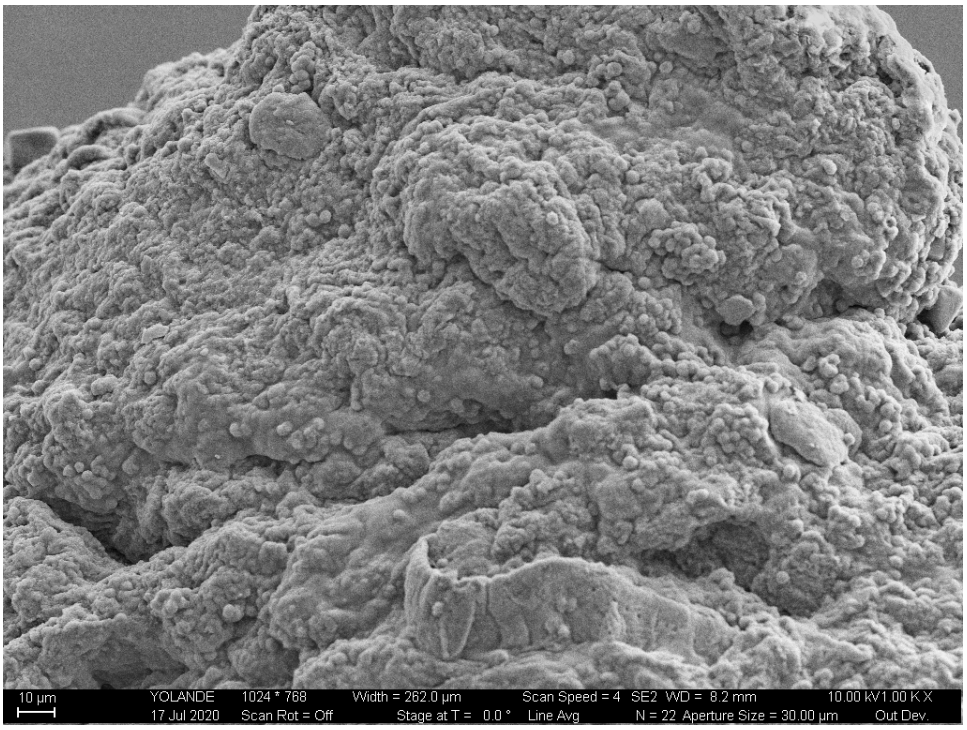

Figure 3-35. SEM image of the SIPA clot (H).

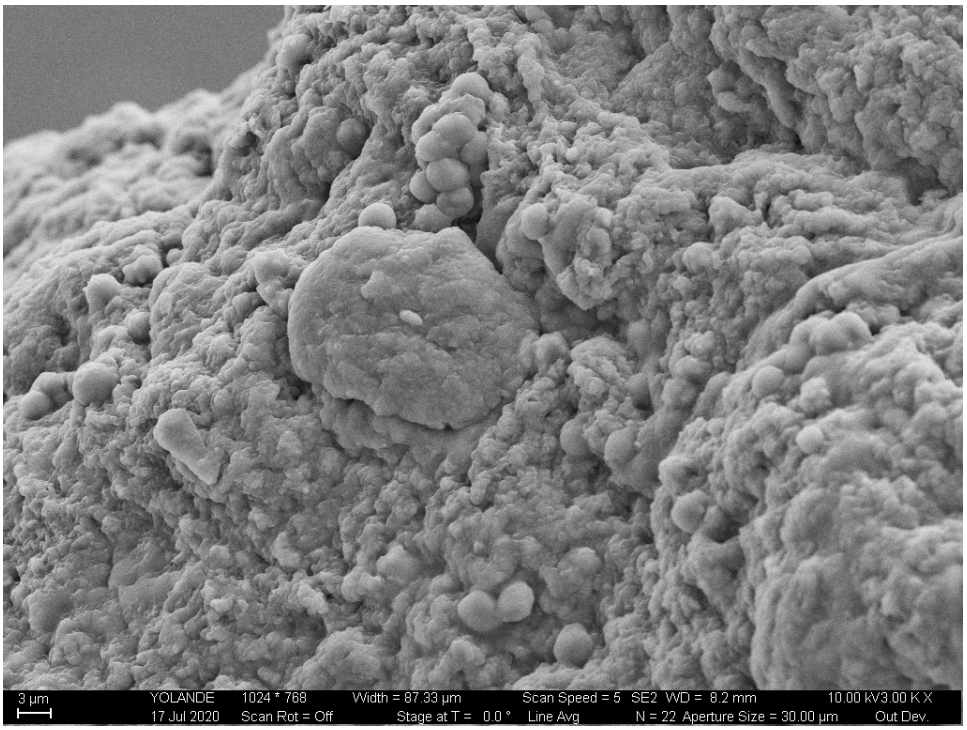

Figure 3-36. SEM image of the SIPA clot (H) with high magnification.

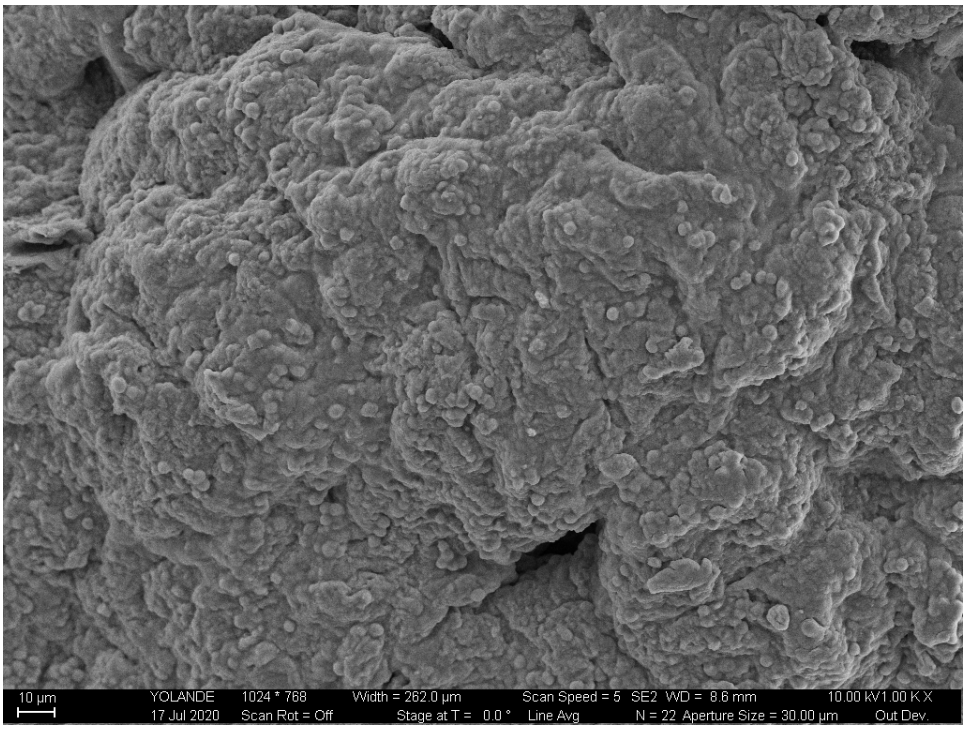

Figure 3-37. SEM image of the SIPA clot (I).

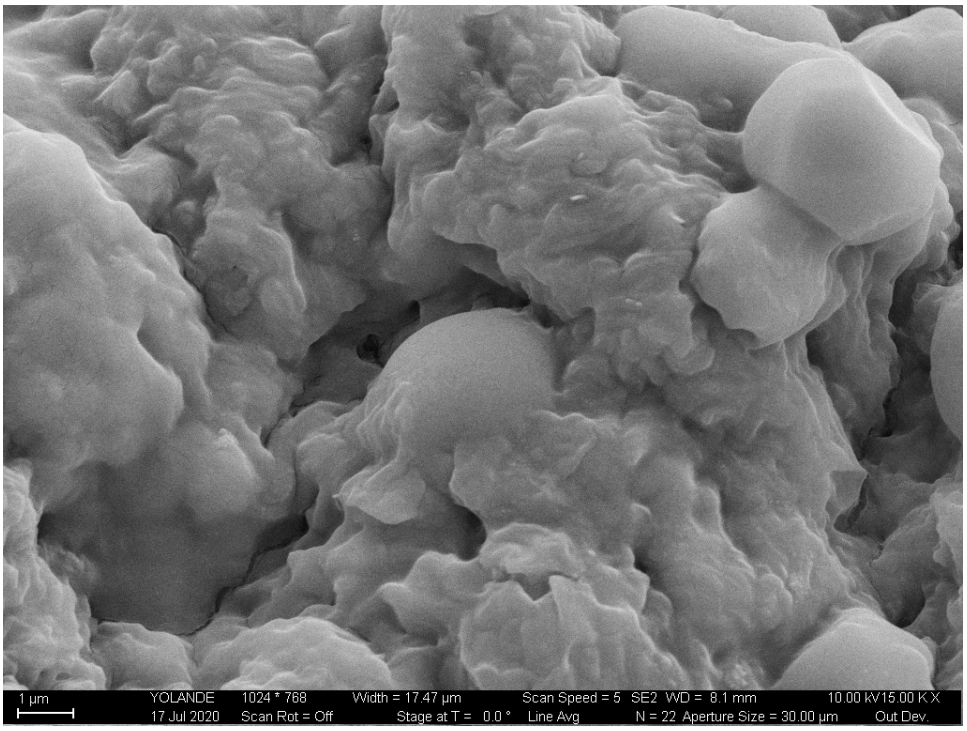

Figure 3-38. SEM image of the SIPA clot (I) with high magnification.

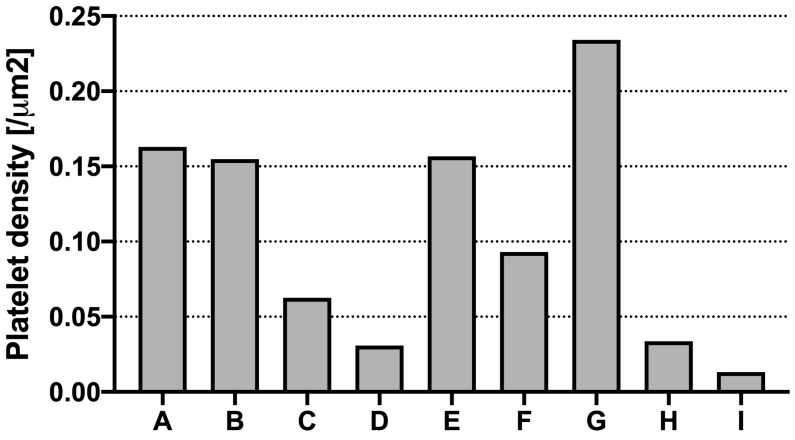

Figure 3-39. Unactivated platelet density of each region taken by SEM.

3.3.6 A SIPA clot is VWF-platelet-rich and has a porous structure

Two SIPA clots were stained using the Carstairs or VWF immunostaining method. One clot was sectioned in a longitudinal direction, and the other was sliced in a transverse direction. Consistent with the SEM results in Ch3.3.5, Carstairs staining showed that the SIPA clot was dominantly occupied by platelets (blue, Figure 3-40) and immunostaining result displayed that VWF was present throughout the SIPA clot (Figure 3-41), proving that the SIPA clot is VWF and platelet rich. Meanwhile, although coagulation cascade can't occur due to pathological high shear conditions as discussed in CH1.3, the Carstairs staining also revealed a little RBCs (yellow) and fibrin (red) in the clot (Figure 3-40). Presumably, RBCs become trapped and fibrin was formed in stagnant regions after occlusive SIPA clot formation. Thus, the void region and the space occupied by RBCs and fibrin are assumed to be pores or valleys that were formed during SIPA clot formation.

The SIPA clots were similar in appearance, macroscopically, as is seen in Figure 3-16. To explore each structure in detail, the clot was separated into six regions (L1 to L6, Figure 3-42A); the transparent parts at the each end (L1 and L6, Figure 3-42A) had fewer platelets than the central part of the clot, but these parts had more fibrin (Figure 3-43) and VWF (Figure 3-44). In addition, dispersed platelet aggregates were surrounded by fibrins (Figure 3-45, Figure 3-46, and Figure 3-61). In L2 (Figure 3-42A), the platelets and trapped RBCs formed a stripe-like pattern (Figure 3-47). Similar to L1 and L6, the platelet aggregates were surrounded by fibrin and the RBCs were trapped in the space between the platelet aggregates (Figure 3-49). L3 and L4 were stenosis regions, where the highest shear rate and SIPA were expected to occur. These regions had axisymmetric structures with fewer trapped RBCs than L2, and the fibrins were concentrated at the center of the lumen (Figure 3-50 and Figure 3-52). In addition, a color gradation from light blue to dark blue to medium blue was seen from the wall to the center of lumen (Figure 3-52). L5 showed characteristic features in that the platelet aggregates were at the wall and protruded at the center, and the area between these regions was filled with RBCs and fibrin (Figure 3-55).

The other SIPA clot was sectioned in a transverse direction and stained using the Carstairs and VWF immunostaining method (T1 to T9, Figure 3-42B). Section T1 shows a large number of trapped RBCs and a small number of dispersed platelet aggregates with fibrins (Figure 3-62) and VWFs (Figure 3-63), which were found in L1. Section T2 shows a large hole at the center and trapped RBCs and some fibrins in the pores (Figure 3-64). The stenotic regions in sections T3 to T7 reveal lumen that were completely occluded by platelet aggregates with a number of pores filled with RBCs and fibrins (Figure 3-66 to Figure 3-74). In contrast, sections T8 and T9 have an RBC-rich region between the platelet

aggregates at the wall and the center of the lumen; this feature is consistent with L5 in the longitudinal slide (Figure 3-55). Color segmentation analysis of the histological images of the blood clots indicated differences in composition and porosity (Figure 3-80). SIPA clot was rich in platelets (60%) and had little fibrin of 4% whereas WB clot was RBC-rich (70%) and PRP clot was platelet-rich (90%) but not as porous as SIPA clot (5% vs. 37%).

Summarizing the findings from histology and SEM, the occluding middle section (L2-5 and T2-9 in Figure 3-42) was composed of dense platelets and VWF with little fibrin and many channels ranging from 10 to 100 μm. Histological images showed more than 70% of this middle section was platelets, implying that the SEM area without spherical platelets could be occupied by flat, activated platelets. The entrance region (T1) and exit region (T6) showed long VWF strands without large platelet aggregates under shear rates less than 1,400 s^{-1} (Figure **3**-**15**B). Stripes of platelet aggregates and trapped RBCs were found in L2 and L5, where more unactivated platelets found in these regions (A, B, and G) than L3-4 (C-F). Platelets in region L3-4 (C-D) were mostly misshapen consistent with prior activation, as this region is expected to experience high shear rate up to 9,000 s^{-1} (Figure **3**-**15**B). The end of thrombus (R5 and T8-9) showed a protruding central core of dense platelets that appear not to have activated where the SEM images are of captured, round platelets (G). Surrounding the core was an annulus without thrombus where recirculation and low shear rate is expected to occur. At the wall is a thin ring of VWF and small aggregates hugging the surface and extending throughout the recirculation region.

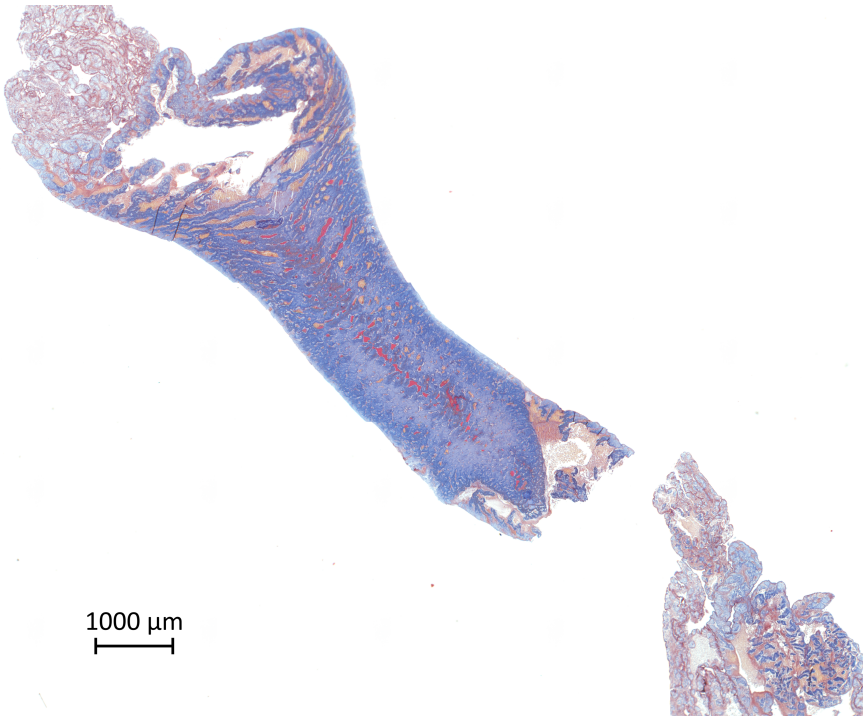

Figure 3-40. Carstairs staining of the SIPA clot in the longitudinal direction.

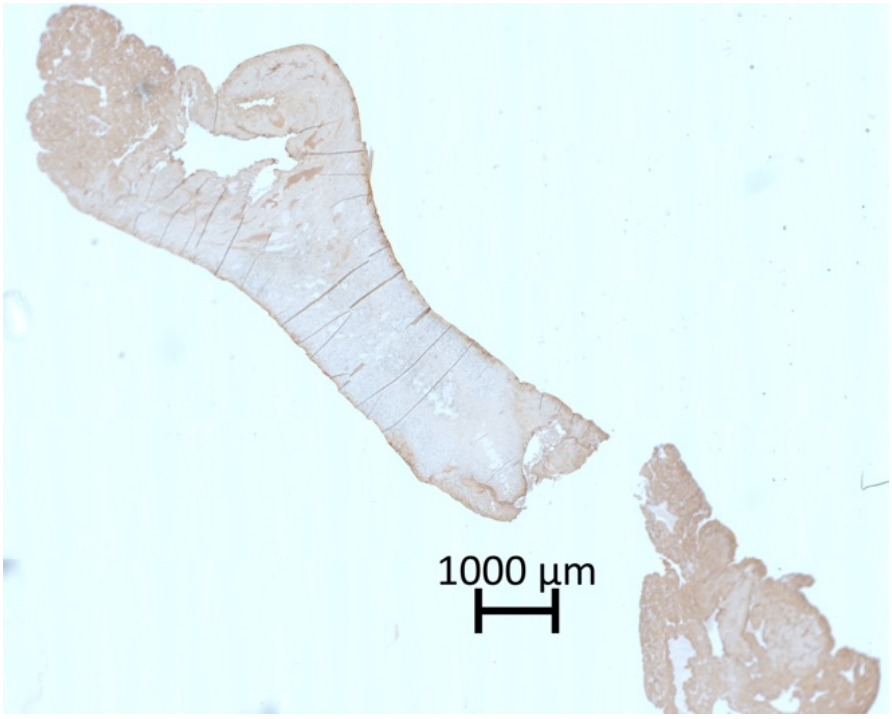

Figure 3-41. VWF staining of the SIPA clot in the longitudinal direction.

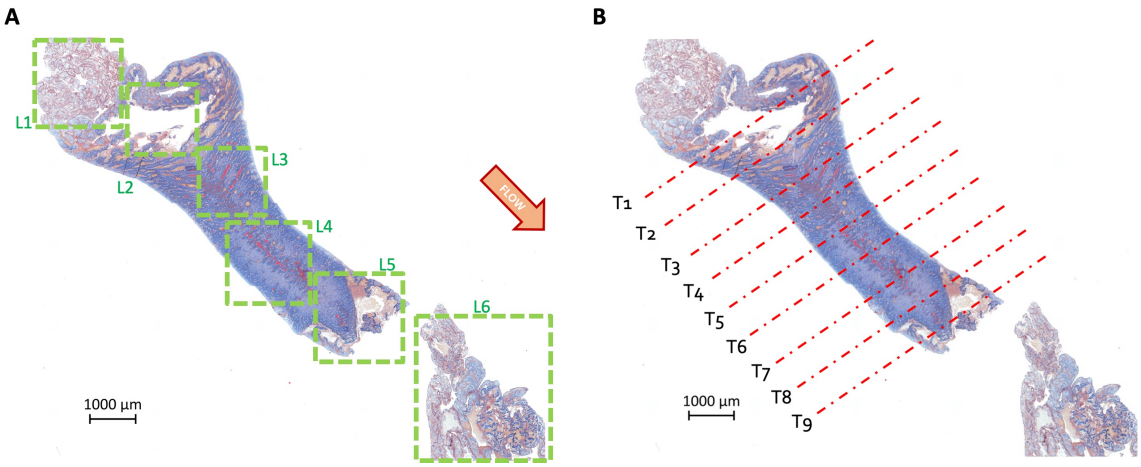

Figure 3-42. (A) Regions of interest from the longitudinal slide (L1-6). (B) Approximate locations of the cross sections (T1-8).

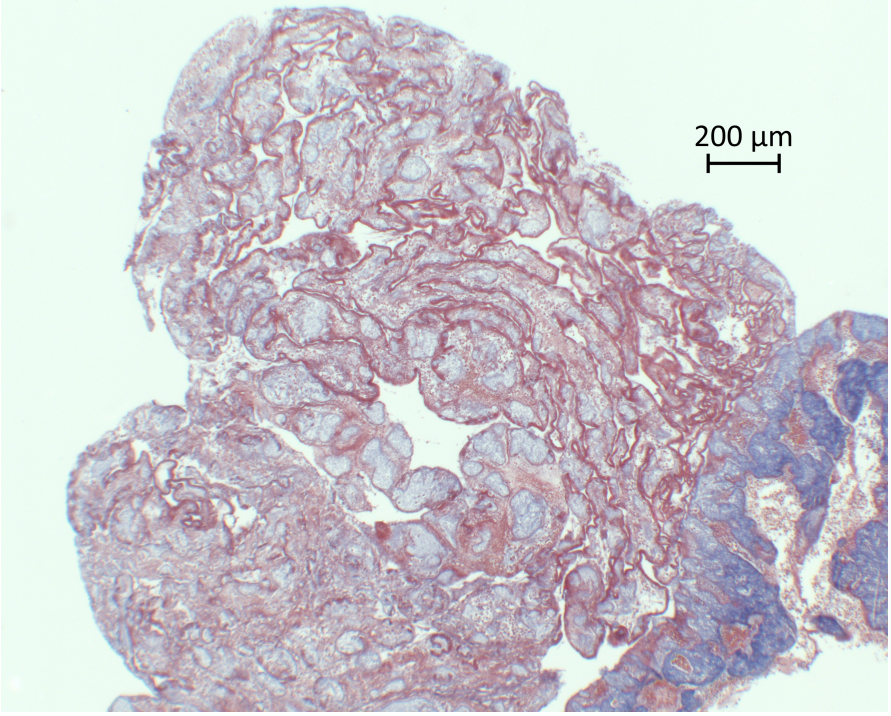

Figure 3-43. Carstairs staining of the SIPA clot in the longitudinal direction (L1, 5x magnification).

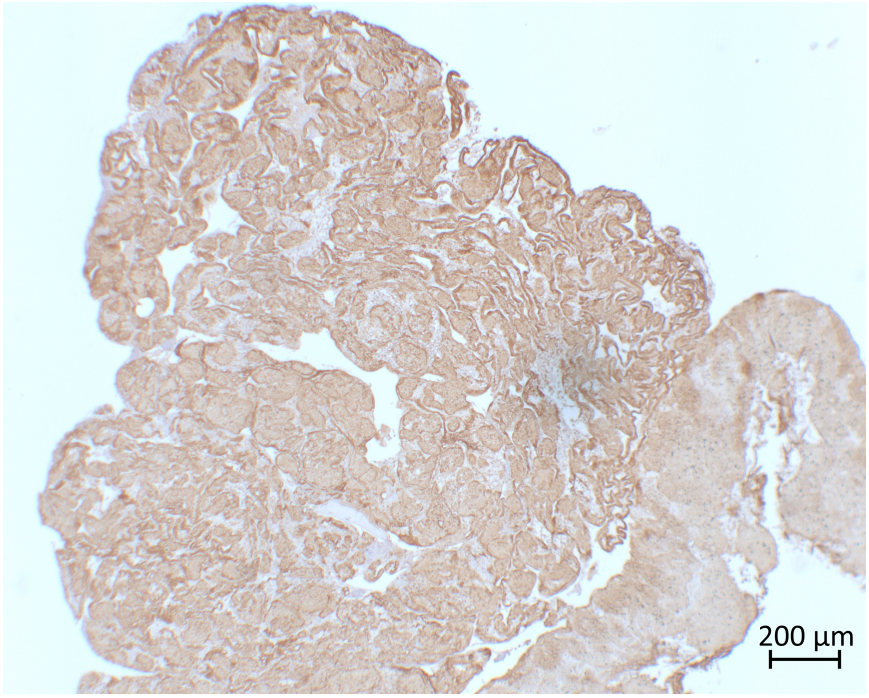

Figure 3-44. VWF staining of the SIPA clot in the longitudinal direction (L1, 5x magnification).

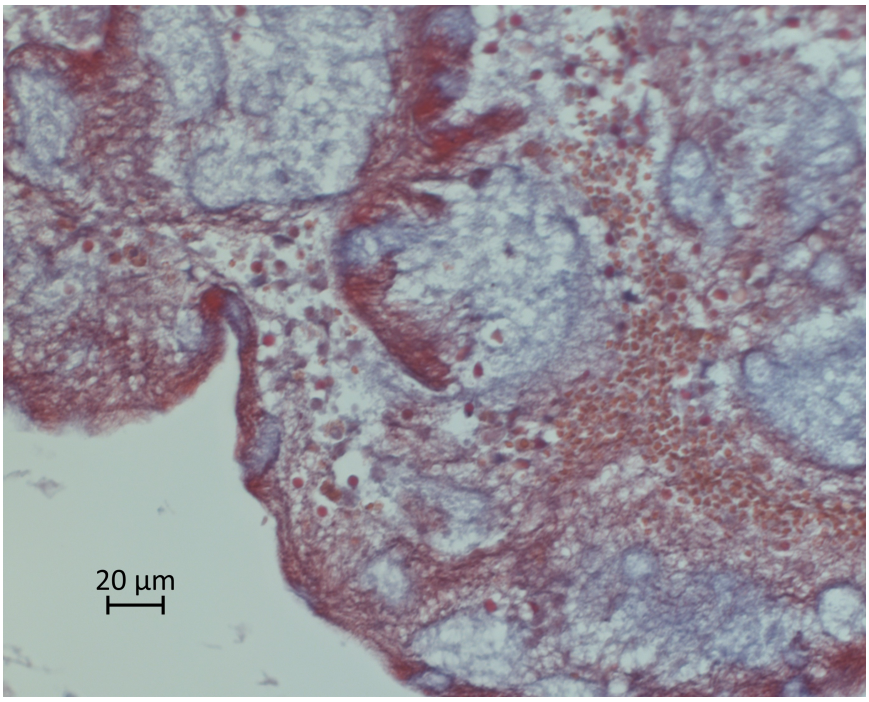

Figure 3-45. Carstairs staining of the SIPA clot in the longitudinal direction (L1, 40x magnification).

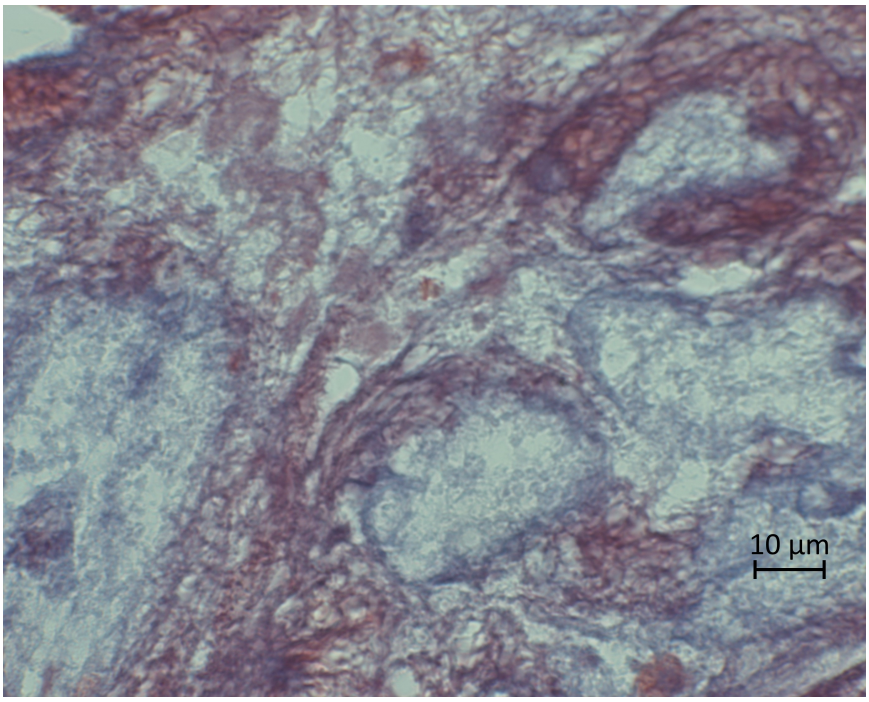

Figure 3-46. Carstairs staining of the SIPA clot in the longitudinal direction (L1, 100x magnification).

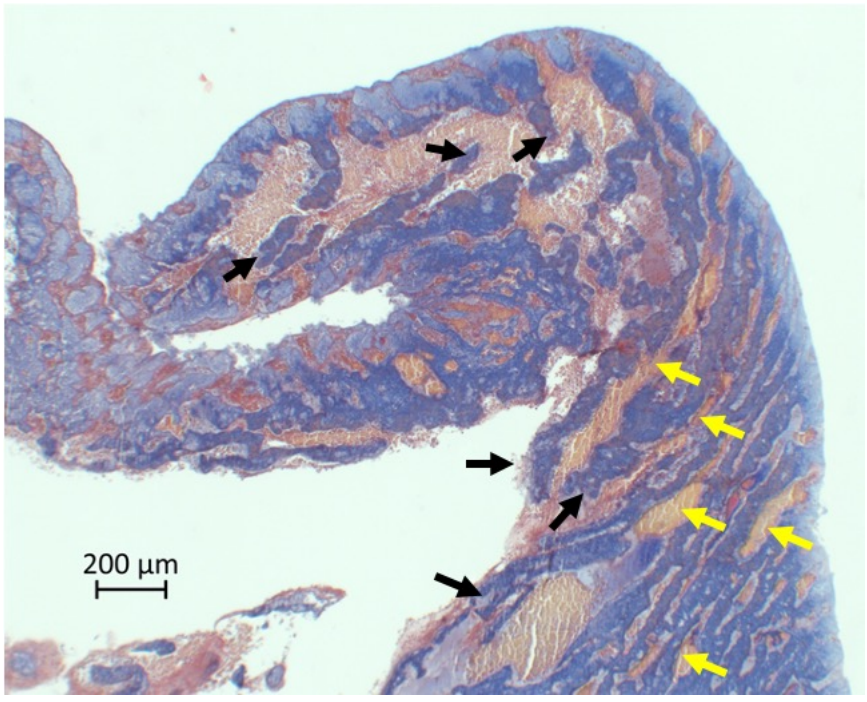

Figure 3-47. Carstairs staining of the SIPA clot in the longitudinal direction (L2, 5x magnification). Arrows indicate mountains (black) and valleys (yellow).

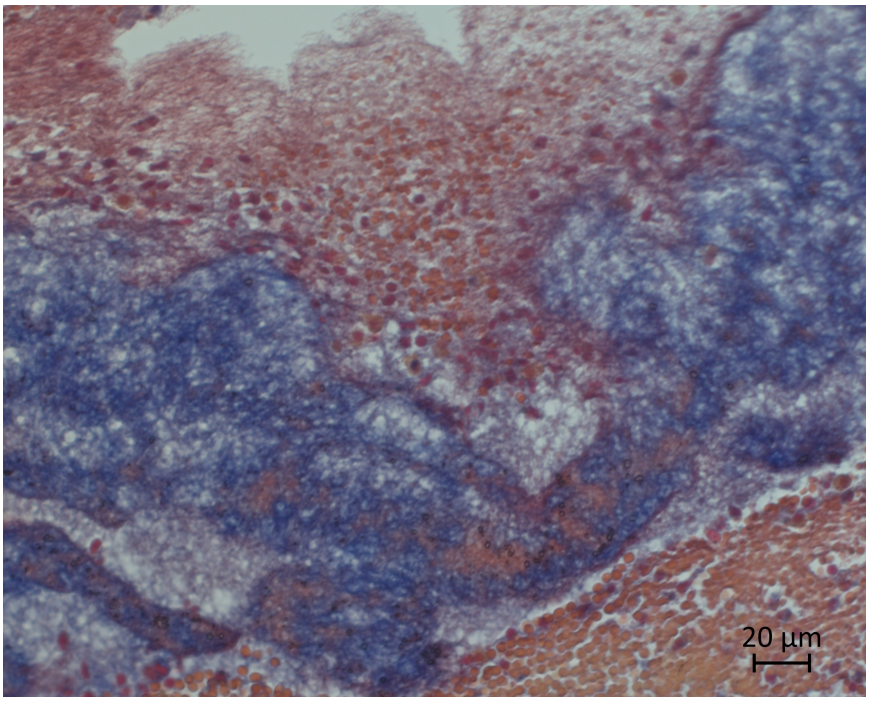

Figure 3-48. Carstairs staining of the SIPA clot in the longitudinal direction (L2, 40x magnification).

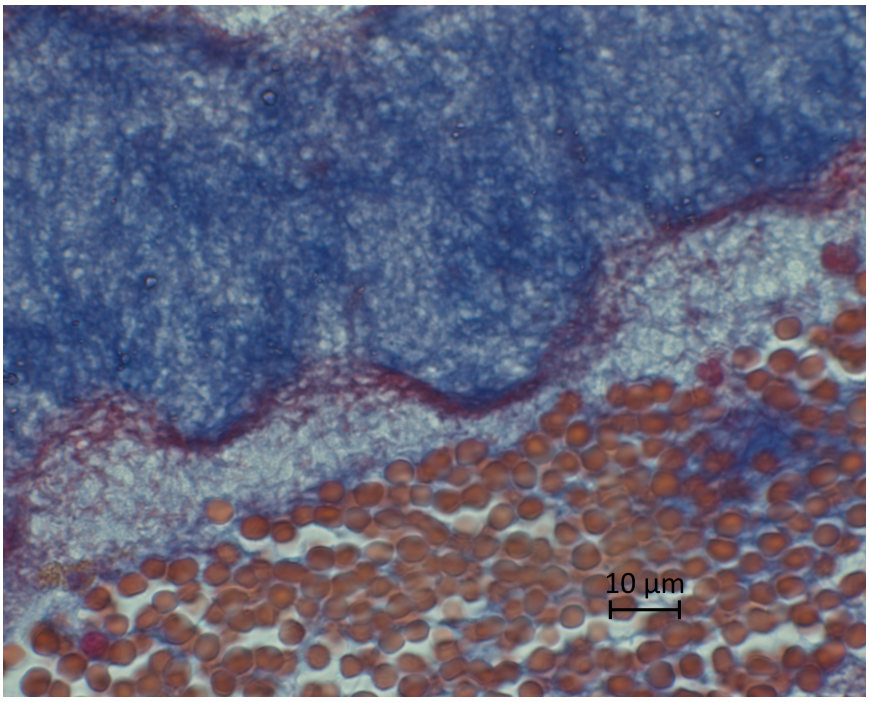

Figure 3-49. Carstairs staining of the SIPA clot in the longitudinal direction (L2, 100x magnification).

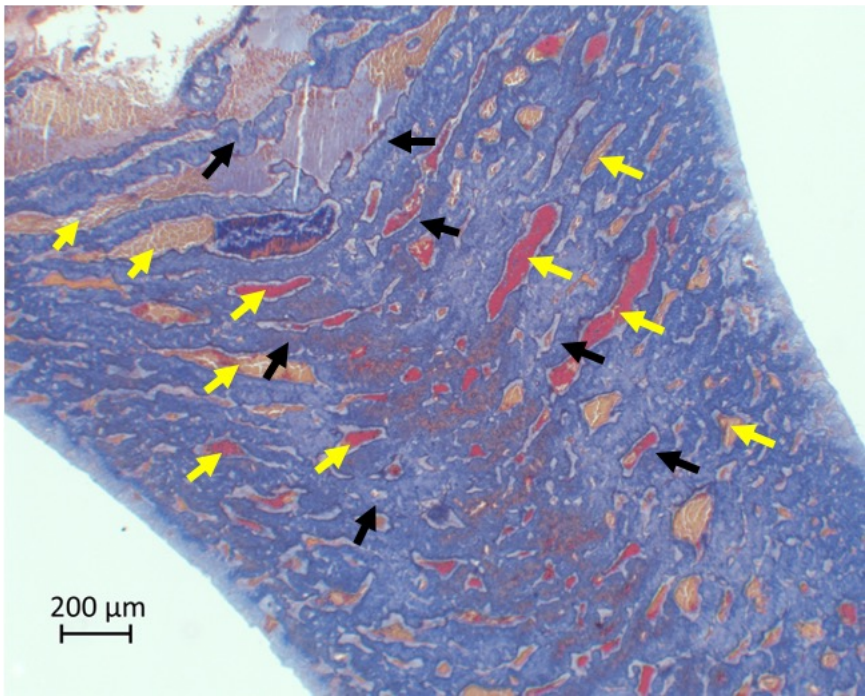

Figure 3-50. Carstairs staining of the SIPA clot in the longitudinal direction (L3, 5x magnification). Arrows indicate mountains (black) and valleys (yellow).

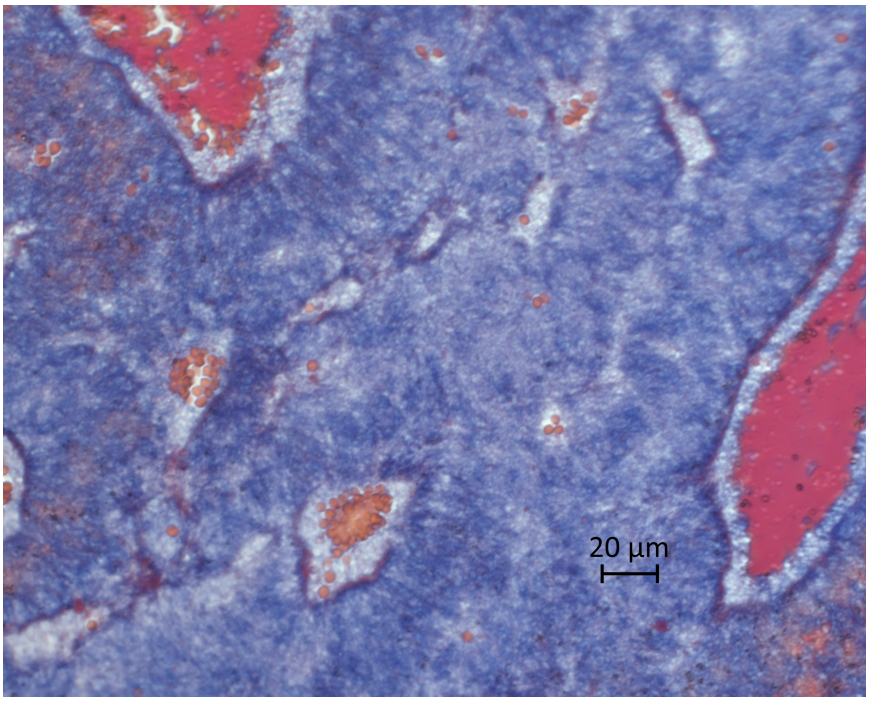

Figure 3-51. Carstairs staining of the SIPA clot in the longitudinal direction (L2, 40x magnification).

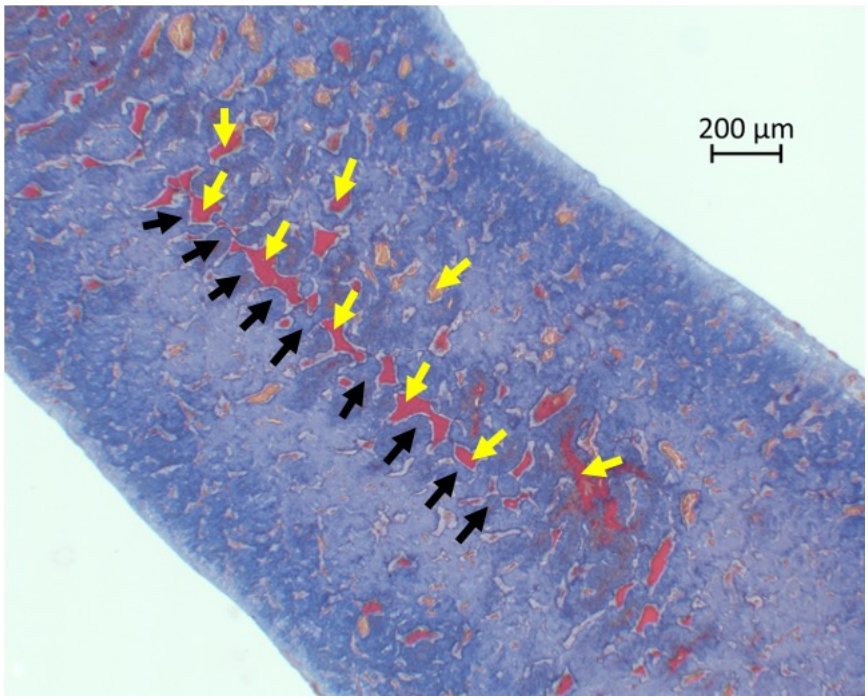

Figure 3-52. Carstairs staining of the SIPA clot in the longitudinal direction (L4, 5x magnification). Arrows indicate mountains (black) and valleys (yellow).

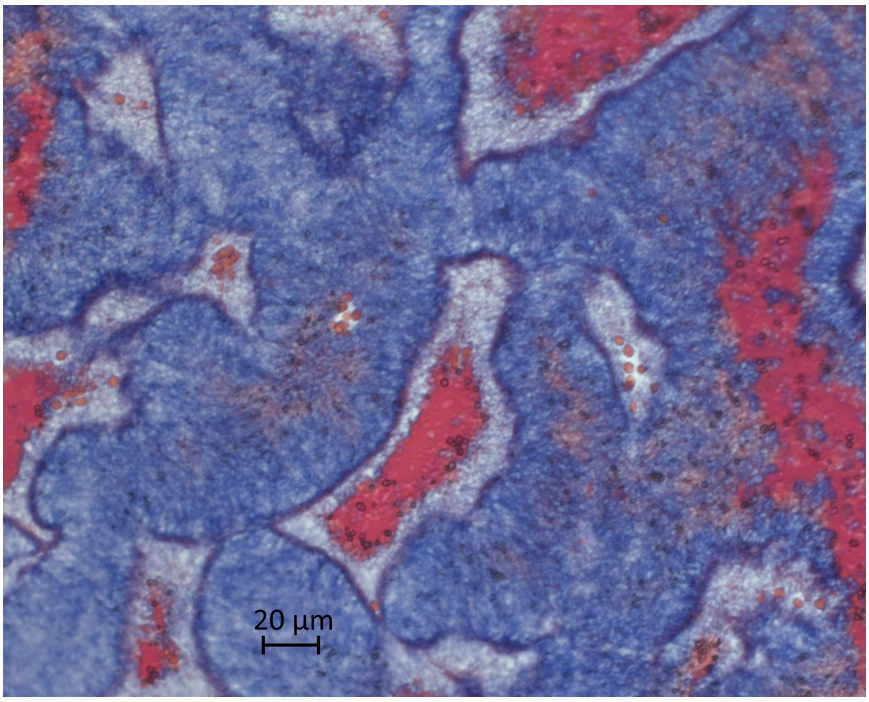

Figure 3-53. Carstairs staining of the SIPA clot in the longitudinal direction (L4, 40x magnification).

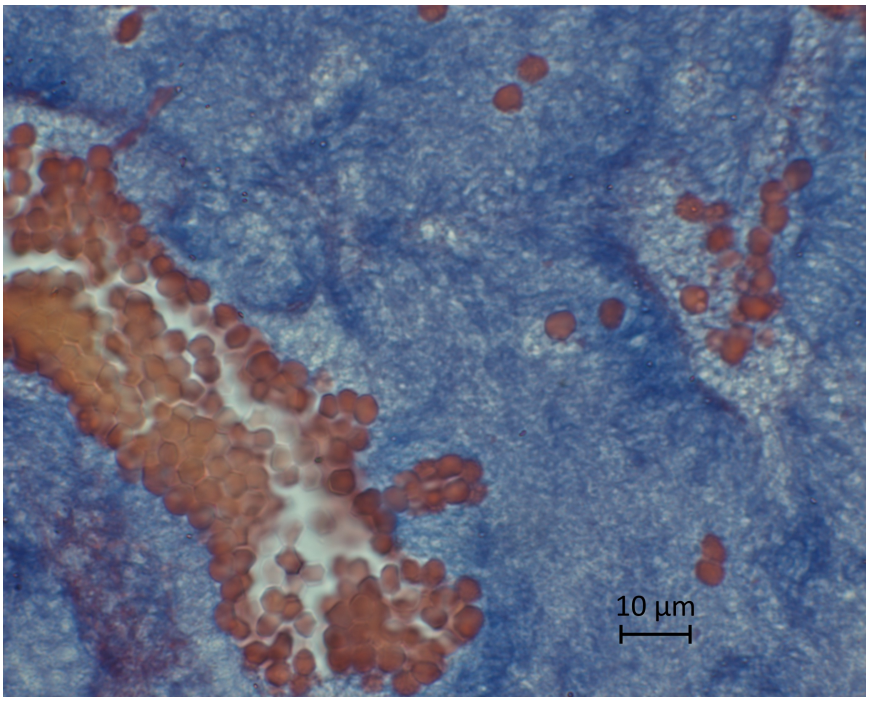

Figure 3-54. Carstairs staining of the SIPA clot in the longitudinal direction (L4, 100x magnification).

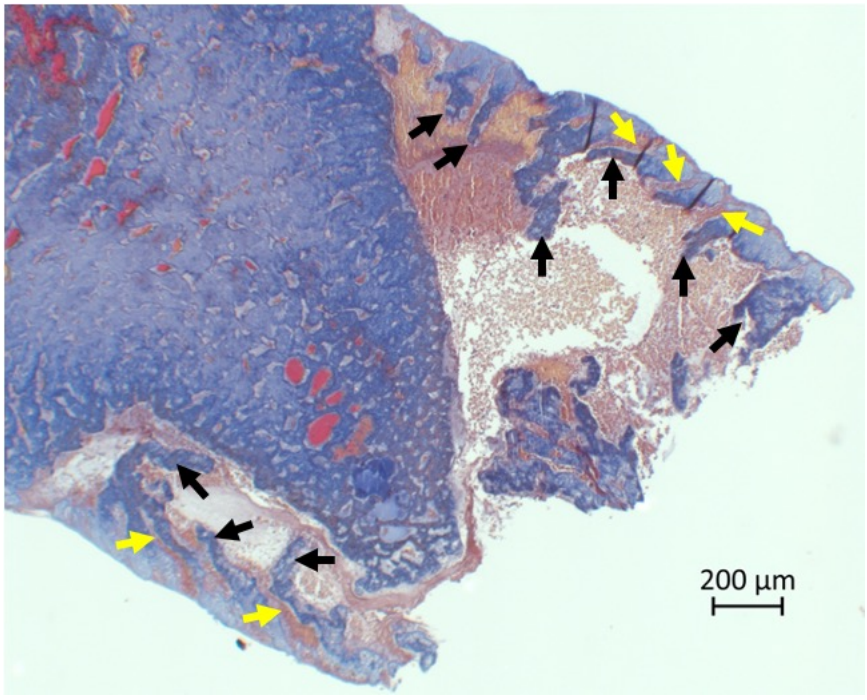

Figure 3-55. Carstairs staining of the SIPA clot in the longitudinal direction (L5, 5x magnification). Arrows indicate mountains (black) and valleys (yellow).

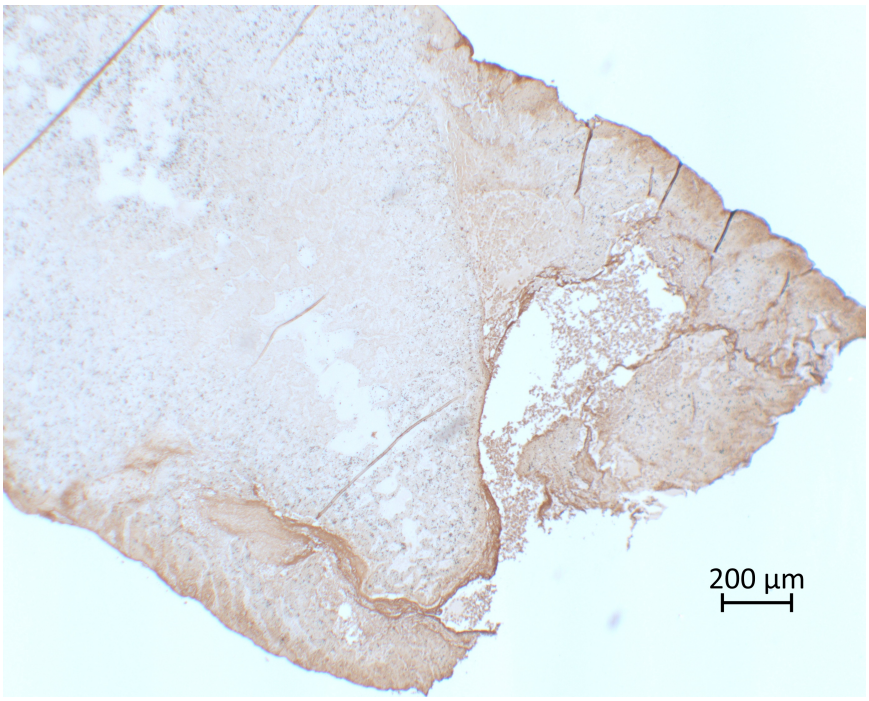

Figure 3-56. VWF staining of the SIPA clot in the longitudinal direction (L5, 5x magnification).

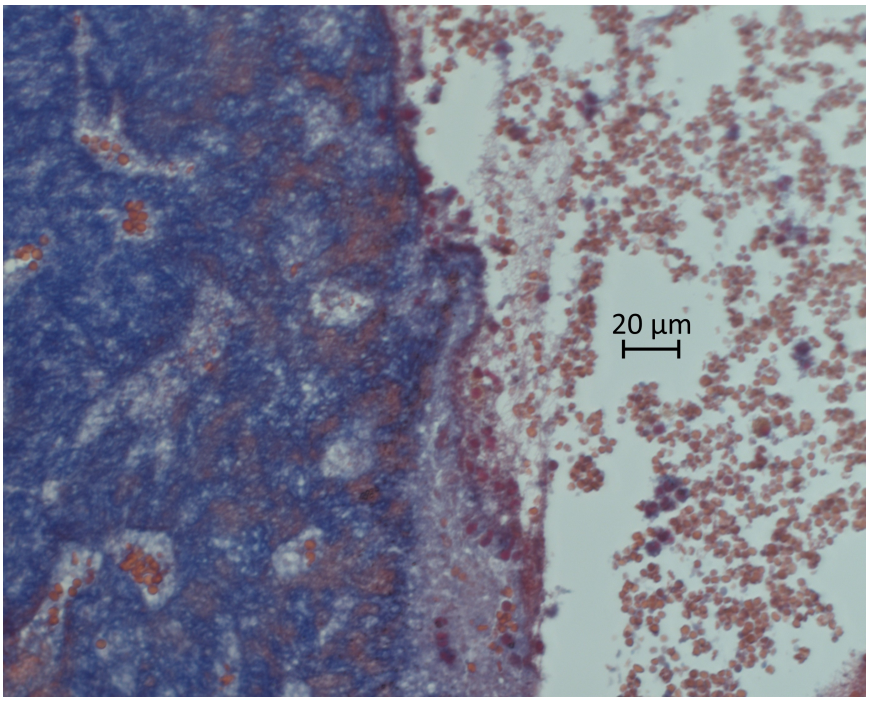

Figure 3-57. Carstairs staining of the SIPA clot in the longitudinal direction (L5, 40x magnification).

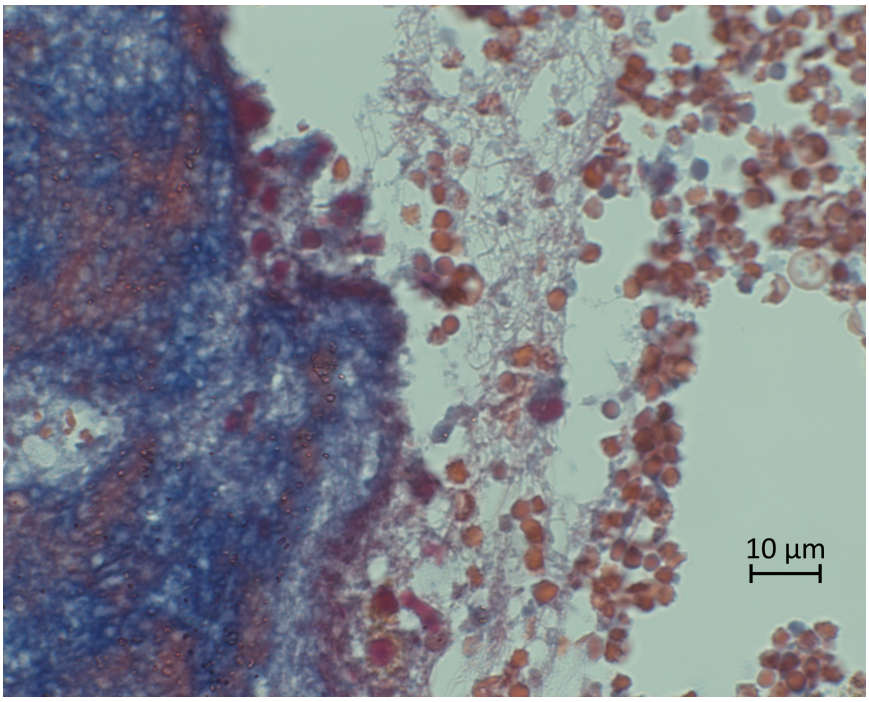

Figure 3-58. Carstairs staining of the SIPA clot in the longitudinal direction (L5, 100x magnification).

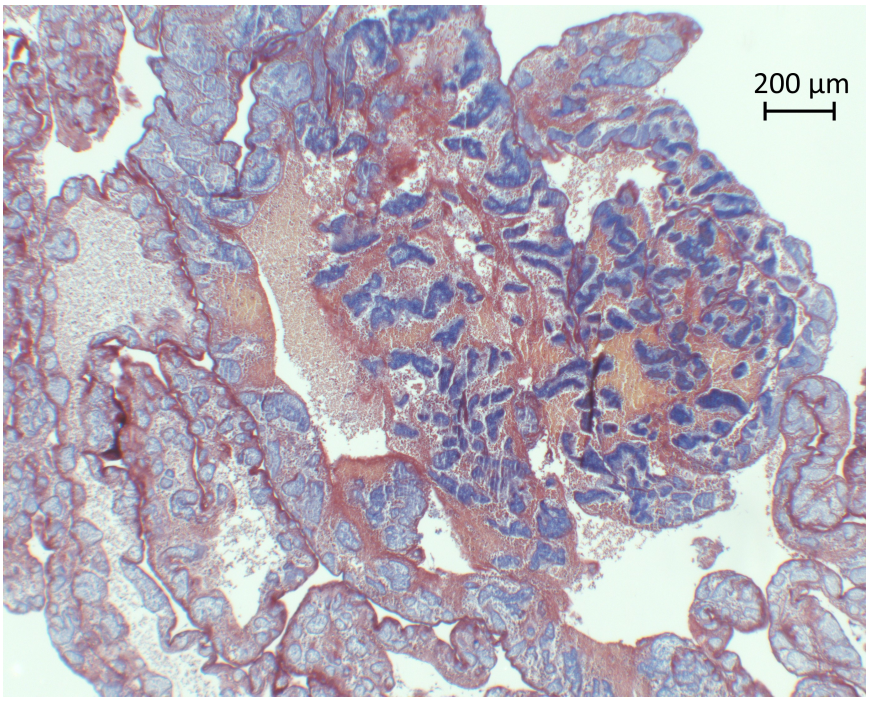

Figure 3-59. Carstairs staining of the SIPA clot in the longitudinal direction (L6, 5x magnification).

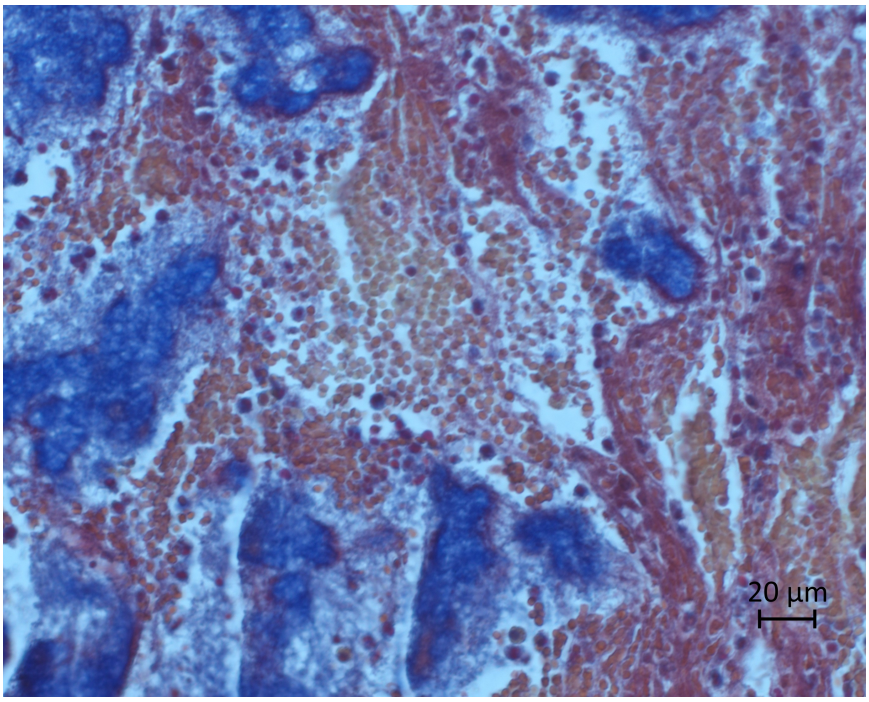

Figure 3-60. Carstairs staining of the SIPA clot in the longitudinal direction (L6, 40x magnification).

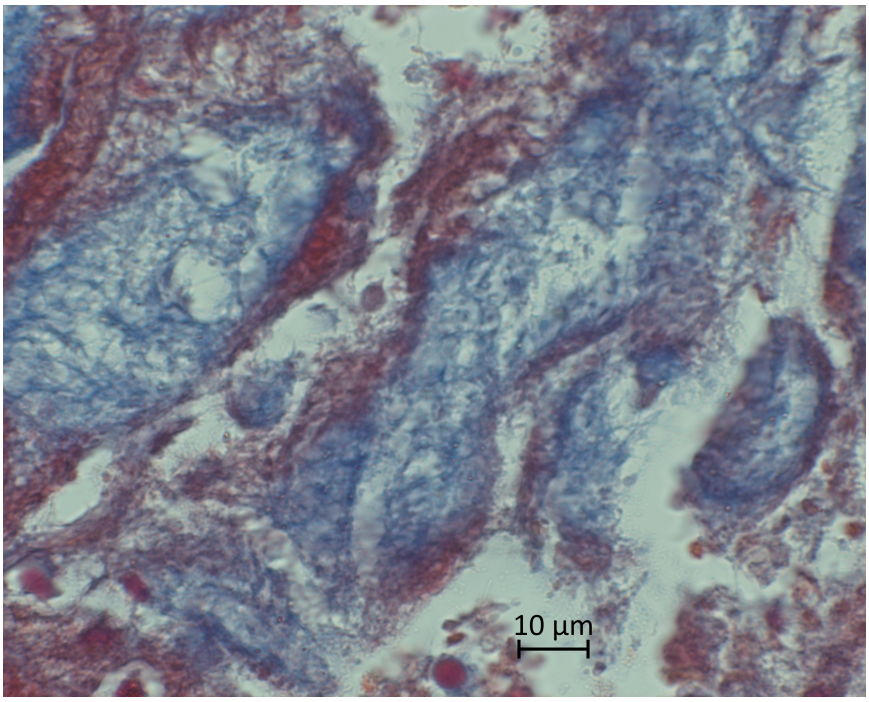

Figure 3-61. Carstairs staining of the SIPA clot in the longitudinal direction (L6, 100x magnification).

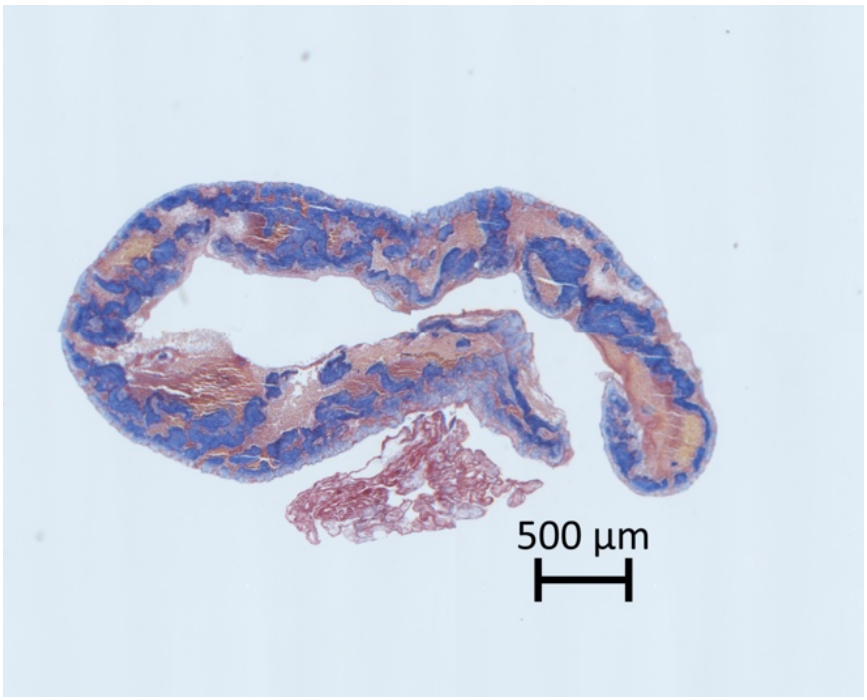

Figure 3-62. Carstairs staining of the SIPA clot in the transverse direction (T1, 5x magnification).

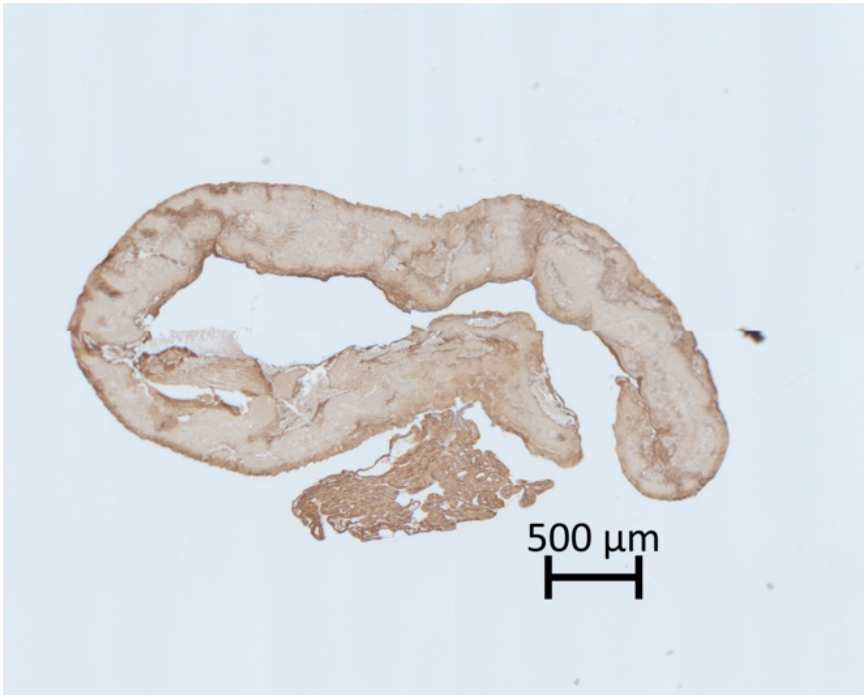

Figure 3-63. VWF staining of the SIPA clot in the transverse direction (T1, 5x magnification).

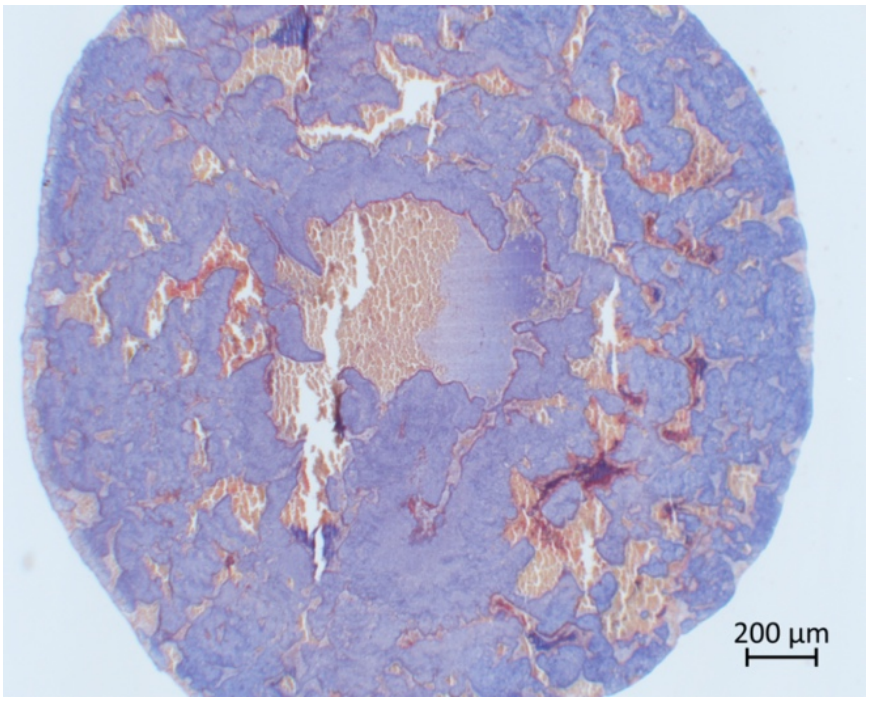

Figure 3-64. Carstairs staining of the SIPA clot in the transverse direction (T2, 5x magnification).

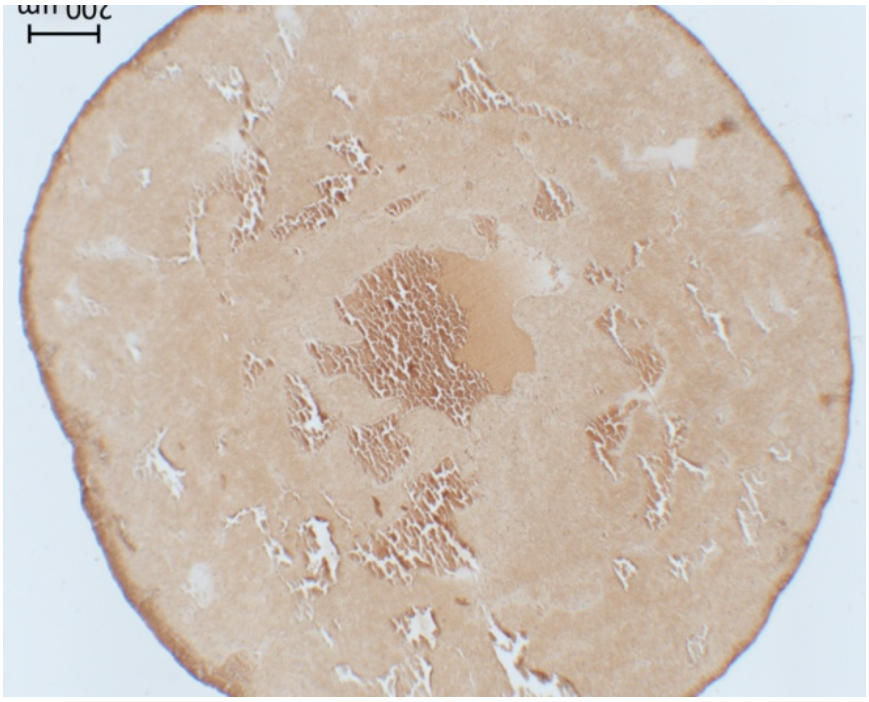

Figure 3-65. VWF staining of the SIPA clot in the transverse direction (T2, 5x magnification).

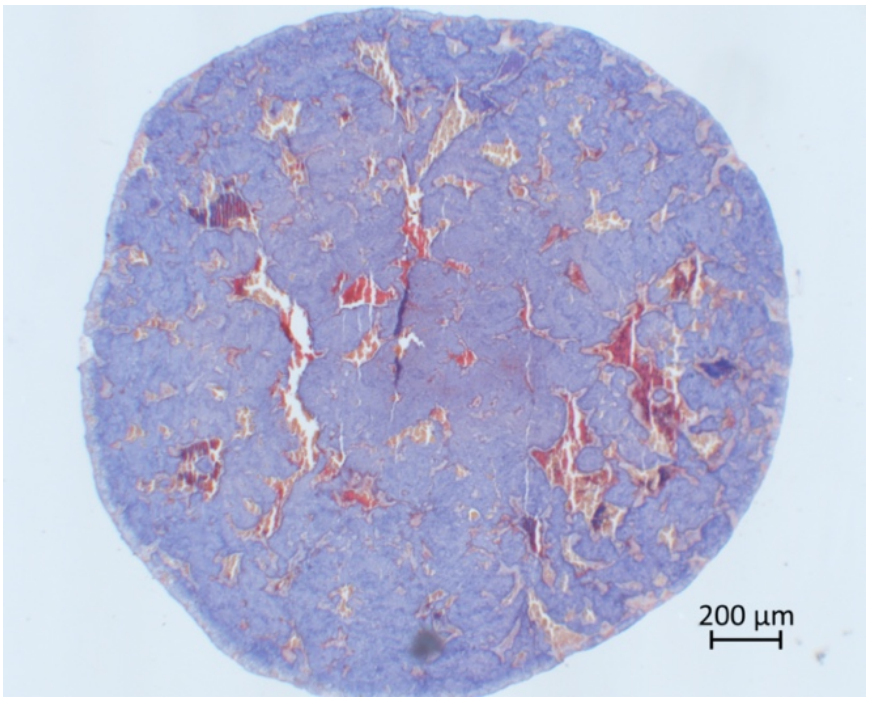

Figure 3-66. Carstairs staining of the SIPA clot in the transverse direction (T3, 5x magnification).

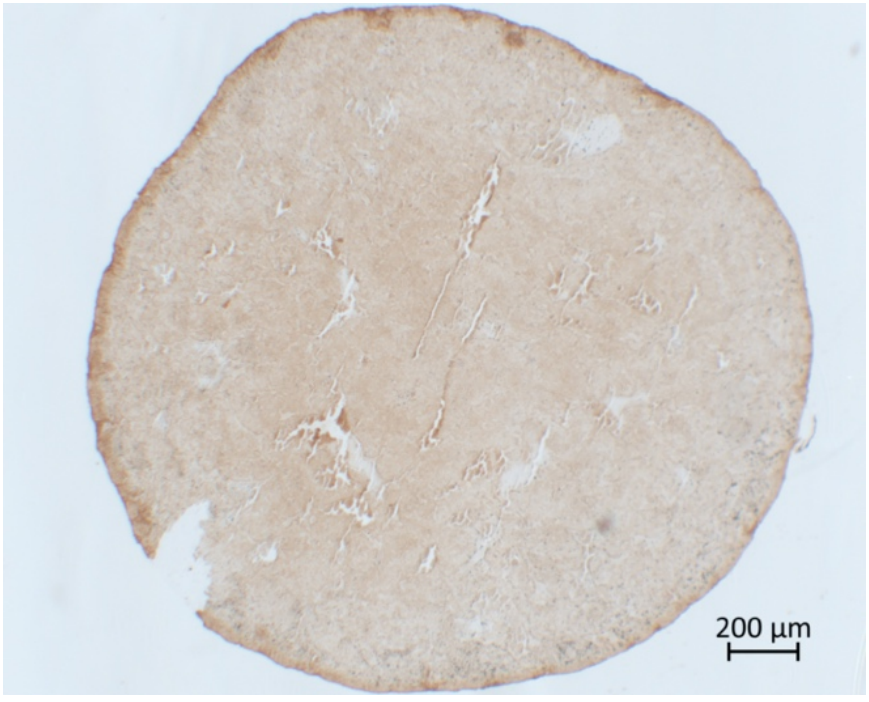

Figure 3-67. VWF staining of the SIPA clot in the transverse direction (T3, 5x magnification).

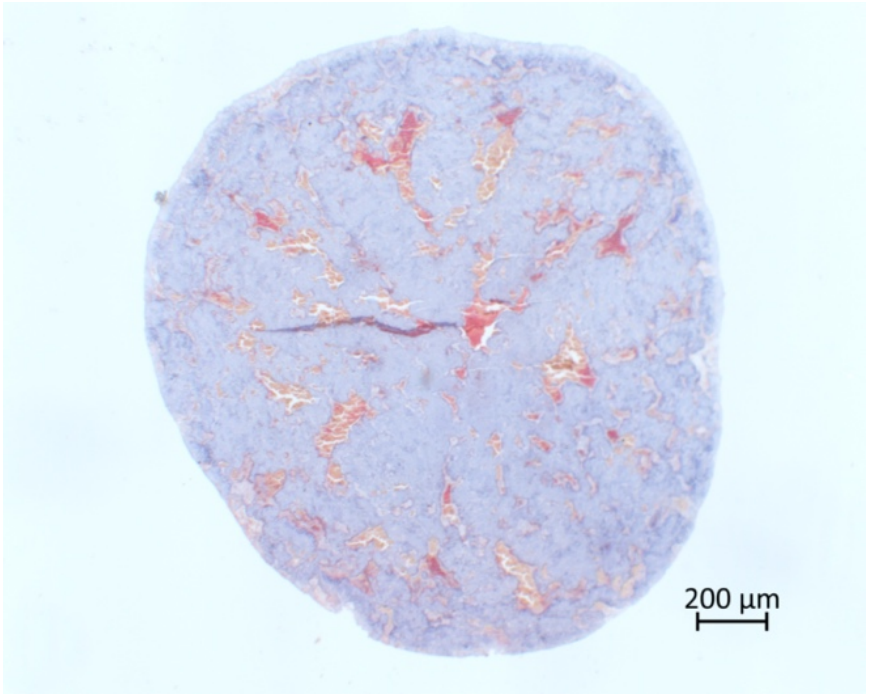

Figure 3-68. Carstairs staining of the SIPA clot in the transverse direction (T4, 5x magnification).

Figure 3-69. VWF staining of the SIPA clot in the transverse direction (T4, 5x magnification).

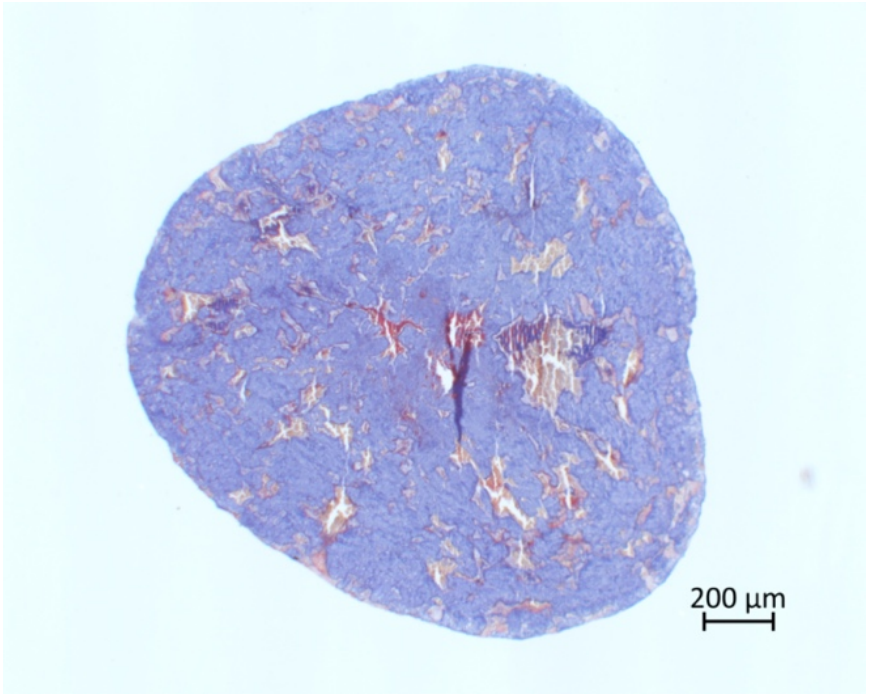

Figure 3-70. Carstairs staining of the SIPA clot in the transverse direction (T5, 5x magnification).

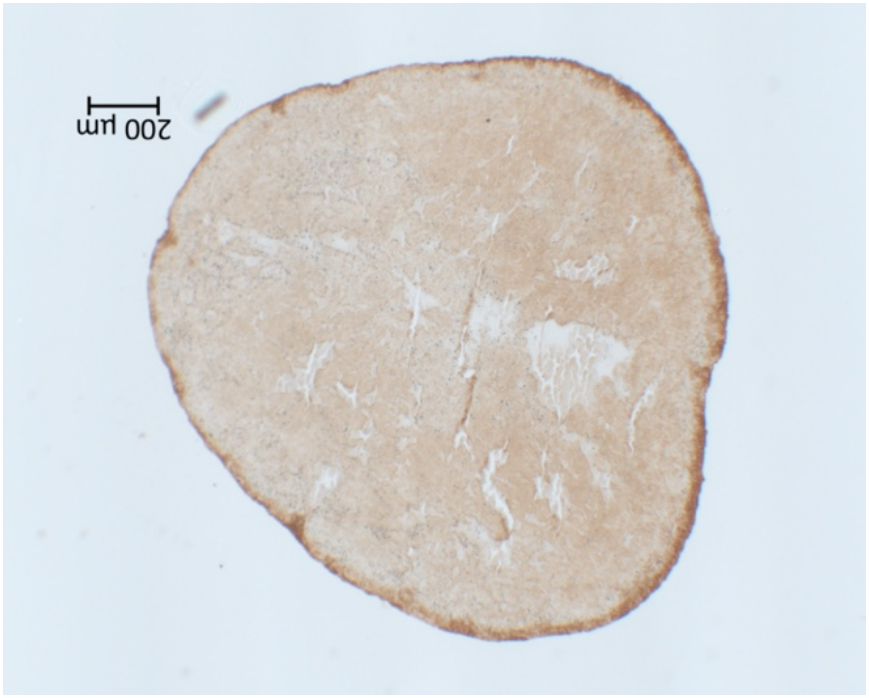

Figure 3-71. VWF of the SIPA clot in the transverse direction (T5, 5x magnification).

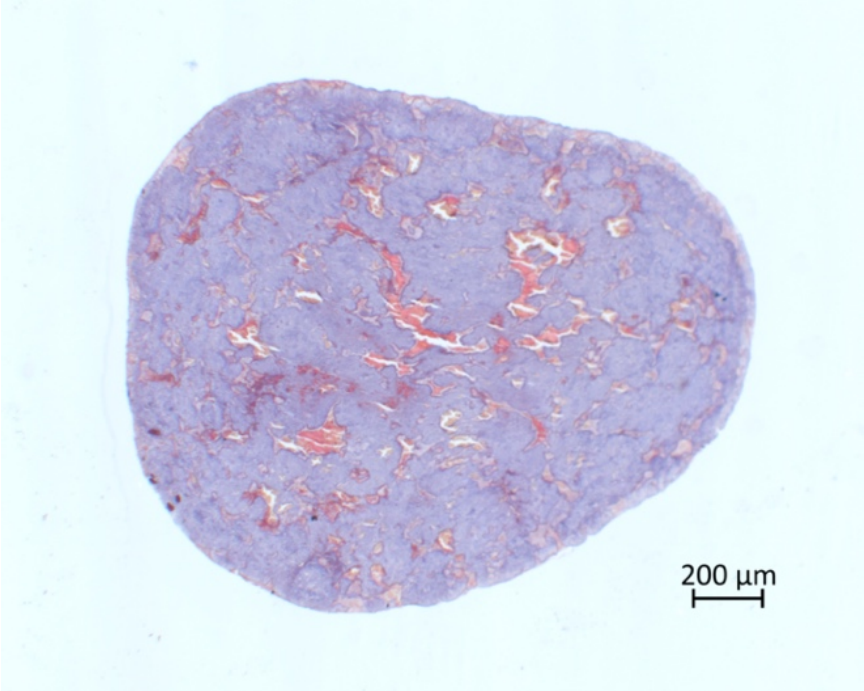

Figure 3-72. Carstairs staining of the SIPA clot in the transverse direction (T6, 5x magnification).

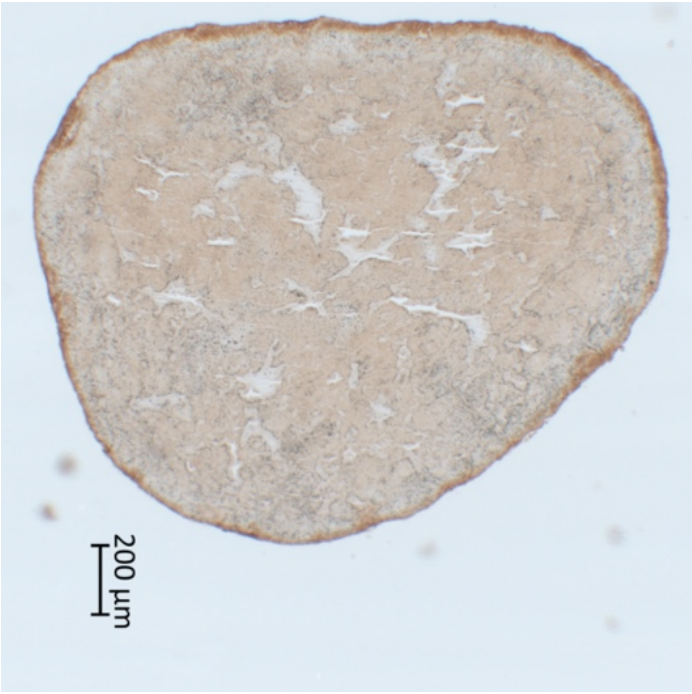

Figure 3-73. VWF of the SIPA clot in the transverse direction (T6, 5x magnification).

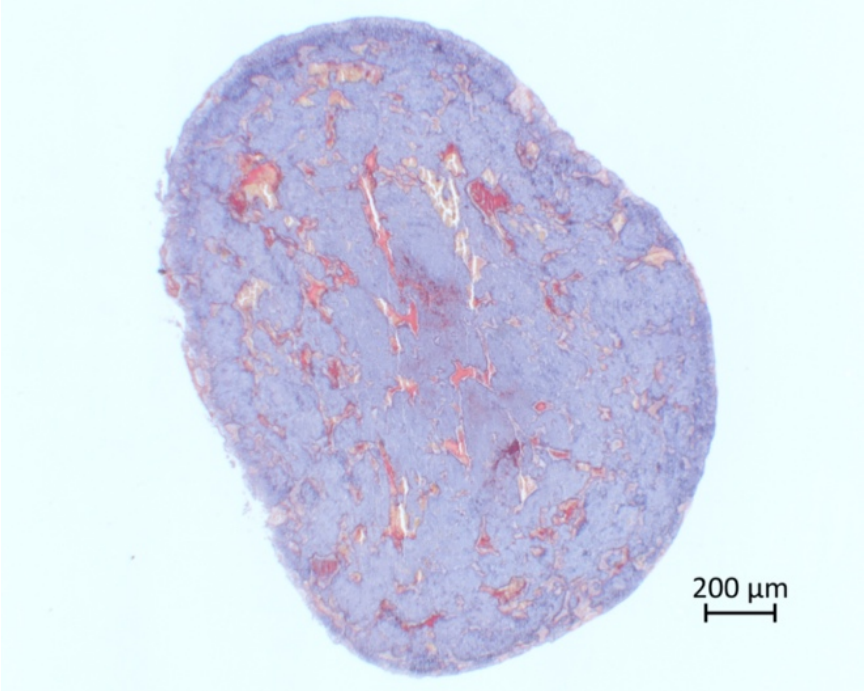

Figure 3-74. Carstairs staining of the SIPA clot in the transverse direction (T7, 5x magnification).

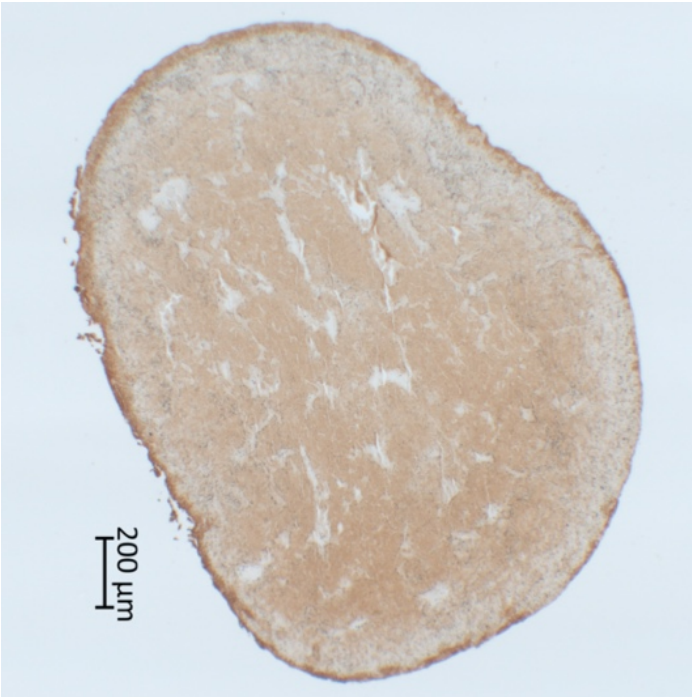

Figure 3-75. VWF staining of the SIPA clot in the transverse direction (T7, 5x magnification).

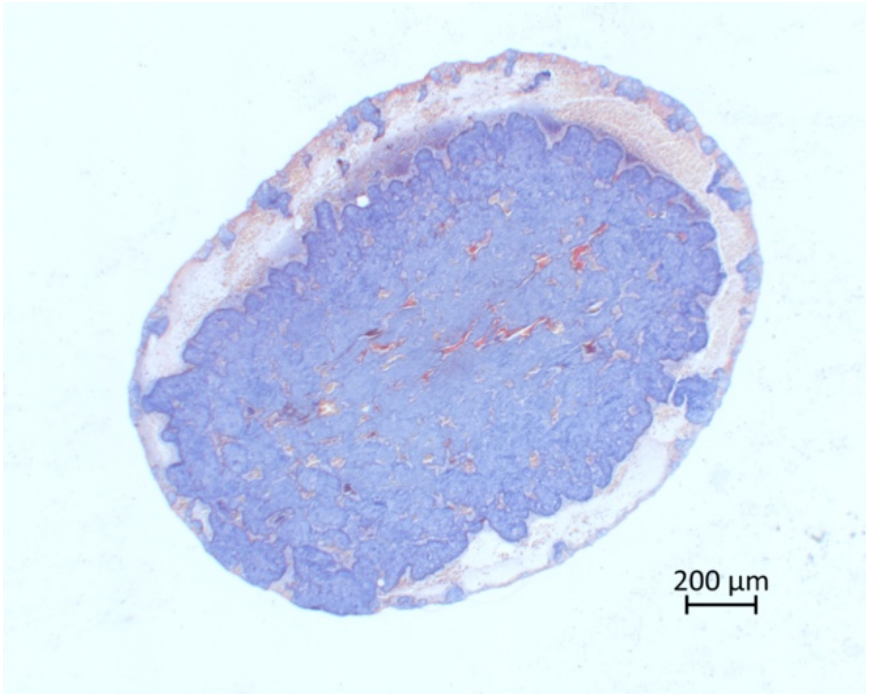

Figure 3-76. Carstairs staining of the SIPA clot in the transverse direction (T8, 5x magnification).

Figure 3-77. VWF staining of the SIPA clot in the transverse direction (T8, 5x magnification).

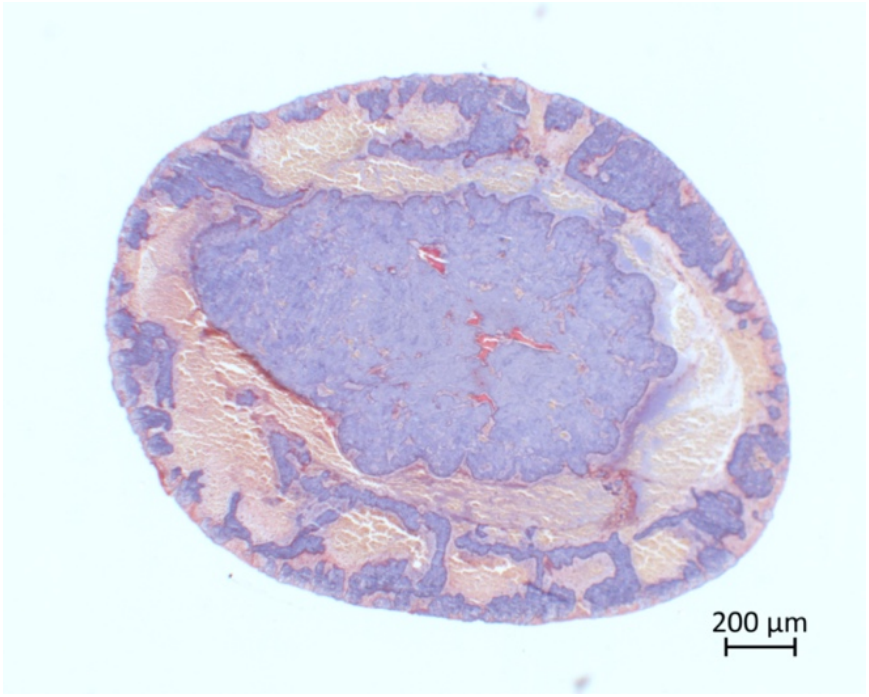

Figure 3-78. Carstairs staining of the SIPA clot in the transverse direction (T9, 5x magnification).

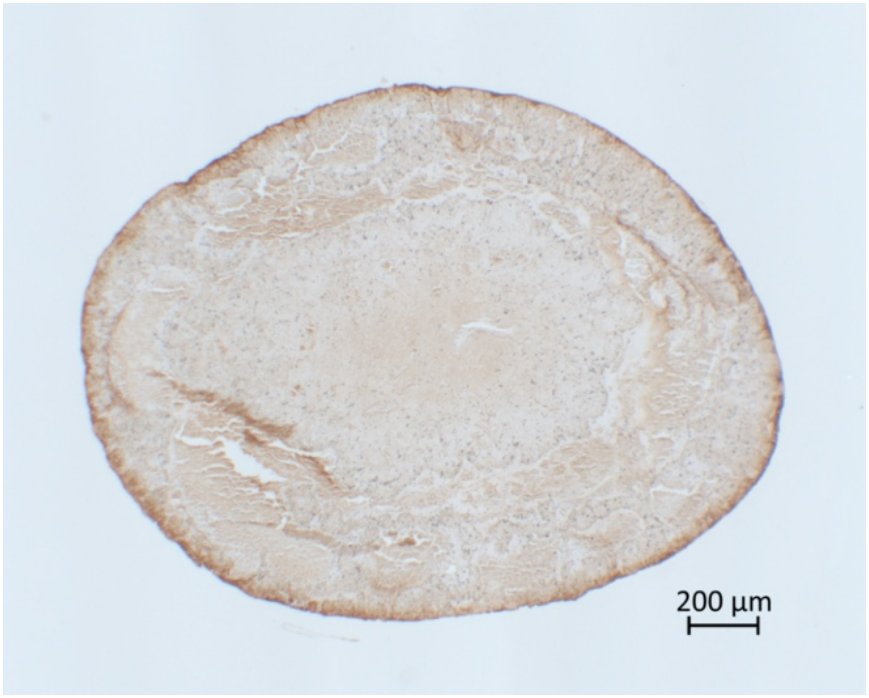

Figure 3-79. VWF staining of the SIPA clot in the transverse direction (T9, 5x magnification).

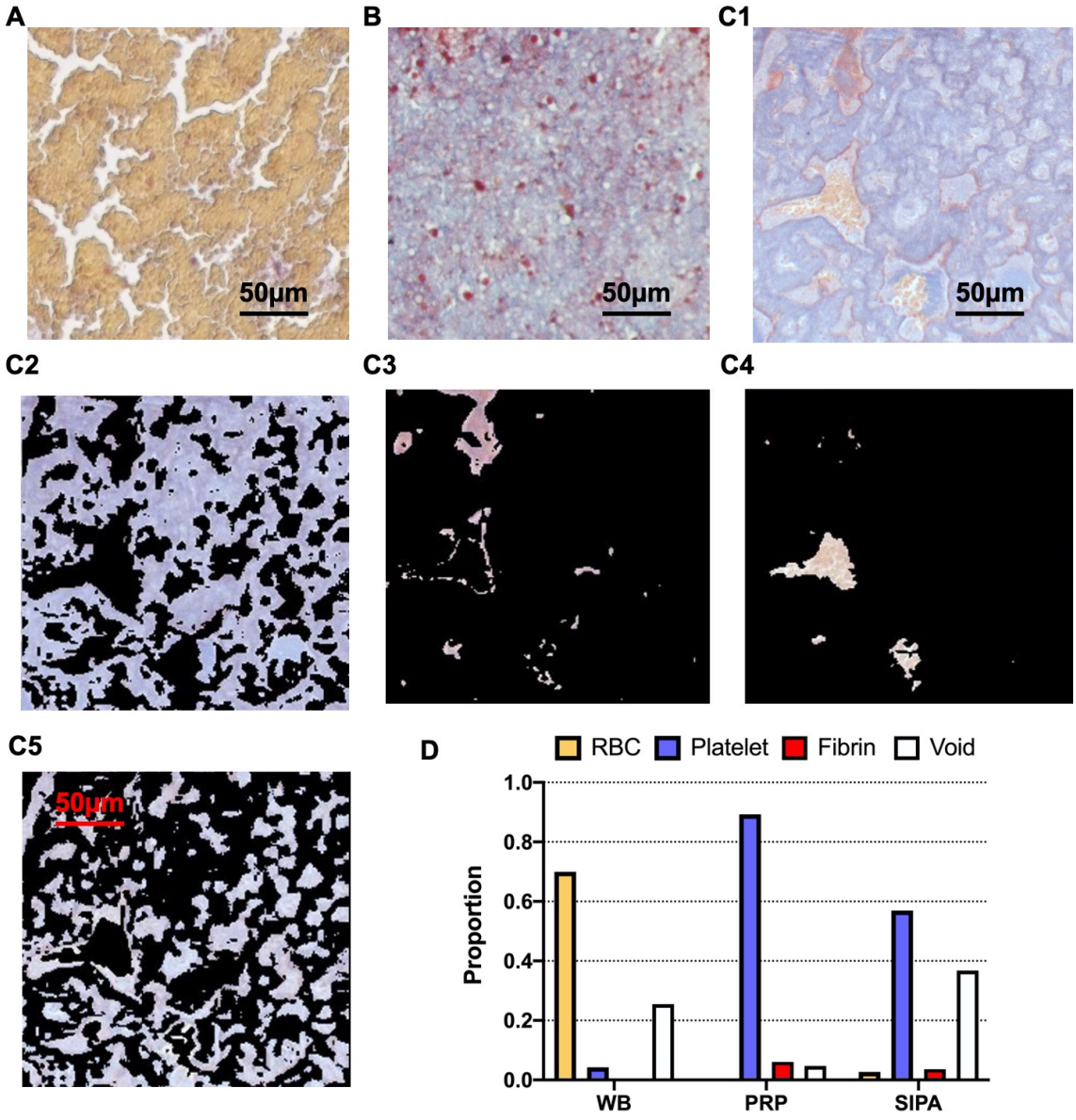

Figure 3-80. Histological analysis of (A) WB and (B) PRP coagulation clots, and (C1) a SIPA clot. Color segmentation of the SIPA clot displayed (C2) platelets, (C3) fibrins, (C4) RBCs, and (C5) void space. (D) Composition of each clot.

3.3.7 A SIPA clot is rich in VWF, especially near the wall

Prevalence of VWFs (brown) were found in the SIPA clot compared to PRP clot (Figure 3-81). In the longitudinal and transverse directions, the immunostaining results showed that VWFs were concentrated at the edge where the clot adjoined the wall (Figure 3-82A). In contrast, in the Carstairs staining result, the blue coloring was lighter near the wall, indicating that fewer platelets were aggregated at the lag phase when platelet adhesion occurred (Figure 3-82B). This complementary density of VWF and platelet was confirmed in Figure 3-82C, which plots normalized intensity level of VWF and platelet from wall to the lumen. Therefore, when the SIPA clot started to develop, a large amount of VWFs must have been accumulated first in order to capture the marginated platelets. The thickness of this layer density was about 20 μm, which had fewer platelets and larger amount of VWF.

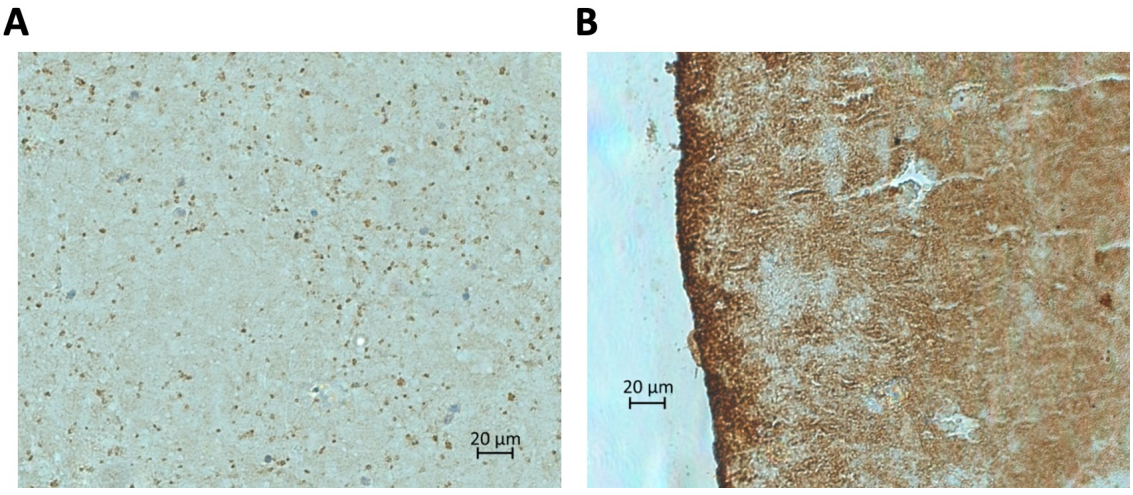

Figure 3-81. VWF staining result for (A) a PRP coagulation clot and (B) a SIPA clot (40x magnification).

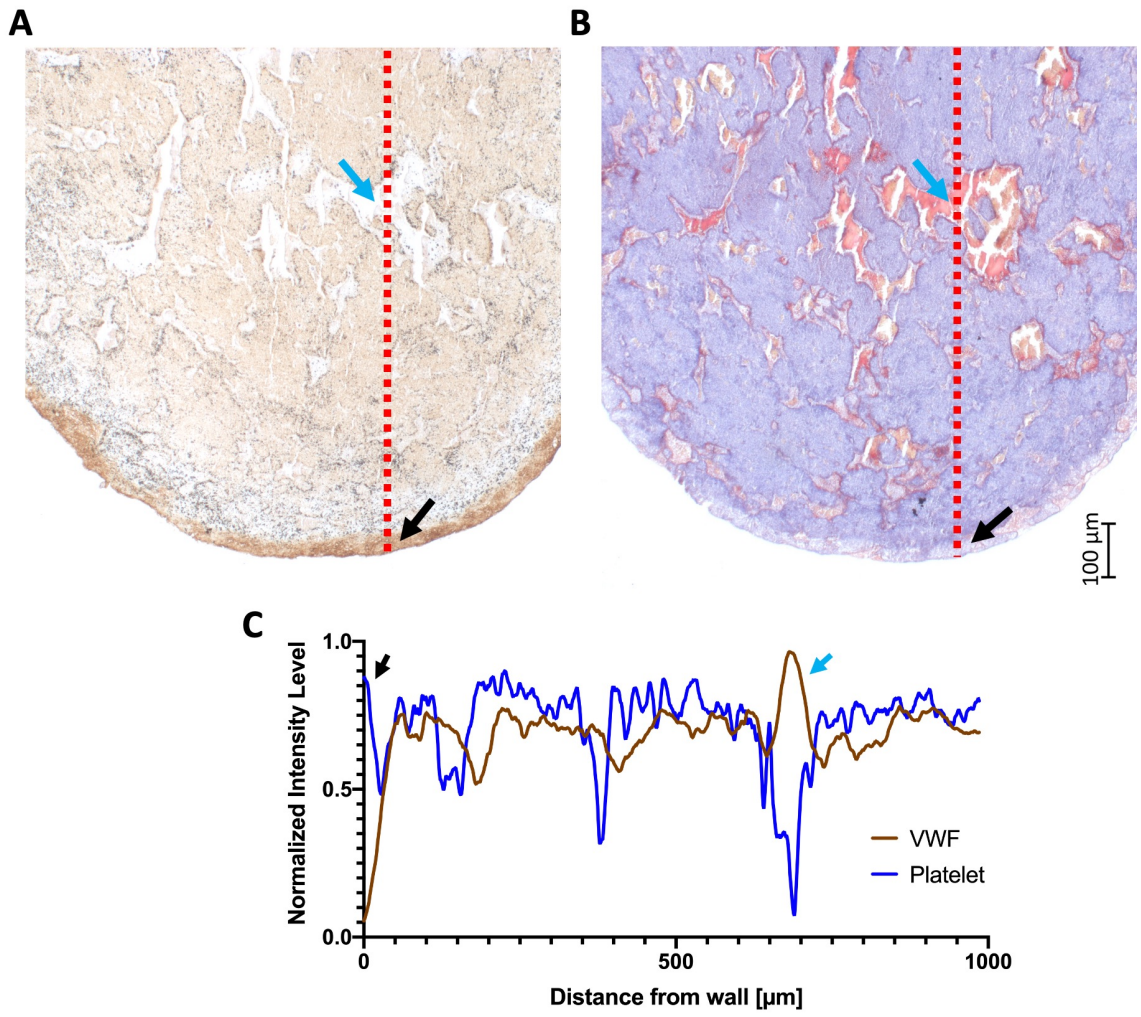

Figure 3-82. (A) VWF staining and (B) Carstairs staining of a SIPA clot in the transverse direction (Section T6, 10x magnification). (C) Normalized intensity level along the red lines in (A) and (B). Near the wall, VWF was concentrated and dark, yielding low intensity levels; whereas, Carstairs platelet was light at the wall corresponding to a high intensity level. Black arrows indicate the starting point close to the wall and blue arrows indicate a pore in the clot.

3.3.8 A SIPA clot is stiffer than a coagulation clot

Dynamic Mechanical Analysis (DMA) was conducted on 1) coagulation clots with RBCs (WB) and 2) without RBCs (PRP) as well as 3) SIPA clots (Figure 3-83). Three different displacements (0.1 mm, 0.2 mm, and 0.5 mm) and three different frequencies (0.1 Hz, 1 Hz, and 10 Hz) were applied to each clot. All clots showed elastic behavior with a small phase difference in 0.1-1 Hz range (Figure 3-83) but displayed a viscoelastic response to 10 Hz displacements. The SIPA clots demonstrated the highest compressive modulus for all conditions compared to the WB and PRP coagulation clots (Figure 3-84). On average, the SIPA clot (2.9 ± 1.9 kPa) had a 2.4 times higher compressive modulus than the WB clot (1.2 ± 0.9 kPa) and a 3.7-fold higher compressive modulus than the PRP clot (0.8 ± 0.5 kPa).

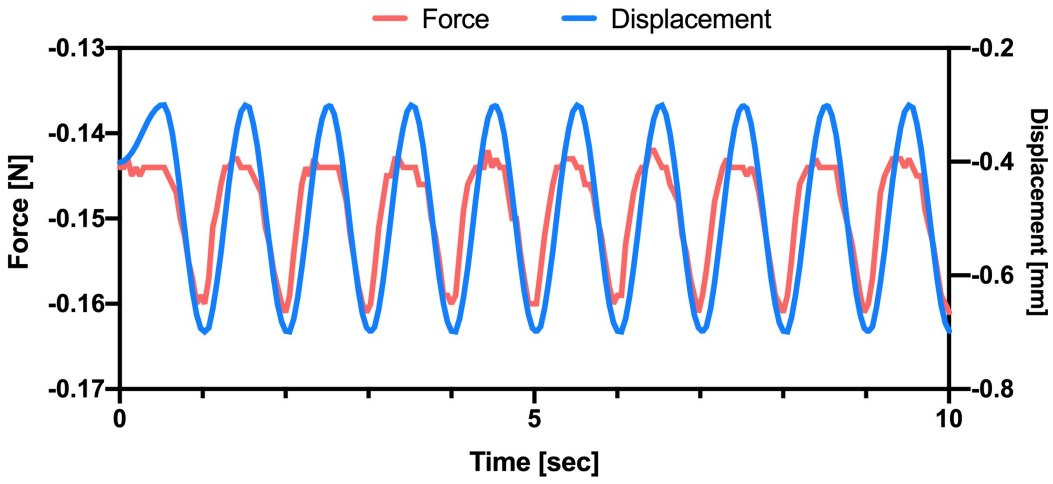

Figure 3-83. DMA result showing SIPA clot force response to a 0.2 mm displacement with 1 Hz frequency.

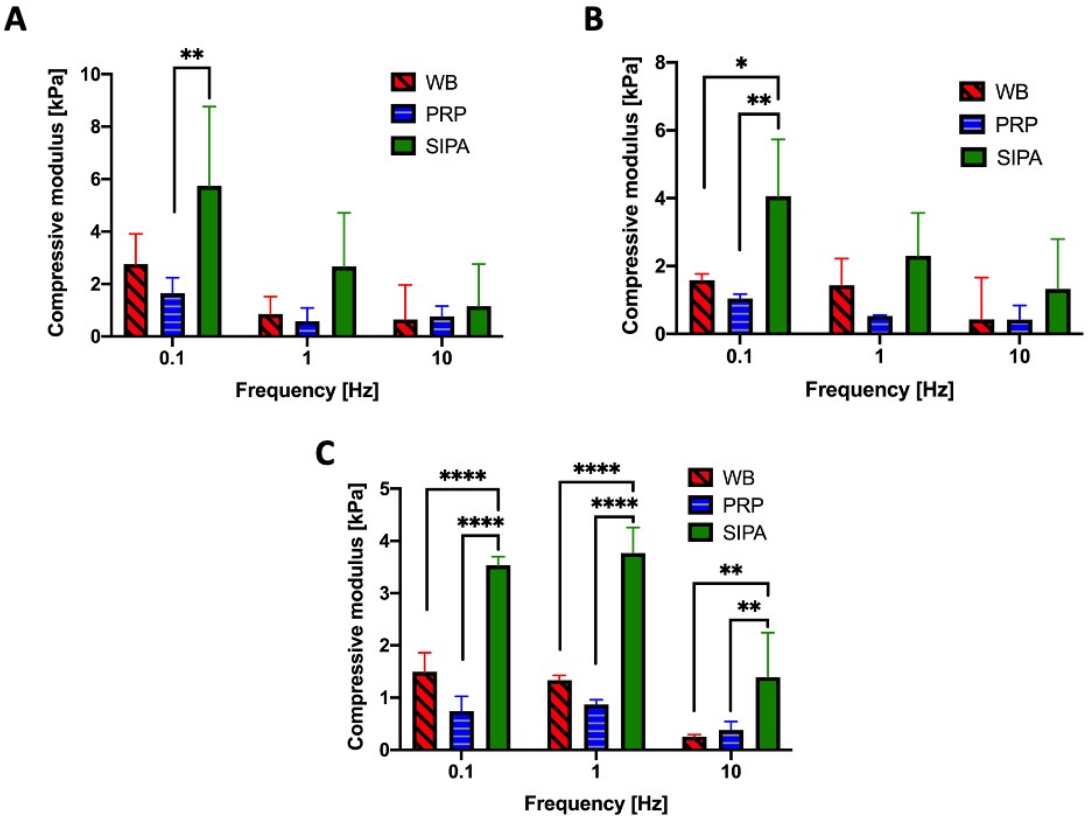

Figure 3-84. Blood clot compressive modulus measured by DMA. On average, clots had an initial height of 1.8 mm. Three different displacements were applied on the blood clots ((A): 0.1 mm. (B): 0.2 mm. (C): 0.5 mm). The SIPA clots showed a two-fold higher modulus (2.9 ± 1.9 kPa, n = 3) compared to the WB (n = 3, 1.2 ± 0.9 kPa) and PRP (0.8 ± 0.5 kPa, n = 3) clots. * $p < 0.05$; ** $p < 0.01$; *** $p < 0.001$; **** $p < 0.0001$.

3.3.9 Clot deformation and critical lengths for the arterial occlusion

An occlusive clot formed in a vessel needs to resist blood pressure to stop blood flow. CFD was performed to calculate the flow field around a clot after occlusion. The SIPA clot and coagulation clot were modeled as a porous media with different permeability (0.3 μm^2 vs.

0.0005 μm^2) and porosity (37% vs. 25%). The difference in permeability did not significantly change pressure distribution, less than 1 Pa due to pressure boundary conditions. However, SIPA clot and coagulation clot had significantly different flow rate (5 nl/min vs. 13 pl/min) and maximum blood velocity through the clot (2.2 m/s vs. 0.5 μm/s). The calculated pressure distribution (Figure 3-85) was transferred for a FE analysis to quantify clot deformation and stress distribution. The SIPA clot showed maximum deformation of 1.4 mm at the center (Figure 3-86) and stress of 5 kPa at the tip where the clot is interfacing wall (Figure 3-87). Most clot areas were having stress less than the breakage strength (4.6 kPa). The morphology after the deformation was similar to the histologic image (Figure 3-40). Meanwhile, the coagulation clot deformed more than 3 mm at the center, making the clot extremely skewed towards downstream (Figure 3-88). The coagulation clot was experiencing stress beyond its breakage strength (675 Pa); thus, it cannot block the channel and will eventually break off (Figure 3-89).

Silver, Baroldi, and Mariani (1980) found occlusive thrombosis most often occurred in 70-89 % stenosed (by diameter) coronary artery. In addition, they found an occlusive thrombus can form in a 5-mm length stenosis. Assuming a rigid clot, 175 mmHg blood pressure (Stamler et al., 1989), and using breakage strength obtained from Ch 3.3.3, a critical length that would be required for a clot to occlude a stenosed coronary artery was calculated (Table 4). A SIPA clot would have sufficient strength to occlude a 60-90% stenosed (by diameter) coronary artery with a clot length shorter than 3 mm. Meanwhile, a coagulation clot would need a length longer than 10 mm for a 60-70% stenosis or 3 mm for an 80-90 % stenosis.

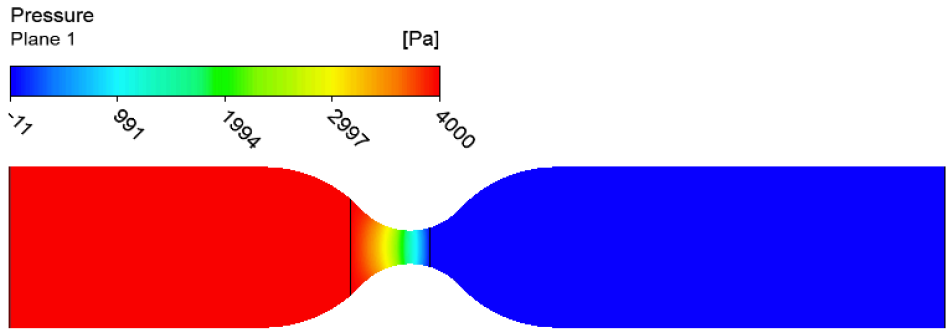

Figure 3-85. Pressure contour in a stenosed tube with a blood clot.

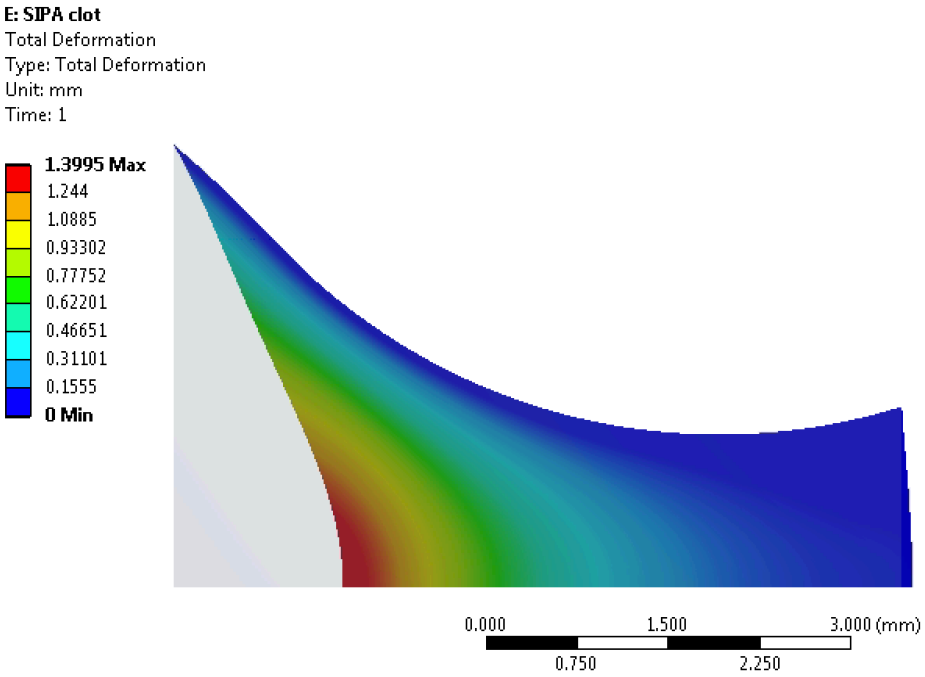

Figure 3-86. SIPA clot FE result showed maximum deformation of 1.4 mm. Undeformed state is shown as a gray contour.

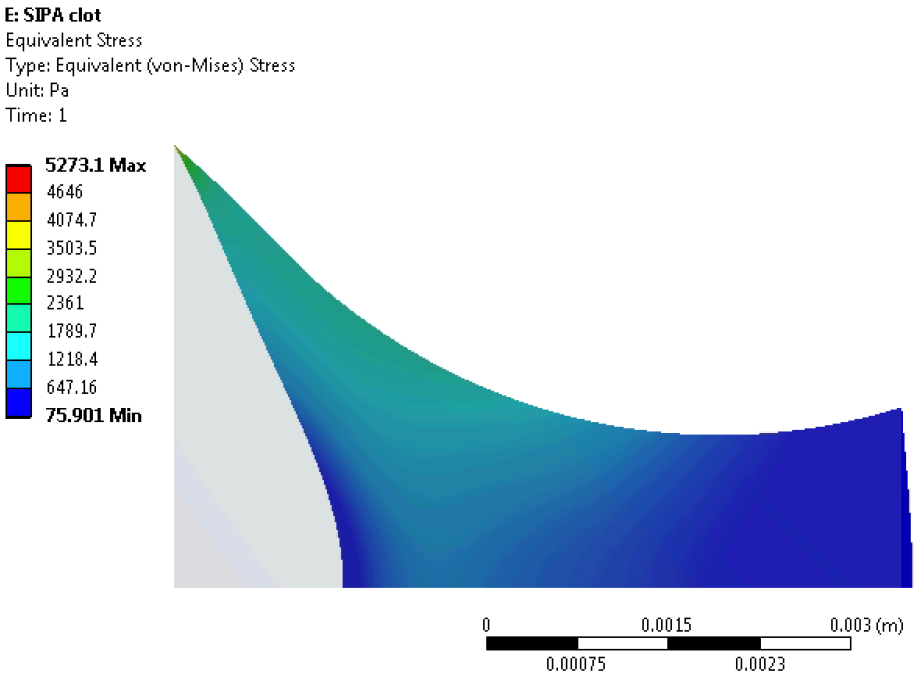

Figure 3-87. SIPA clot FE result showed stress less than its breakage strength (4.6 kPa). Undeformed state is shown as a gray contour.

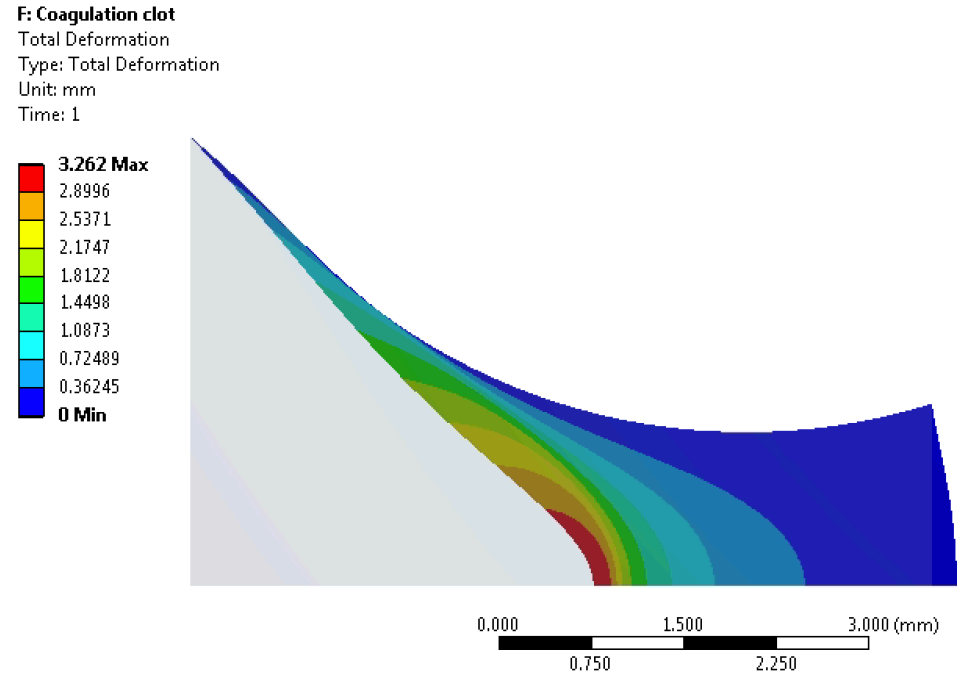

Figure 3-88. Coagulation clot FE result showed maximum deformation of 3.3 mm. Undeformed state is shown as a gray contour.

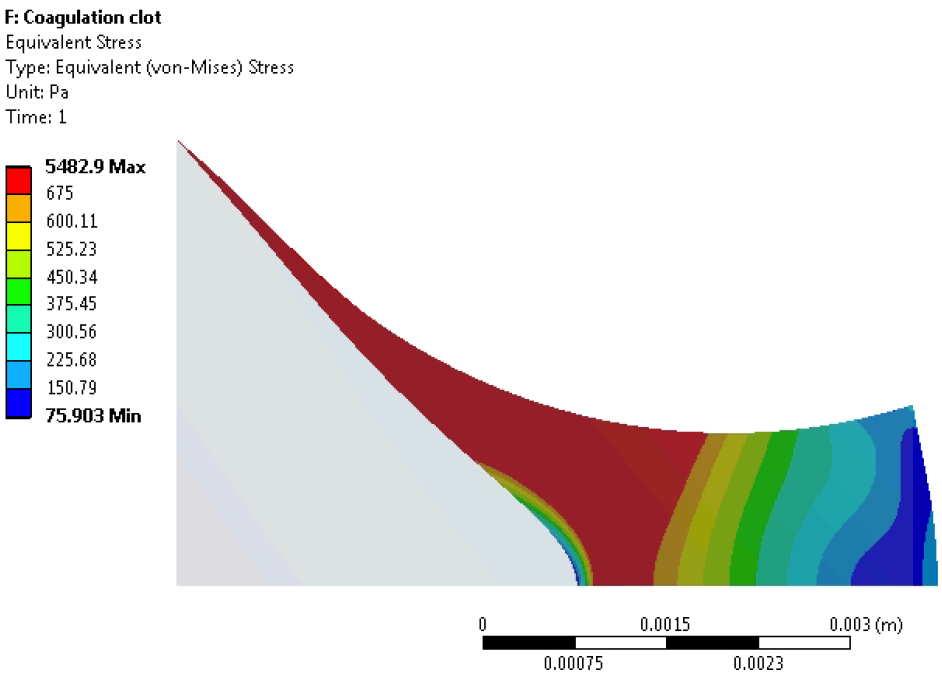

Figure 3-89. Coagulation clot FE result showed more than 39% area having a stress higher than its breakage strength (675 Pa). Undeformed state is shown as a gray contour.

Table 4. Critical clot length for coronary occlusion based on the breakage strength of the thrombus.

mm	Stenosed coronary by diameter			
	60%	70%	80%	90%
Vessel diameter	1.6	1.2	0.8	0.4
SIPA clot length	2.0	1.5	1.0	0.5
Coagulation clot length	14.8	11.1	7.4	3.7

3.4 Discussion

The SIPA clots were three orders of magnitude more permeable than the coagulation clots (0.3 μm^2 vs. 0.0005 μm^2). Despite high in platelet density (57%), the SIPA clot's permeability is two orders of magnitude higher permeability compared to 31% platelet-rich coagulation clot (0.0061 μm^2) by Wufsus et al. (2013). The high permeability may help the SIPA clot to relieve flow pressure and continue to grow. The permeability of the clot is strongly related to the thrombolytic drug delivery to the clot (Diamond, 1999). A previous study has used the value of a coagulation clot's permeability to estimate the thrombolysis time (Piebalgs et al., 2018); however, the change in permeability for a SIPA clot will likely result in significantly different thrombolysis time. Based on the permeability value in Figure 3-10, porosity was estimated using multi-channel modelling in this study. The porosity from the histology images (37%) was in the range of the theoretically calculated maximum porosity value (60%), implying that the SIPA clot's porous structure is equivalent to 1,000 pores with an approximate diameter of 10 μm. These values are in good agreement with what Arrarte Terreros et al. (2020) found in their clinical study. They calculated permeability of occlusive thrombi in acute ischemic stroke patients by measuring flow rate and assuming a range of pressure gradient from 30 to 100 mmHg. They arrived at conclusions that the thrombus permeability ranges from 19.2 μm^2 to 64 μm^2, the number of channels in the thrombus ranges from 449 to 1,497, and the channel radius ranges from 12 μm to 22 μm. Thus, the occlusive thrombi found in acute ischemic stroke patients must be SIPA clot, not coagulation clot.

The present findings indicate that a SIPA clot has 7 times higher breakage strength (4.6 kPa vs. 0.6 kPa) and 2.5 times higher stiffness (3.2 kPa vs. 1.2 kPa) than a WB

coagulation clot. Compared to Riha et al. (1999), the measured breakage strength (0.3 kPa vs. 0.6 kPa) and stiffness (0.4 kPa vs. 1.2 kPa) of coagulation clots were higher in our study. They tested coagulation clots immediately after mixing calcium chloride, thus fibrin polymerization could have been immature to provide a higher strength; whereas, our study allowed 30 min to 1 hr for the coagulation clot to be polymerized.

The SIPA clot may have more strength than coagulation clots from the components or the architecture. The protein strands of VWF and fibrin are likely similar in strength, as well as the cell membranes of platelets and erythrocytes, so the components are similar. CFD models of SIPA aggregation indicate that multiple strands of VWF roll up individual platelets into agglomerates (Z. Liu, 2020). Coagulation clots likely form by single fibrin strands connecting RBC during static conditions. Thus, the seven-fold increase in strength may stem from the architecture of greater numbers of VWF tethers forming the SIPA aggregate. Alternatively, the interface between components rather than the component itself may break off. Lam et al. (2011) did a single platelet measurement by using atomic force microscopy cantilever coated with fibrinogen, and found a rupture occurred at the interface when stress reached 5 kPa. Meanwhile, Wellings and Ku (2012) suggested that a VWF net can capture a platelet under high shear via numerous Gp1b-A1 bonds that have strength of $\sim <$ 100 pN. A concave VWF net can create 11,280 bonds, which can be converted to a strength of 100 kPa. Moreover, more GPIIb/IIIa bonds can form and give additional strength between platelet-VWF interface after a platelet activation. Thus, the strength may derive from the increased number of bonds per platelet during SIPA.

With the measured stiffnesses of a SIPA clot, our FE model showed that the center of SIPA thrombus facing the flow deforms about a same magnitude (1.4 mm) compared to

histologic images (1.2 mm) and can block the large stenotic glass tube. In contrast, a coagulation clot would deform more than 3 mm and have a large area having stress that exceeds its breakage strength. Using our calculated breakage strengths of blood clots, a critical length for a clot to occlude stenosed coronary artery was estimated and compared to clinical data (Silver et al., 1980; Stamler et al., 1989). A SIPA clot would be strong enough to resist an arterial blood pressure (175 mmHg) and occlude the artery with a length of 2 mm. In contrast, a coagulation clot would be required to be longer than 10 mm clot length for ~70% stenosis in diameter and 3 mm clot length for ~90 % stenosis in diameter. Thus, it is unlikely that a coagulation clot could account for an arterial occlusion as it would need to be much longer than generally observed at autopsy. However, a coagulation clot may form after the SIPA clot occludes an artery, proximal and distal to the SIPA clot. Thus, a pathological post-mortem specimen may be mixture of SIPA clot and coagulation clot, especially if there was time delay between the occlusion and a clot retrieval. This may explain why people have been reported finding fibrin clots in coronary arteries (Uchida et al., 2011) or carotid arteries (Marder et al., 2006), after late harvest making hard to distinguish the real culprit of an occlusion.

SIPA clots were generated in a closed *in vitro* flow loop to investigate the SIPA clot structure. The size of the generated SIPA clot was physiologically relevant (2 mm in diameter and 5 mm in length) and had a trumpet-like shape with the mouth opened against the blood flow. SEM images showed that the platelets were tightly packed in the clot with a density of 0.1 platelets/μm^2, indicating that the 1.23 billion platelets were aggregated in the SIPA clot. Even more platelets are expected to be present in the clot because the density was calculated by counting spheres (i.e., unactivated platelets) from images. The

histological images showed consistent results in which the clot was VWF-platelet-rich, and RBCs were trapped in the pores, which is strikingly similar to the SIPA clot formed in mice in vivo model in Ch2 (Figure 2-7D). Casa and Ku (2017) suggested a 7-step process for a SIPA clot formation. The process starts with a high wall shear rates (step 1) and VWF adsorption onto the collagen surface (step 2). In this study, the SIPA clot had a high VWF density on the wall, but sparse platelets compared to the lumen side. The plasma VWF must be important for the lag phase (step 1-2), as platelets need to be captured at the wall (step 3-4).

Casa et al. (2016) found that plasma VWF is more important than platelets in forming occlusive SIPA clots. When a sufficient amount of VWFs are accumulated, and a minimum number of platelets are captured (step 3-4) and activated, platelets can make new highly reactive surfaces by releasing granules of VWF (step 5). As discussed in CHAPTER 2, α-granules are necessary to initiate the RPA phase (step 5-7) and the subsequent vessel occlusion. The histological images show that there was a sudden transition from light blue to dark blue all the way to the lumen. This light blue layer was about 20 μm thick, which is comparable to the 10 μm thrombus thickness defined by Bark, Para, and Ku (2012) for the lag phase. Based on the growth rate of SIPA, they suggested 10 μm thrombus thickness as a transition threshold from the lag phase to the RPA phase. Between 20 μm thick layer and center of the lumen, mountain-like structures protruding from wall to the lumen were found in a half-cut SIPA clot (Figure 3-16) and Carstairs staining slice in a longitudinal direction (Figure 3-40). This structure was prominent at the upstream (L2-3), with RBCs trapped in valleys between mountains. Past studies also observed these SIPA clot structures,

which was referred as “fingers” in expanded polytetrafluoroethylene vascular graft tubing (Wootton, Markou, Hanson, & Ku, 2001) and glass capillary tube (Para & Ku, 2013).

It is interesting how these mountains (indicated in Figure 3-12, Figure 3-47, Figure 3-50, Figure 3-52, and Figure 3-55) grew perpendicular to the flow and occlude a large (~2.5 mm in diameter) channel. The mountains appear to have been growing faster near the apex due to a higher shear rate that promotes thrombus growth rate (Mehrabadi et al., 2016). The faster growth at the apex region can constrict the lumen, creating a larger recirculation area distal that may accumulate RBCs (L5), but proximal region (L2-3) continues to grow at a lower growth rate compared to the apex region. While the mountains protrude towards the lumen, platelets may aggregate in valleys where reactive surfaces exist. In addition, the platelet aggregates that were captured in valleys may extend downstream (L5). Later, the apex region occludes the channel and stops blood flow, which inhibits the proximal region to grow and occlude the channel. Fibrin may form at the pores when the SIPA clot occluded the lumen, thus lowering the shear rate and enabling the coagulation cascade to occur. These whole processes are illustrated in **Error! Reference source not found.**.

It is critical to know the permeability and composition of a clot in order to effectively deliver the thrombolytic agent and lysis. High permeability of SIPA clot may allow convective drug transport through the inner clot (Diamond, 1999). Although a drug could be transported to the center of the clot through the pores, tPA may not work due to lack of fibrins in a SIPA clot where the histological images only trace amounts of fibrin. Thus, perfusing a thrombolytic agent that reacts with VWF or platelet may be needed to dissolve a SIPA clot.

The clot permeability and mechanical strength from this study are useful values for designing thrombectomy devices. Current simulation model (Chitsaz, Nejat, & Nouri, 2018) and *in vitro* assays (Gunning et al., 2018; Khalil et al., 2017; Y. Liu et al., 2020) used only coagulation clots to test thrombectomy devices. The permeability of the SIPA clot can be used to simulate and design aspirational devices as they use fluid force to remove the arterial thrombi. The mechanical strength of the SIPA clot quantified in the present study could be used to optimize the wire based thrombectomy devices (e.g., stent and coil retriever).

The present study had several limitations. First, only one animal's (porcine) blood was used to generate the clot. However, Para and Ku (2013) found there was no significant difference between human and porcine blood when generating a SIPA clot. In the future, it would be interesting to use human blood (e.g., from polycythemia vera patients for the large tube experiment) and compare the histology and mechanics results. Second, high shear chambers had rigid impermeable walls, and steady flow was applied for the SIPA clot generation. Different materials of walls (PDMS vs. glass) may have different stiffness and may differ in adsorption of hydrophilic compounds. Third, the breakage strength of the clots was estimated from pressure blow-out tests, but more direct measurement of tensile strength may be used to validate the results. Fourth, the brown color of VWF immunostaining in the clot was hard to distinguish from the RBCs (yellow). In the future, it could be interesting to use immunofluorescence staining to compare the relative dominance of VWF vs. fibrin in SIPA and coagulation clots.

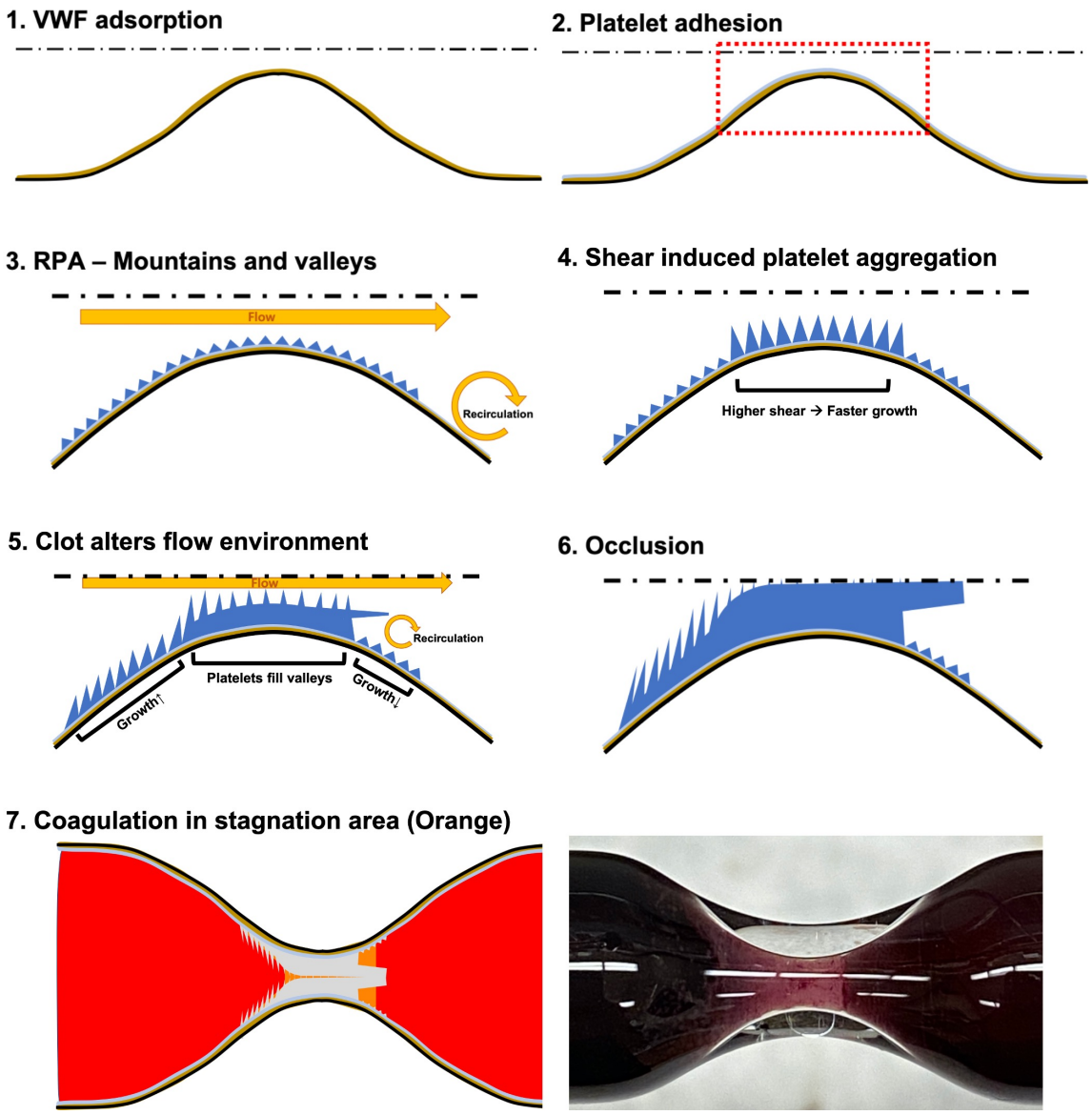

Figure 3-90. Process of SIPA clot formation in a large glass tube.

3.5 Conclusions

A SIPA clot generated in an *in vitro* flow loop, was VWF-platelet-rich and had a heterogeneous structure. SEM images of the clot revealed densely packed platelets, which can be converted into 1.23 billion platelets in the clot. Whereas histological images showed

distinctive structural features for upstream, near the apex, and downstream of the stenosis. Upstream region showed mountain-like platelet aggregates protruding to the central lumen that left a large hole in the center, while RBCs trapped in valleys. Near the apex, dense platelet aggregates throughout the lumen fully occluded the channel. Unactivated platelets were present at the downstream end of the thrombus that ended abruptly and did not extend to the walls located in the flow separation zone. Compared to a coagulation clot, the SIPA clot was three orders of magnitude more permeable, but two-fold stiffer and seven-fold stronger which make it capable of occluding a stenosed coronary artery with a short clot length of less than 2 mm. Due to its distinctive mechanical properties, the SIPA clot may require a new thrombolytic agent and optimized thrombectomy devices for the treatment.

3.6 Acknowledgements

We thank Yolande Berta for her help with the sputter coating and SEM imaging of the SIPA clot and Aqua Asberry for her help with Carstairs staining.

CHAPTER 4. THROMBOLYSIS OF ARTERIAL SIPA CLOTS

4.1 Introduction

An acute ischemic stroke because of an occlusive arterial thrombosis in the carotid artery can lead to a patient's death. More than 700,000 cases of ischemic stroke occur in the United States every year (Mozaffarian et al., 2015; Prabhakaran et al., 2015). The primary goal of ischemic stroke treatment is to retain the blood flow in the brain by removing an occlusive blood clot. The current gold standard for stroke treatment is the use of the IV tPA within 3 hours of the onset of symptoms (Bivard et al., 2013; Prabhakaran et al., 2015).

tPA catalyzes the conversion of plasminogen to plasmin, and plasmin cleaves fibrin (Bivard et al., 2013; Brenner, 1988). The cleavage of fibrins results in fibrin degradation product (Figure 1-3) and lysis of a fibrin-rich clot. However, SIPA clots in arteries are rich in VWF platelets and have less fibrin (Ku & Flannery, 2007). tPA has shown a limited recanalization rate of less than 30% (Bhatia et al., 2010) and a risk reduction of 30% compare to a placebo in stroke patients. In addition, there was no statistically significant decline in the overall mortality with the use of tPA (Chapman et al., 2014). tPA has a high rate of bleeding complications because of the induction of a hyperfibrinolytic state, which deters its clinical use (Crescente et al., 2012; Marder, 2011; Wechsler, 2011).

Clot composition may determine the efficacy of a thrombolytic drug. As arterial thrombi are formed under high shear conditions and are VWF-platelet rich, tPA may not be an efficacious thrombolytic agent for SIPA clots. Therefore, we tested the efficacy of potential novel thrombolytic agents and tPA on SIPA clots. Potential thrombolytic agents that may react with SIPA clots are selected based on the literature.

A Disintegrin and Metalloproteinase with a Thrombospondin Type 1 Modtif, Member 13 (ADAMTS-13) is the protease that cleaves VWF, the main component of SIPA clot formation under high shear rates (Casa et al., 2016; Muia et al., 2014; Para, Bark, Lin, & Ku, 2011). Denorme et al. (2016) showed the potential thrombolytic use of ADAMTS-13 in a mouse model of acute ischemic stroke. They induced arterial thrombosis by applying $FeCl_3$ to mouse arteries. Abciximab is a GPIIb/IIIa inhibitor that blocks interactions between platelets and fibrin or VWF (Coulter Stephanie et al., 2000; Kwon et al., 2002). N-acetylcysteine (NAC) has been shown to cleave plasma VWF and prevent thrombosis (Chen et al., 2011). Furthermore, Martinez de Lizarrondo et al. (2017) demonstrated that NAC can be used as a thrombolytic agent for $FeCl_3$-induced thrombi. S. M. Hastings and Ku (2017) reported that NAC lyses SIPA clot better than tPA, ADAMTS-13, and Abciximab. However, NAC batches were found to have a high variability and the high-efficacy batches contained N,N'-Diacetyl-L-cystine (DiNAC). Therefore, we also tested DiNAC as a thrombolytic agent for SIPA clots. DiNAC is the disulfide dimer of NAC that has been studied for its anti-atherosclerotic effects (Pettersson & Bergstrand, 2003; Wagberg et al., 2001) but not for thrombolytic therapy.

4.2 Methods

4.2.1 Capillary tube preparation

The stenotic glass test sections (ID = 1.5 mm) were made by the Chemistry and Biochemistry Glass Shop at Georgia Institute of Technology. The percent stenosis by diameter reduction ranged from 60% to 80%. Capillary glass tubes were washed and reused multiple times after each experiment. The washing protocol is described as follows.

I. Incubation in a sonicator for 15 min.
II. Incubation in a hot chamber (130°C) or sterilization in a sterilizer.
III. Repeat I and II, 2 times.
IV. Drying in a hot chamber (70°C).

4.2.2 Collagen coating

Fibrillar equine collagen (type I; Chrono-Log Corporation, Havertown, PA) was diluted 9:1 in NaCl (Sigma-Aldrich, St. Louis, MO) and incubated in the test section (10 µL each) at the stenosis for 24 h in a warm, moist environment(Para et al., 2011; Para & Ku, 2013).

4.2.3 Blood collection

Immediately following the slaughter, porcine blood was collected at a local abattoir into 3.5 U/mL heparin (Thermo Fisher Scientific, Waltham, MA) or 3.2% sodium citrate (Sigma-Aldrich, St. Louis, MO). On the same day as the collection, WB was gently agitated using an Orbit LS shaker (Laboratory Supply Network, Atkinson, NH) until perfusion, and it was used in experiments as soon as possible.

4.2.4 Syringe perfusion

Lightly heparinized porcine WB was perfused through the stenotic test section using a syringe pump. The flow rate was set so that the initial wall shear rate in the stenosis was 3,500 s^{-1}. A pressure transducer was connected in-line upstream of the stenosis (Figure 4-1A). A dissecting microscope with a camera (PCO-Tech Incorporated, Romulus, MI) was used to capture images in real time during perfusion. The upstream pressure increased as the SIPA clot grews at the stenotic section, and the syringe pump was paused when the pressure increase reached 30 mmHg, to perfuse the thrombolytic agent. In sequence, agents (tPA, ADAMTS-13, abciximab, NAC, and DiNAC) and a control treatment with PBS were perfused for an hour at a constant flow rate of 1 mL/min. Agent solutions were made by dissolution or dilution in PBS. The *in vitro* flow system setup and image acquisition are shown in Figure 4-1, and the concentrations of each agent are detailed in Table 5. Real-time image capture (5 frames per second) of the stenosis and upstream pressure recording using LabVIEW (National Instruments, Austin, TX) continued throughout the experiment.

Table 5. Thrombolytic agent concentration and replicate number.

Agent	Concentration	Number of replicates
DiNAC	0.02 mM, 0.2 mM, 2 mM, 20 mM, *20 mM	8, 8, 9, 8, 8
NAC	2 mM, 20 mM	7, 5
tPA	20 μg/mL	4
ADAMTS-13	1 μg/mL	4
Abciximab	35 μg/mL	4
PBS	-	10

* Neutralized DiNAC solution

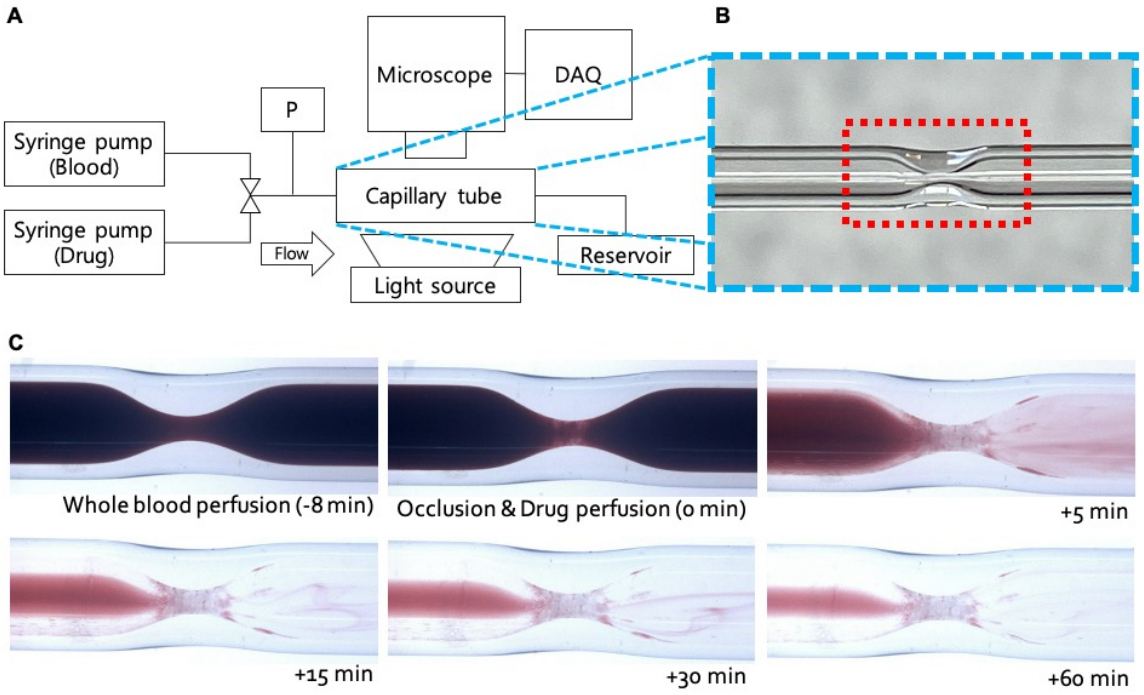

Figure 4-1. The *in vitro* perfusion system for creating platelet-rich, occlusive thrombi under arterial (high) shear rates, followed by perfusion of known and potential lytic agents. (A) Schematic of the arterial flow setup. (B) Close-up of the glass capillary tube with stenosis, which is coated with fibrillar collagen prior to perfusion. The red box denotes the region of interest. (C) Thrombus formation and subsequent perfusion with a PBS control, showing no lysis at the end of the experiment.

4.2.5 Formation and lysis of coagulation clots

PRP was made by separating citrated WB via gravity over a 2 h period and collecting the supernatant. Separation by gravity was employed instead of centrifugation to avoid platelet damage and activation. Citrated WB or PRP was then recalcified with $CaCl_2$ to a final $[Ca^{2+}]$ of 10 mM (Griffin et al., 2019), and 200 µL was transferred into 500 µL centrifuge tubes and allowed to clot and retract for 30 min. The clot was then incubated with 100 µL of either agent or control solution. The treatment solution was exchanged by removing the top 100 µL and replacing it with a fresh solution at 3, 6, 12, 24, and 48 h of incubation.

The weight of the tube was measured immediately post-clot formation and each time the old solution was removed but before it was replaced with fresh solution.

4.2.6 Computational Fluid Dynamics analysis

CFD was used to calculate the drag force acting on the thrombi formed in the stenosis under flow. Simulations were performed using Ansys 19.1 (Ansys Inc, PA, USA). WB was assumed to be a Newtonian fluid of 3.5 cP, and flow was presumed to be laminar, incompressible, steady, continuous, and isothermal because of the low Reynolds number (Re = 16). The capillary tube was modeled with no-slip walls, and a 1 ml/min flow rate was applied at the inlet, with zero-pressure at the outlet, reflecting experimental conditions. Mesh convergence was achieved at 3.8 million tetrahedral cells yielding a residual error of 10^{-9}.

4.2.7 Data analysis

The thrombi surface area (colored green) was calculated using manual pixel counting in the open-source GNU Image Manipulation Program (GIMP, Version 2.10.8, 1995-2018). Surface area reduction was calculated by percent pixel reduction versus the occlusion image. After checking normality of a data, analysis of variance (ANOVA) was used to test for statistical differences between groups, with the significance set at $p < 0.05$. Data are displayed as mean with error bars denoting SEOM.

4.3 Results

4.3.1 DiNAC lysed SIPA clots better than NAC

NAC batches from multiple vendors showed large variability in thrombolytic efficacy on SIPA clots. To find the difference between batches, mass spectrometry was conducted on NAC solutions, and high-efficacy solution was found to have DiNAC. Therefore, DiNAC could be the potential thrombolytic agent that lyses SIPA clots. To test this hypothesis, low (2 mM) and high (20 mM) concentrations of pure NAC and DiNAC solutions were perfused over SIPA clots formed in our established stenotic capillary tube model. Figure 4-2 and Figure 4-3 show the effects of DiNAC and NAC perfusion over 60 min on occlusive thrombi in the glass stenoses. In Figure 4-2, DiNAC dissolved most of the thrombi (> 95%) within 14 min with 2 mM and within 1.5 min with 20 mM. In contrast, NAC did not cause lysis at 60 min (Figure 4-3), leaving most of the thrombi (green) in the stenosis. The thrombus areas after a 60 min perfusion in the capillary tube were compared for DiNAC and NAC, and DiNAC showed a significantly higher reduction of thrombus area (Figure 4-4) for both concentrations (2 mM, $p < 0.001$, 20 mM, $p < 0.01$).

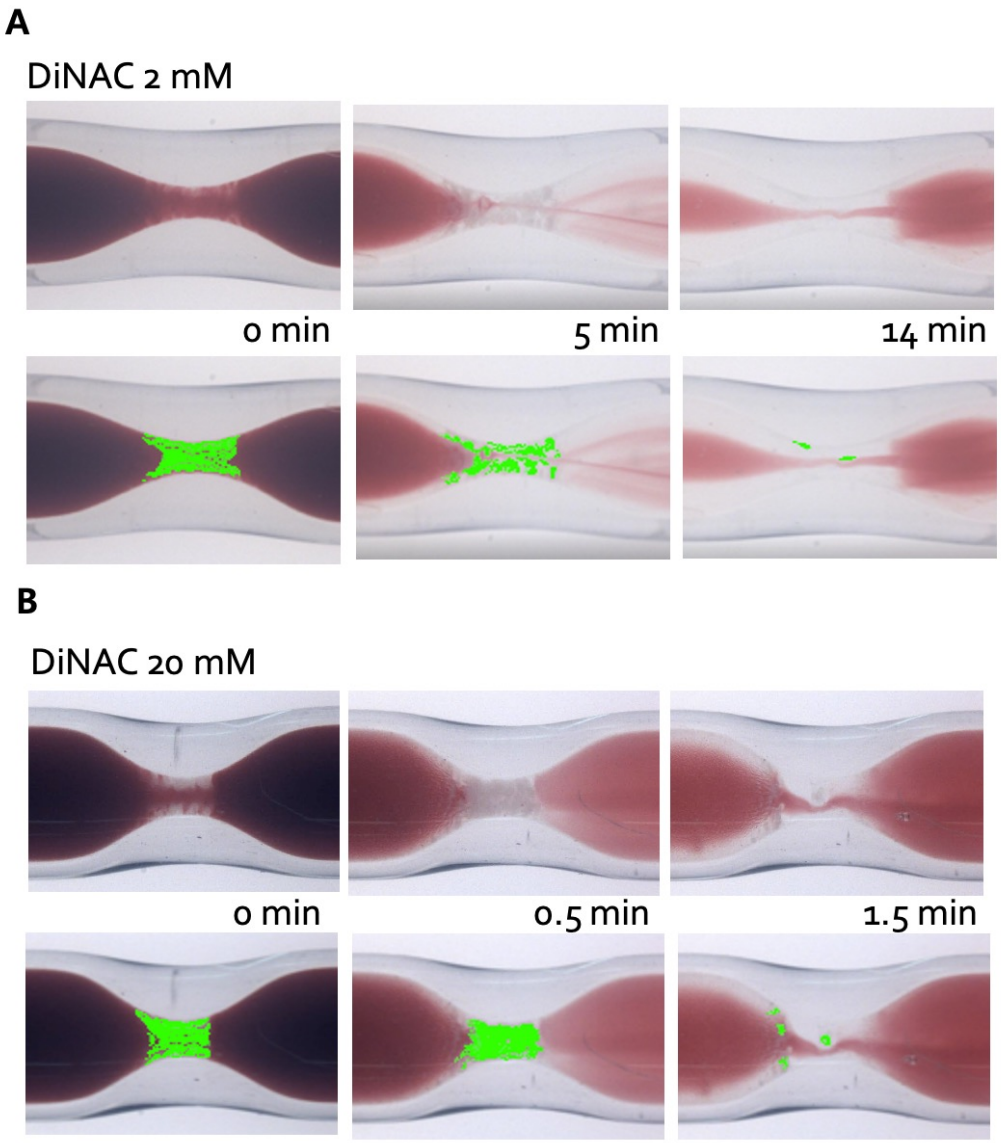

Figure 4-2. Perfusion with DiNAC. The thrombus surface area was determined by pixel counting and is shown in paired images below originals, with the thrombus area highlighted in green. (A) 2 mM DiNAC perfusion showing complete (> 95 % surface area reduction) lysis in 14 min. (B) 20 mM DiNAC perfusion showing complete lysis in 1.5 min.

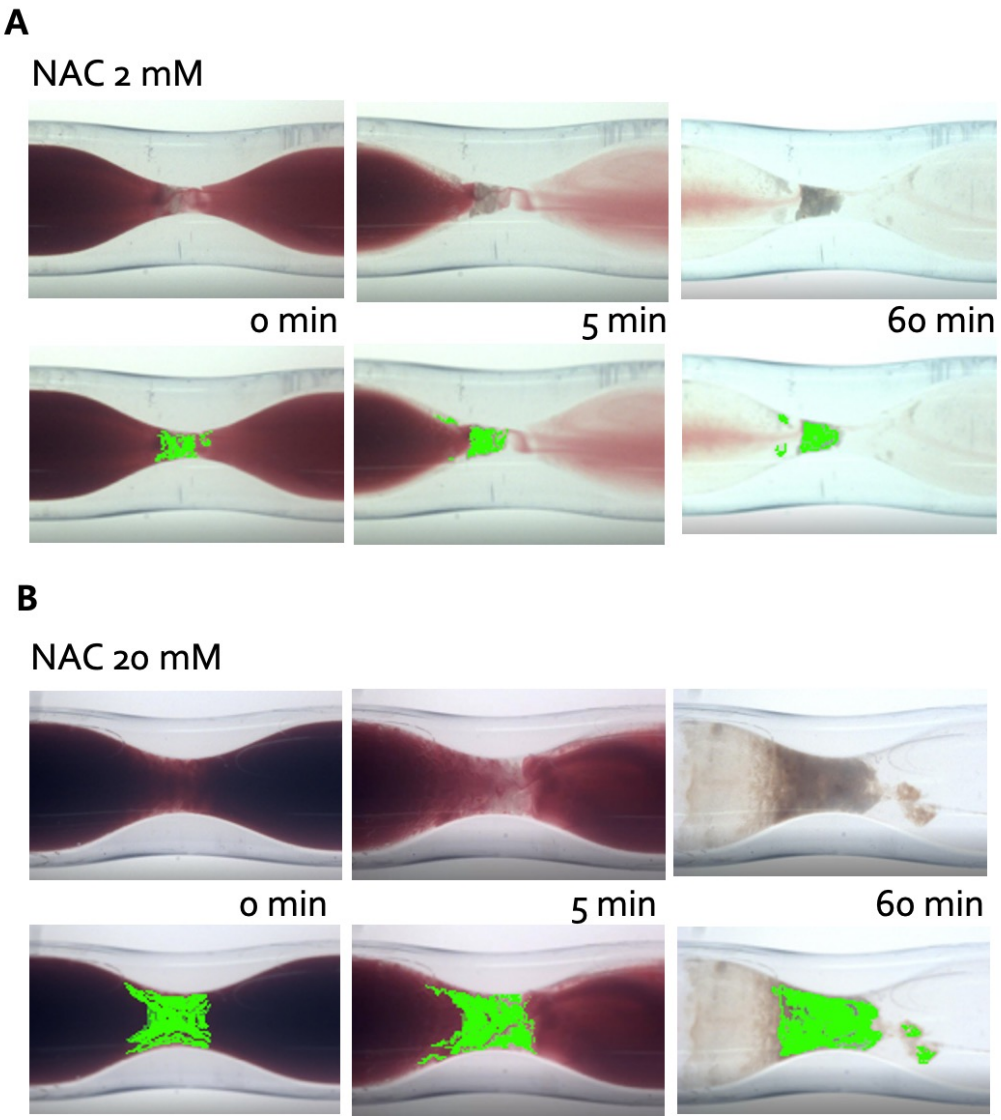

Figure 4-3. Perfusion with NAC. The thrombus surface area was determined by pixel counting and is shown in paired images below originals, with the thrombus area highlighted in green. (A) 2 mM NAC perfusion, with minimal lysis (< 20 % surface area reduction) after 60 min. (B) 20 mM NAC perfusion after 60 min, again with minimal lysis even at increased concentration.

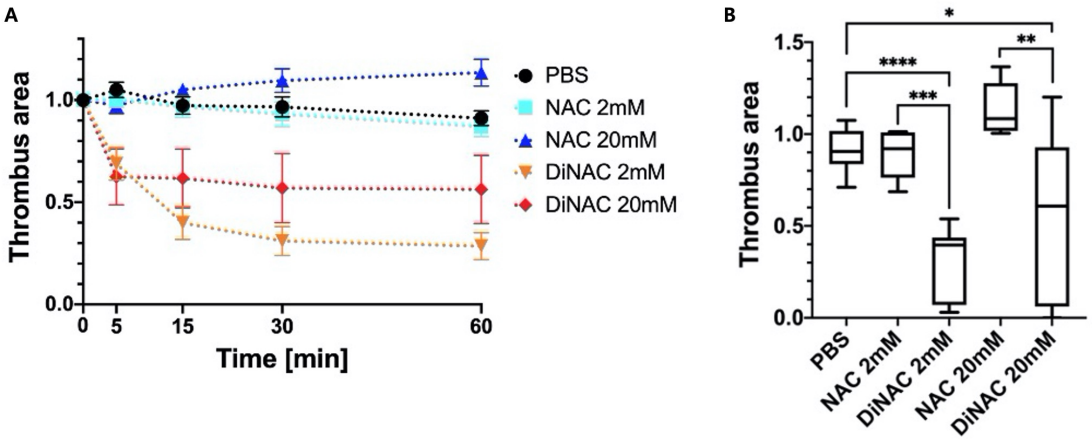

Figure 4-4. Perfusion with DiNAC and NAC. (A) Thrombus area reduction over time. PBS is included as a negative control (black line). (B) Thrombus area after 60 min perfusion with the indicated agent (x-axis). 2 mM and 20 mM DiNAC cause significantly more lysis than the control, while neither concentration of NAC was more efficacious than PBS. DiNAC also was significantly different from NAC at each concentration. * $p < 0.05$; ** $p < 0.01$; *** $p < 0.001$; **** $p < 0.0001$.

4.3.2 Dose response of DiNAC

DiNAC was tested with varying dosages of 0.02 mM, 0.2 mM, 2 mM, and 20 mM to confirm the efficacy. The result demonstrated an increasing reduction of the thrombus area as dosage increased (Figure 4-5). The final thrombus area was minimal at 2 mM (71 ± 20%) and slightly increased at the highest concentration of 20 mM (59 ± 12%). However, this was not significantly different (p = 0.86). The lowest concentration of 0.02 mM DiNAC was not significantly different from the PBS control, but 0.2 mM showed a significantly decreased thrombus area (46 ± 15%, p = 0.02 < 0.05). The 20 mM DiNAC solution was found to be acidic (pH ≈ 2), while 2 mM DiNAC was close to neutral (pH = 7). To test if acidity affected thrombolytic efficacy, the 20 mM DiNAC solution was neutralized with sodium bicarbonate to a final pH = 7. Neutralization of 20 mM DiNAC

improved the variance from 47% to 12% in surface area reduction (44 ± 47% vs 59 ± 12%, $p = 0.77$, Figure 4-5).

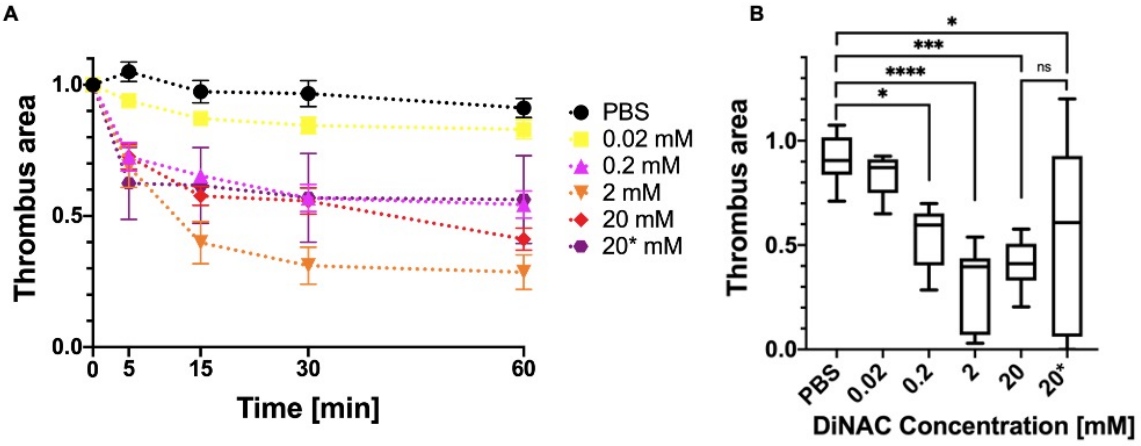

Figure 4-5. DiNAC dosage response with concentrations of 0.02 mM, 0.2 mM, 2 mM, and 20 mM. The * denotes the acidic DiNAC 20 mM solution. (A) Thrombus area reduction over time. The control is shown in black. 0.02 mM DiNAC was not different from the control (yellow), and 2 mM DiNAC (orange) had the greatest efficacy. (B) Thrombus area after 60 min perfusion with increasing concentrations of DiNAC. Concentrations of 0.2 mM and greater were significantly different from the control. Neutralization of DiNAC mitigated variability and increased the surface area reduction (20 mM vs. 20* mM). * $p < 0.05$; *** $p < 0.001$; **** $p < 0.0001$.

4.3.3 Thrombolytic efficacy of the other agents on SIPA clots

A negative control with PBS for 60 min of perfusion reduced the thrombus surface area by 9 ± 12% (Figure 4-1C). Perfusion with 0.02 mg/mL tPA reduced the thrombus surface area by 23 ± 4% (Figure 4-6A), demonstrating a weak thrombolytic effect compare to DiNAC. Perfusion with ADAMTS-13 reduced the thrombus area by 19 ± 8% (Figure 4-6B), and perfusion with Abciximab resulted in a reduction in thrombus area of 22 ± 11% (Figure 4-6C). None of these three agents was significantly different from the PBS control (Figure 4-6D&E: tPA, $p = 0.43$; ADAMTS-13, $p = 0.52$; Abciximab, $p = 0.31$).

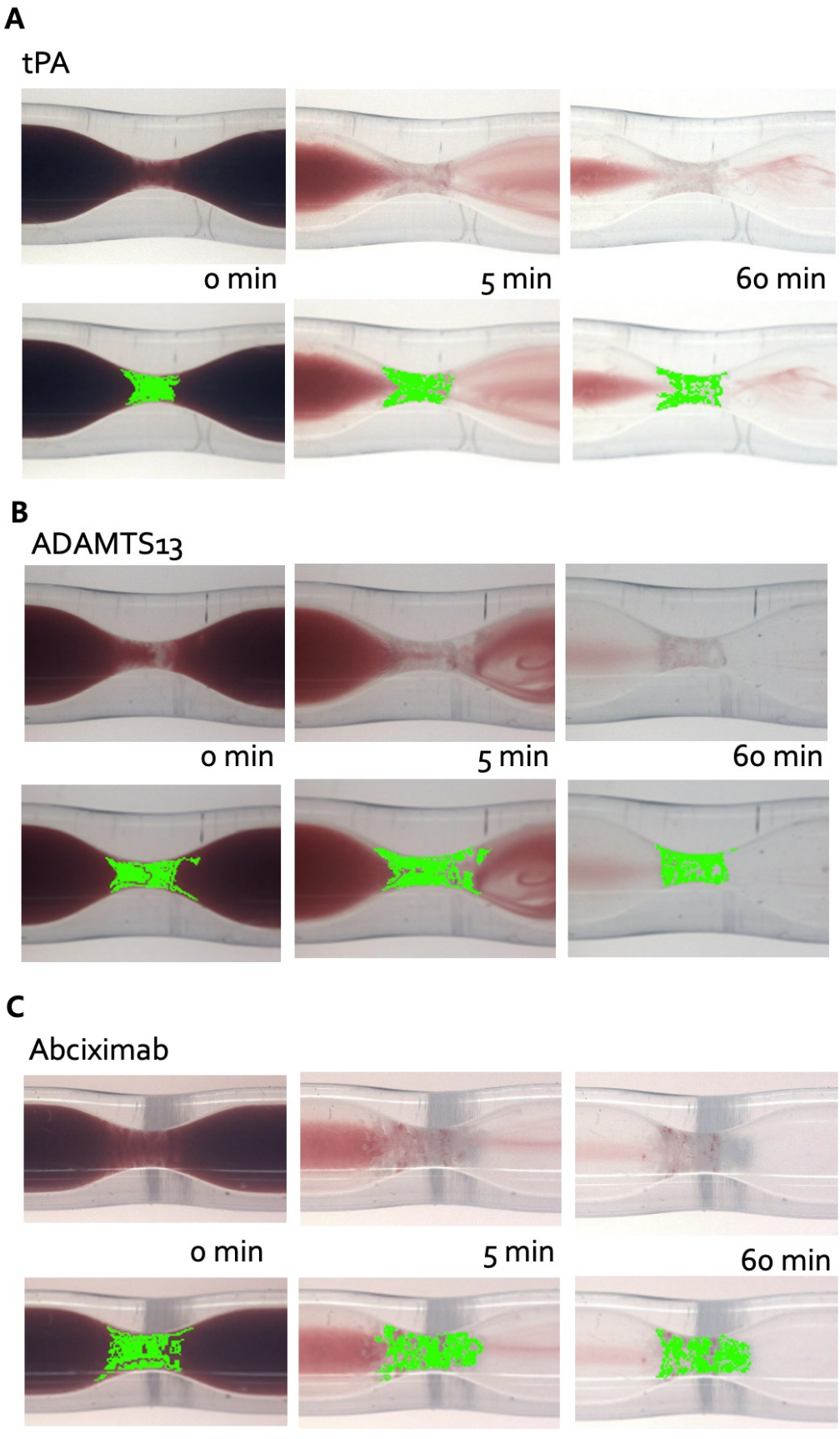
A
tPA
0 min
5 min
60 min
B
ADAMTS13
0 min
5 min
60 min
C
Abciximab
0 min
5 min
60 min

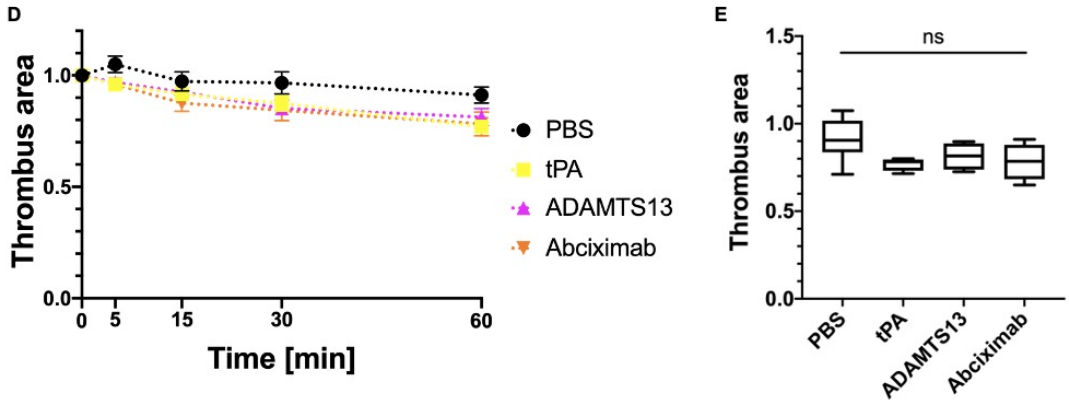

Figure 4-6. Thrombolysis with the other agents. The thrombus area is highlighted in green. Perfusion with tPA (A), ADAMTS-13 (B), and abciximab (C) perfusion showed minimal lysis after 60 min. (D) Thrombus area reduction over time. (E) Thrombus area after 60 min perfusion with the indicated agent (x-axis). Perfusion of tPA, ADAMTS-13, and abciximab had no effect on the white clot, with no differences from the control.

4.3.4 DiNAC does not lyse fibrin-rich coagulation clots

We generated fibrinous coagulation clots by re-calcifying citrated WB (Figure 4-7) and PRP (Figure 4-8) under stagnant conditions, and agents were applied to quantify thrombolytic efficacy. PRP was included to test any potential platelet-specific interactions by agents. Only tPA showed significant thrombolytic efficacy on coagulation clots (Figure 4-9). Between 6 h and 12 h, tPA began to show significantly reduced both clot volume and weight ($p < 0.01$) compared to the PBS control. At the end of the experiment (= 48 hr), tPA lysed more than 80% of both WB and PRP coagulation clots. Whereas, the other agents (DiNAC, NAC, and ADAMTS-13) did not demonstrate a significant reduction in clot size or volume.

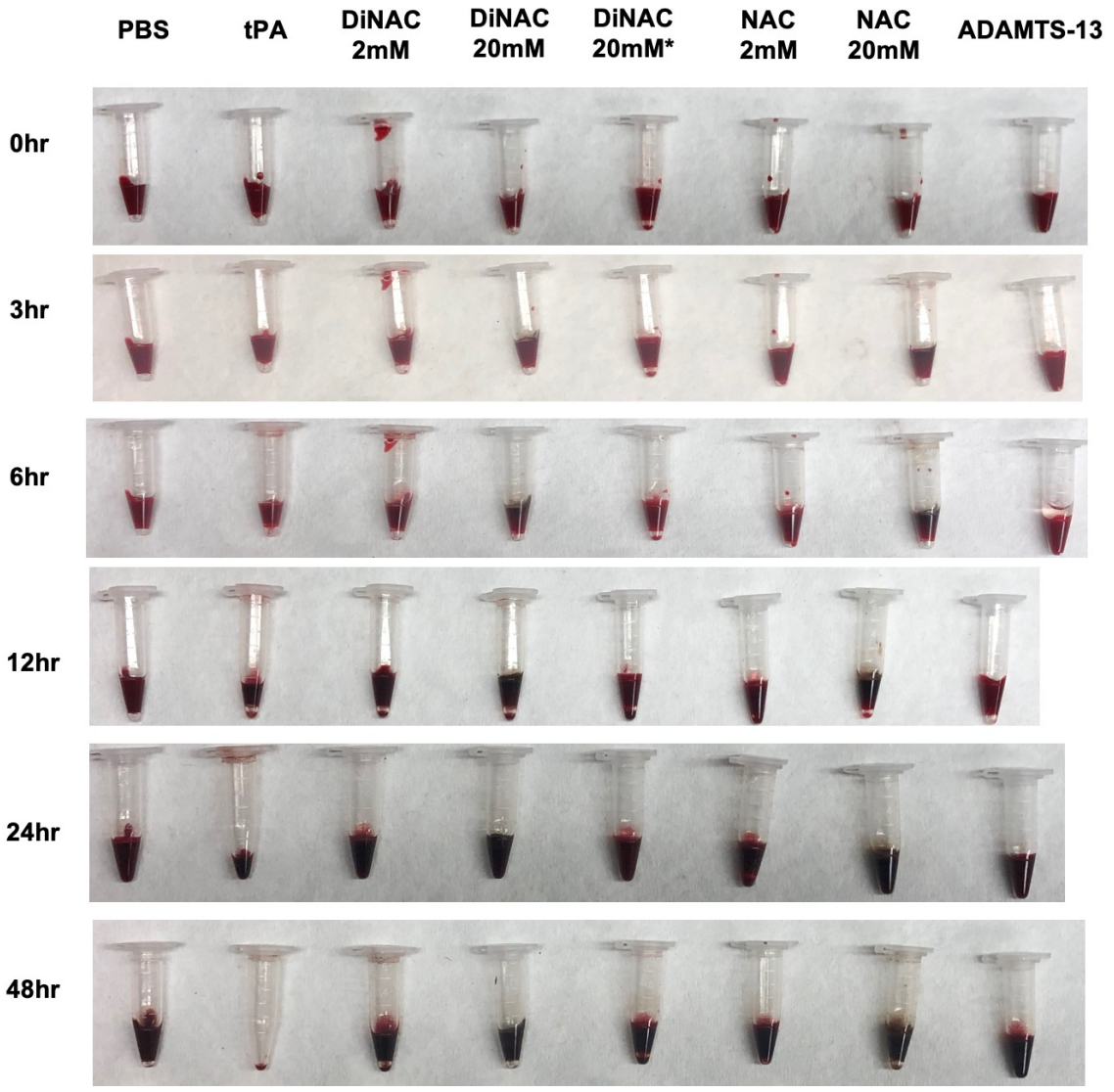

Figure 4-7. Lysis results on WB coagulation clots formed under stagnant conditions over 48 h (n = 3 per agent). Only tPA showed a large decrease in coagulation clot volume.

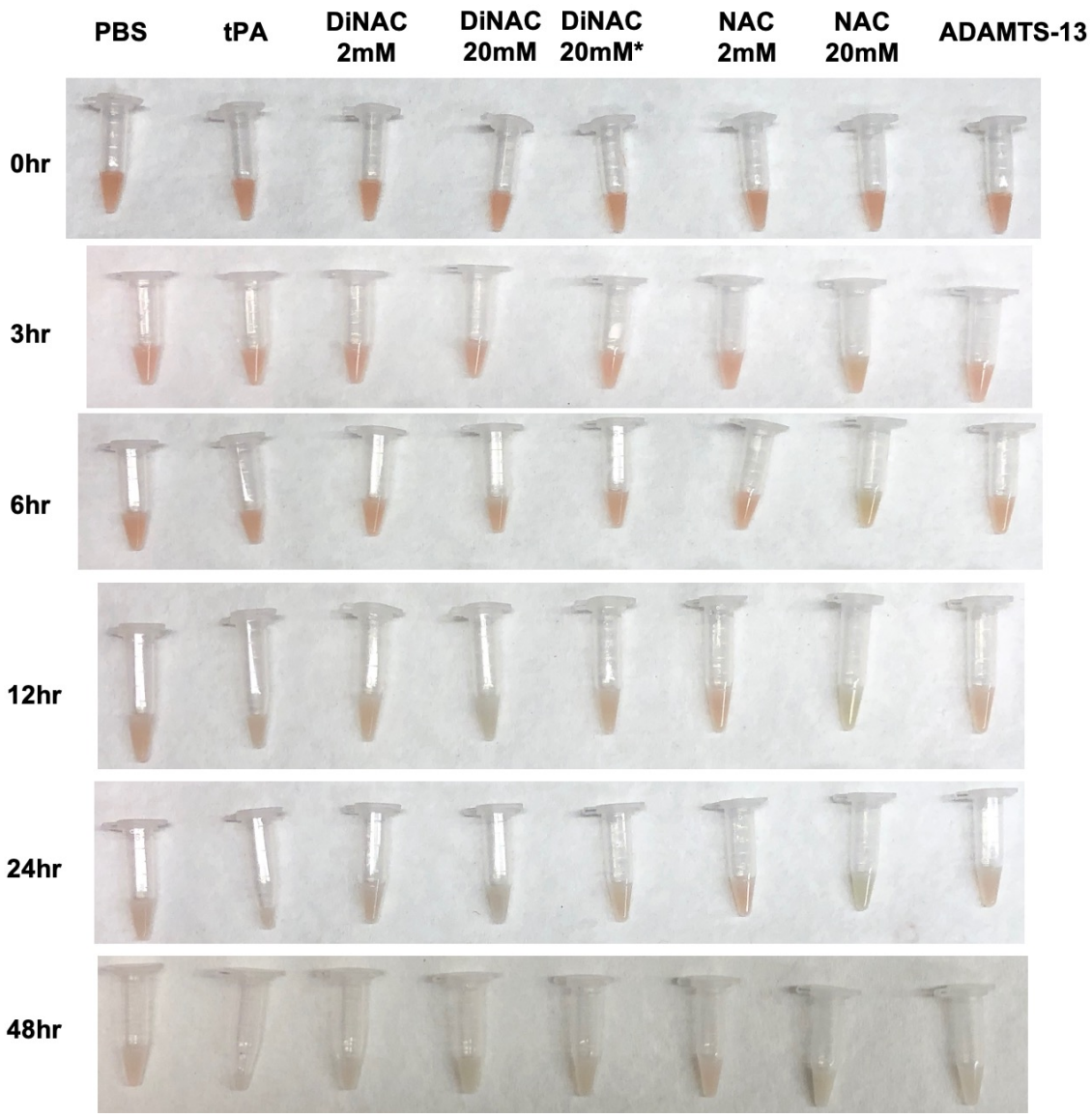

Figure 4-8. Lysis results on PRP coagulation clots formed under stagnant conditions over 48 h (n = 3 per agent). Only tPA showed a large decrease in coagulation clot volume.

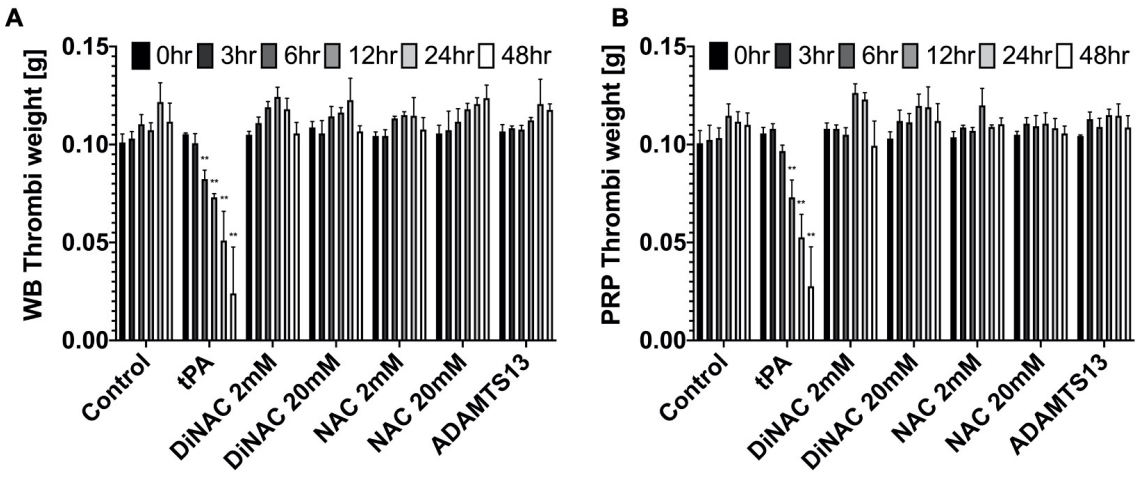

Figure 4-9. Change of clot weight with WB (A) and PRP (B) clot in 48 h. tPA-lysed clots resulted in changes in weight significantly different from baseline after 6 h for WB (A) and 12 h for PRP (B) (26 % and 36 % reduction, respectively, **$p < 0.01$). DiNAC, NAC, and ADAMTS-13 had no effect on red clots, with no differences from baseline nor control.

4.3.5 SIPA clot elongates and break during DiNAC perfusion

DiNAC perfusion on the SIPA clot led to a break apart of thrombus in fragments. The initial fragments were smaller than the entire thrombus with some retained thrombus on the glass wall. Thus, it is not likely that the glass-collagen interface was the source of the initial weakness. The thrombi fragments were stretched downstream and towards the center of the lumen, away from the wall, and often remained tethered by a strand longer than 1 mm at the stenotic region. The strand shaped thrombi remained tethered for several minutes, before eventual breakage (Figure 4-10A).

The flow field around thrombi in the tube were simulated using CFD (Figure 4-10B) to quantify the shear stresses and hydrodynamic drag forces on the fragments. The modeled thrombi fragments are colored in gray in Figure 4-10B. High-velocity jet-like flow was seen in the stenosis with recirculation downstream (Figure 4-10C). Maximum

shear rate occurred at the stenosis reached over 15,000 s^{-1} while shear rates of approximately 4,000-8,000 s^{-1} acted on the surface of thrombus downstream (Figure 4-10D). The total drag force was 380 nN for the smaller fragment and 780 nN for the larger fragment (Figure 4-10E). A typical bond strength is on the order of 100 pN, thus, there needs to be many thousands of bonds to hold thrombi remain tethered.

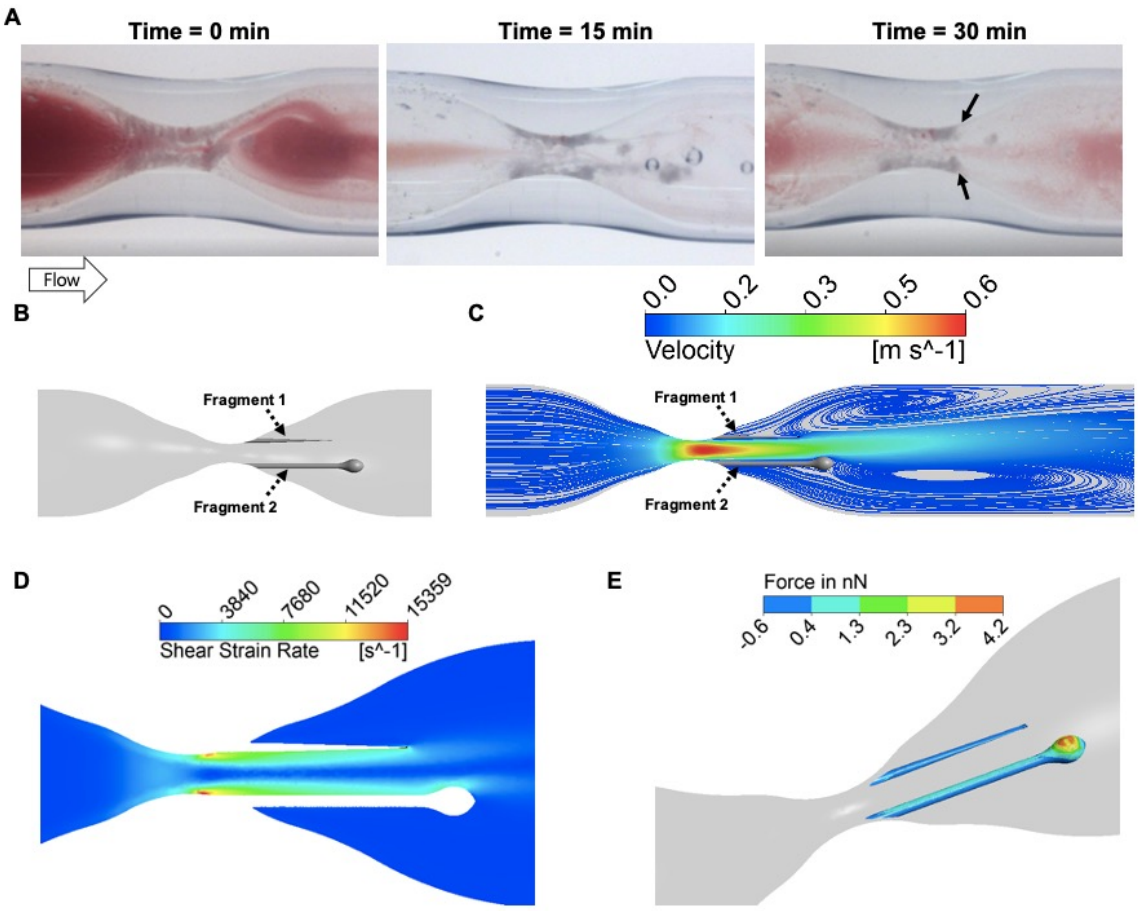

Figure 4-10. Simulation of flow and force through the stenosis using CFD. (A) Structure of a thrombus during elongation and breakage at 0, 15, and 30 minutes of DiNAC perfusion. Black arrows denote points of tether breakage. (B) Computer model of the attached thrombus fragments at 15 min. (C) Velocity streamlines showing a jet-like flow and recirculation downstream of the elongated thrombus colored in gray. (D) Shear strain rate around the thrombus. A maximum shear of

15,000 s^{-1} (red) was observed in the throat of stenosis. (E) Drag force acting on the thrombi surface. The thrombus 2 fragment experiences a maximum force of > 4 nN.

4.4 Discussion

Different thrombolytic agents were efficacious for different types of clots. Compared to the other agents, DiNAC showed a significantly high thrombolytic efficacy for SIPA clots. A disulfide bond between two NAC monomers forms DiNAC that has been studied for its anti-atherosclerotic effects (Pettersson & Bergstrand, 2003; Wagberg et al., 2001) but not for a thrombolytic effect. DiNAC reduced more thrombus area as its concentration increased from 0.02 mM to 0.2 mM and 2 mM, but it had slightly less efficacy at 20 mM. The acidic 20 mM DiNAC solution showed lower variability when neutralized with sodium bicarbonate. In the process of thrombolysis by DiNAC, a SIPA clot broke into multiple fragments, and some fragments elongated and floated in the flow while tethering to the surface. The thrombus fragments eventually detached, broken into smaller fragments, and washed away from the stenotic region. The length of a stretched thrombus was in the order of millimeters, which can be expected to be VWF strands. When a thrombus was stretched in the flow, the hydrodynamic drag acting on the surface was quantified to be 380 ~ 780 nN. The bond strength of GPIb (T. Yago et al., 2008) and GPIIb/IIIa is on the order of ~100 pN. Thus, many thousands of bonds are required for a thrombus to be tethered, and it is consistent with previous bond number estimates by Wellings and Ku (2012). On the other hand, DiNAC did not show any significant lysis if the coagulation clots. Thus, DiNAC may not cause severe bleeding, which has limited the use of tPA in patients. The limited effect of DiNAC on PRP clots suggests that DiNAC is not reacting with the

platelets, but it may be interacting with VWF or the VWF-platelet bond to achieve thrombolysis.

Meanwhile, tPA showed a significant thrombolytic efficacy on WB and PRP coagulation clots compared to the other agents in this study. tPA lysed coagulation clots with an approximate front speed of 3.5 μm/min. This is comparable to the other *in vitro* fibrinolytic assays (Bannish, Chernysh, Keener, Fogelson, & Weisel, 2017; Tasci et al., 2017). tPA breaks down fibrins by activating plasminogen into plasmin. Thus, this process requires the presence of endogenous plasminogen and it occurs within minutes of chemical reaction for the lysis (Hoylaerts, Rijken, Lijnen, & Collen, 1982; Piebalgs et al., 2018). Coagulation clots may form after a SIPA clot occludes an artery, thus it could be beneficial to co-administer tPA with DiNAC.

SIPA clots were not lysed effectively by tPA, ADAMTS-13, Abciximab, or NAC. tPA may lyse SIPA clots better with additional plasminogen in the system. Tersteeg et al. (2014) suggested that plasmin is a potential back-up chemical for ADAMTS-13, and they showed that plasmin degrades platelet-VWF complexes. ADAMTS-13 is known to cleave ULVWF when it is stretched under high shear conditions (Crescente et al., 2012; Gurevitz et al., 1998). Furthermore, ADAMTS-13 has been shown to have potential antithrombotic and thrombolytic effects *in vivo* (Crescente et al., 2012; Denorme et al., 2016). In the clot, the VWF may be sufficiently stretched for ADAMTS-13 to access and cleave the VWF, but spatial obstruction might keep ADAMTS-13 (molecular weight 190 kDa) from penetrating the thrombus, compared with a small molecule like DiNAC (molecular weight

324 Da), as thrombus must be tightly packed with platelets and VWFs. Using an *in vivo* $FeCl_3$ injury model, Crescente et al. (2012) found that both tPA and ADAMTS-13 reduced thrombus size (by 53.2% and 62.3%, respectively) after a 60-min treatment. They used a higher concentration of ADAMTS-13 (4 μg/mL), which may account for the differences in our results. Because of the prohibitively high cost of ADAMTS-13, tests were limited to the concentration the level of ADAMTS-13 in normal plasma (1 μg/mL) (Soejima et al., 2006). Abciximab has shown synergetic effect when used with thrombolytic agents, as it blocks GPIIb/IIIa bonds and prevent platelet aggregation observed in patients treated with tPA (Coulter Stephanie et al., 2000; Kwon et al., 2002). However, no significant thrombolytic effect was found in this study with abciximab alone. As a future study, it would be interesting to test abciximab together with other agents. Currently, NAC is used to treat chronic obstructive lung disease by reducing the size of mucin multimers. VWF is very similar to the mucin multimers in structure (Chen et al., 2011; Perez-Vilar & Hill, 1999) and Chen et al. (2011) confirmed VWF cleavage by NAC, motivating this study to use NAC as a potential thrombolytic agent for SIPA clot. Martinez de Lizarrondo et al. (2017) demonstrated the thrombolytic efficacy of NAC by using an *in vivo* mouse model. However, they found limited reperfusion of less than 40% with NAC alone. Other proteolytics (e.g., trypsin) can be tested in the current experimental set-up in future.

There are limitations to this study. To transport blood from the abattoir and prevent any contact activation, a light heparin (3.5 IU/mL) was used as an anticoagulant. Heparin interrupts thrombin, so it does not disrupt the SIPA process, but it may affect coagulation downstream or in a recirculation region with low shear. Porcine blood can be different from human blood, but the difference is expected to be minimal (Mehrabadi et al., 2016). The

stenotic region was viewed from a top-down direction, and only 2-dimensional images were recorded. Thus, lysis of a thrombus was measured by quantifying area reduction. A 3-dimensional imaging technique may produce new information about the reduction of thrombus volumetric or the initial lysis site inside the thrombus. The flow was paused before the thrombus became too occlusive to deliver agents efficiently. Delivery of DiNAC (e.g., IV, oral, and catheter infusion) is left for a future study. When switching the syringe, there is mixing between agents and blood, but a limited supply of blood plasma may constrain thrombolytic efficacy of tPA (plasmin) or ADAMTS-13 (ions). As a future study, using an *in vivo* mouse model could be beneficial, since it uses conditions that are closer to clinical circumstances and the toxicity of the agent can be quantified. In addition, clarifying the mechanism behind the thrombolytic efficacy of DiNAC is remains for future study.

4.5 Conclusion

DiNAC was highly efficacious in the lysis of SIPA clots created in an *in vitro* stenotic coronary artery model perfused under high shear stress. DiNAC demonstrated significantly higher thrombolytic efficacy than NAC and other agents in this setting, including tPA and ADAMTS-13. DiNAC was unable to lyse coagulation clots in a stagnant setting, while tPA was highly efficacious in the latter system. These results indicate the possibility of DiNAC as an effective thrombolytic agent against arterial thrombosis without the side effects of severe hemorrhage associated with current thrombolytic therapies.

CHAPTER 5. CONCLUSIONS AND FUTURE WORK

A combination of *in silico*, *in vitro*, and *in vivo* methods were used to investigate the role of α-granule on SIPA clot formation. To initiate the RPA phase and induce SIPA under high shear condition, α-granule release from platelets was necessary. Among many chemicals in an α-granule cargo, VWF is expected to play an essential role under high shear conditions. Thus, it would be interesting to explicitly study platelet VWF by developing and using genetically modified mice. Also, it would be interesting to perfuse GPS patient's blood in the microfluidic assay to confirm the *Nbeal2*$^{-/-}$ mice experiment results. Lastly, α-granule could be a potential new target for pharmacological interventions to prevent SIPA clot formation in myocardial infarction or stroke patients. In the past, membrane-active drugs (e.g., chloroquine, hydroxychloroquine, camoquine and quinacrine) have been studied to prevent platelet α-granule release (Prowse, Pepper, & Dawes, 1982). These drugs can be tested through *in vitro* and *in vivo* models in this study and see if it prevents SIPA clot and has less bleeding complication compared to current antithrombotic agents (e.g., aspirin, abciximab, and clopidogrel).

SIPA clots were fabricated in *in vitro* flow loops to investigate the structure and quantify mechanical properties: permeability, breakage strength, and modulus. SIPA clot was VWF-platelet-rich and had pores where RBCs are trapped. The SIPA clot was three orders of magnitude more permeable, but two-fold stiffer and seven-fold stronger than the coagulation clot. Based on measured breakage strength, calculation showed that the SIPA clot is capable of resist and occlude a stenosed coronary artery within 2 mm clot length. Due to its distinctive properties, the SIPA clot may require a new thrombolytic agent and optimized thrombectomy devices for the treatment. A large SIPA generated in a closed *in*

vitro flow loop could be useful to study heterogeneity, to perform a tensile test, and to test thrombectomy devices. It can also be used to see how SIPA clot's mechanical properties change within various chemical environments (e.g., thrombolytic agent). The quantified mechanical properties can be used to perform fluid-structure interaction (FSI) simulation to study how does the SIPA deform and fracture under arterial flow condition.

DiNAC demonstrated a high thrombolytic efficacy on VWF-platelet-rich SIPA clot that was generated in an *in vitro* stenotic coronary flow model. DiNAC showed significantly higher efficacy than the other thrombolytic agents: NAC, tPA, ADAMTS-13, and abciximab. Meanwhile, DiNAC did not lyse fibrin-rich coagulation clots, whereas tPA lysed the clots significantly. Thus, DiNAC has the potential to be an effective thrombolytic agent against arterial thrombosis without the side effects of severe hemorrhage associated with current thrombolytic therapies. The next step would be to test DiNAC in an *in vivo* mice model to confirm the thrombolytic efficacy, to estimate bleeding risk, and to assess toxicity. The present study focused on efficacy evaluation; thus, the delivery and mechanism of DiNAC remain as future work. Lastly, a combination of multiple thrombolytic agents could be an interesting subject for future study. After the vessel occlusion, the coagulation clot may form at each end of SIPA clot due to a stagnant flow condition. Thus, coadministering DiNAC and tPA could be beneficial for a particular clinical situation.

APPENDIX A. FOLTS-LIKE ARTERIAL STENOSIS MODEL

Adapted from Folts, Crowell, and Rowe (1976) with input from the Di Paola Lab.

METHODS

I. Pre-procedure

a. Anesthesia solution: Make cocktail of ketamine (100 mg/mL), xylazine (100 mg/mL), saline with 1:0.1:8.9 ratio.

b. Measure the weight of the mouse.

II. Anesthesia

a. Grasp back of the mouse's neck.

b. Do IP (Intraperitoneal) injection based on the mouse's weight (0.1 mL/10g)

*Caution: Air bubbles in the syringe can kill the mouse. Remove air bubbles before the injection.

c. Leave it for 5~10min.

d. Clip the tail to check if the mouse is still awake.

e. If the mouse reacts, wait for another 5 min or inject more anesthesia.

*Caution: Too much anesthesia can kill the mouse.

III. Dissection

a. Place mouse on its back. Fix mouse's legs.

b. Cut skin around the neck.

c. Remove fat and muscles to expose carotid artery.

The carotid artery is located at right next to the white colored throat (0.5~0.6 mm in diameter).

IV. Isolation

a. Carefully find carotid artery using forceps.

b. Remove fat and nerves around the artery.

   *Fat and nerves can interrupt flow measurement.

c. Place forceps below the artery.

d. Place a silk thread on the tip of the forceps.

e. Pull the thread and make a loose knot.

V. Flow probe placement

a. Place a flow probe on the artery.

b. Put saline on the probe if it's necessary.

c. Check the flow rate (0.3~0.8 mL/min).

   *If the flow rate is too low or negative, remove the probe and check the artery. Remove fat around the artery if it is necessary.

d. Wait around 2 min for the flow stabilization.

VI. Suture stenosis

a. Carefully tighten the knot.

b. Wait ~2 min for the flow stabilization. Go for 75% first, wait, then for 50%.

c. Check flow rate if it's 50% of initial flow rate.

   *If the flow went below 0, untie the knot.

d. Repeat A to C.

e. Wait ~2 min for the flow stabilization.

VII. Mechanical injury

a. Crush the vessel using forceps.

b. Make sure flow rate at least goes down to 0 mL/min.

c. Repeat 3 times.

VIII. Post-process

a. Collect the vessel (and the clot) if it is necessary.

b. Euthanasia the mouse.

c. Save the flow rate data.

APPENDIX B. SIPA CLOT GENERATION PROTOCOL

MATERIALS: Heparinized blood (3.5 U/mL) 450 mL.

METHODS

I. Collagen coating

a. Collagen solution: Make cocktail of collagen and saline with 1: 9 ratio.

b. Place 60 µL of collagen solution on stenosis of the large glass tube.

c. Make a mark on the large glass tube and leave it stationary in a container for 1 hour.

d. Rotate the tube 180 degree and leave in the container for 23 hours.

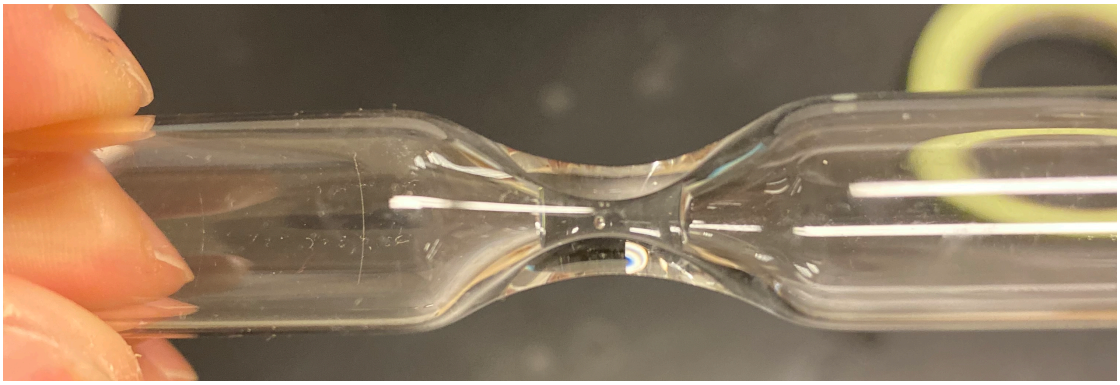

Figure B - 1. A large glass tube with collagen solution placed at the stenosis.

II. Flow loop set-up

a. Take out the large glass tube and flush with PBS.

b. Connect the large glass tube to tubings.

c. Set roller pump's flow rate to zero.

III. Blood preparation

a. Filter the blood to avoid any emboli in the circuit.

b. Put blood in a 500 mL beaker.

IV. Blood perfusion

a. Put inlet tube into the 500 mL beaker (lower reservoir).

b. Slowly increase the roller pump flow rate to fill the upper reservoir.

c. Raise the outlet tube to avoid any bubble formation.

d. Put outlet tube into the lower reservoir.

e. Adjust the flow rate to achieve constant pressure gradient (constant blood volume at the upper reservoir).

Figure B - 2. A closed *in vitro* flow loop set-up.

f. Lower down the flow rates every ~2 min as thrombus grow in the large glass tube.

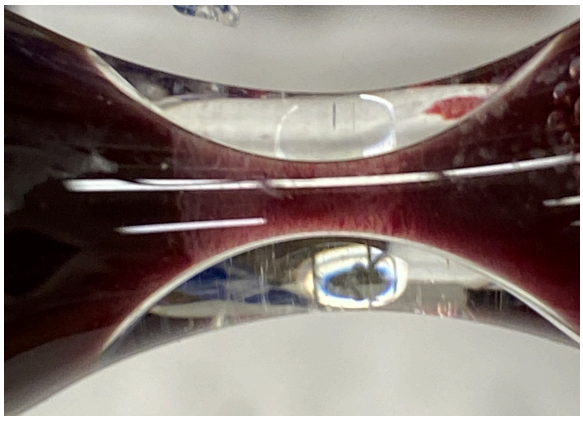

Figure B - 3. Growing SIPA clot at a large glass tube.

g. When the flow rate is lower down to the minimum flow rate (5 mL/min), turn off the pump and leave the circuit 30 min ~ to achieve a complete occlusion.

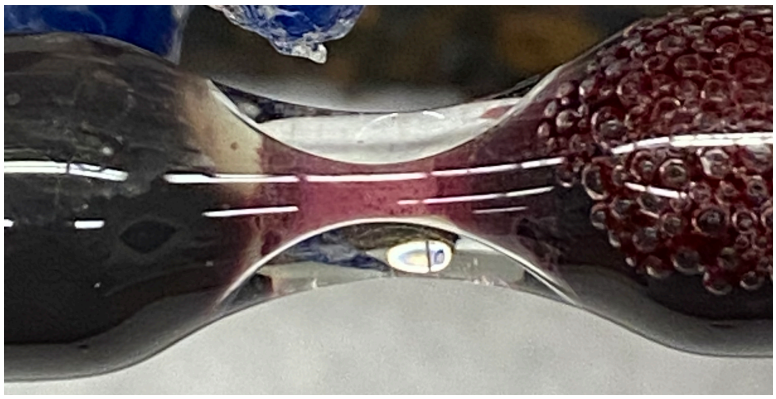

Figure B - 4. An occlusive SIPA clot formed in a large glass tube.

V. Clot retrieval

a. Drain blood from the circuit.

b. Lightly flush the large glass tube with tap water.

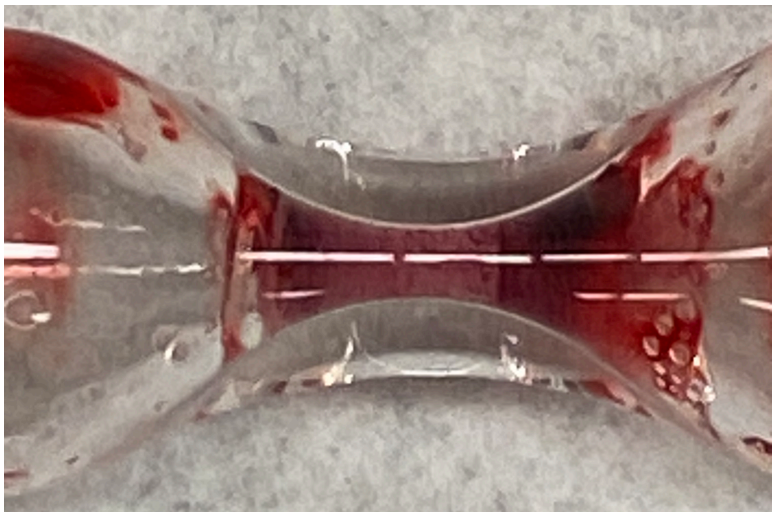

Figure B - 5. A large glass tube after drain.

c. Inspect the circuit for any blood clot formation.

d. With a needle, detach transparent sheets at upstream and downstream.

e. Put the needle between clot and large glass tube wall and swirl to detach the clot from the large glass tube.

f. Retrieve the clot using forceps.

Figure B - 6. A retrieved SIPA clot.

REFERENCES

Aarts, P. A., Steendijk, P., Sixma, J. J., & Heethaar, R. M. (1986). Fluid shear as a possible mechanism for platelet diffusivity in flowing blood. *Journal of biomechanics, 19*(10), 799-805.

Aarts, P. A., van den Broek, S. A., Prins, G. W., Kuiken, G. D., Sixma, J. J., & Heethaar, R. M. (1988). Blood platelets are concentrated near the wall and red blood cells, in the center in flowing blood. *Arteriosclerosis: An Official Journal of the American Heart Association, Inc., 8*(6), 819-824.

Adams, H. P., Jr. (2003). Stroke: a vascular pathology with inadequate management. *Journal of Hypertension, 21*. Retrieved from https://journals.lww.com/jhypertension/Fulltext/2003/06005/Stroke__a_vascular_pathology_with_inadequate.2.aspx

Albers, C. A., Cvejic, A., Favier, R., Bouwmans, E. E., Alessi, M.-C., Bertone, P., . . . Ouwehand, W. H. (2011). Exome sequencing identifies NBEAL2 as the causative gene for gray platelet syndrome. *Nature Genetics, 43*, 735. Retrieved from https://doi.org/10.1038/ng.885

Arrarte Terreros, N., Tolhuisen, M. L., Bennink, E., de Jong, H. W. A. M., Beenen, L. F. M., Majoie, C. B. L. M., . . . Marquering, H. A. (2020). From perviousness to permeability, modelling and measuring intra-thrombus flow in acute ischemic stroke. *Journal of biomechanics, 111*, 110001. doi:https://doi.org/10.1016/j.jbiomech.2020.110001

Ashton, J. H., Vande Geest, J. P., Simon, B. R., & Haskett, D. G. (2009). Compressive mechanical properties of the intraluminal thrombus in abdominal aortic aneurysms and fibrin-based thrombus mimics. *J Biomech, 42*(3), 197-201. doi:10.1016/j.jbiomech.2008.10.024

Astrup, T., & Müllertz, S. (1952). The fibrin plate method for estimating fibrinolytic activity. *Archives of Biochemistry and Biophysics, 40*(2), 346-351. doi:https://doi.org/10.1016/0003-9861(52)90121-5

Astrup, T., & Permin, P. M. (1947). Fibrinolysis in the Animal Organism. *Nature, 159*(4046), 681-682. doi:10.1038/159681b0

Bannish, B. E., Chernysh, I. N., Keener, J. P., Fogelson, A. L., & Weisel, J. W. (2017). Molecular and Physical Mechanisms of Fibrinolysis and Thrombolysis from Mathematical Modeling and Experiments. *Scientific Reports, 7*(1), 6914. doi:10.1038/s41598-017-06383-w

Bark, D. L., Jr., & Ku, D. N. (2010). Wall shear over high degree stenoses pertinent to atherothrombosis. *J Biomech, 43*(15), 2970-2977. doi:10.1016/j.jbiomech.2010.07.011

Bark, D. L., Jr., Para, A. N., & Ku, D. N. (2012). Correlation of thrombosis growth rate to pathological wall shear rate during platelet accumulation. *Biotechnol Bioeng, 109*(10), 2642-2650. doi:10.1002/bit.24537

Bark Jr, D. L., & Ku, D. N. (2010). Wall shear over high degree stenoses pertinent to atherothrombosis. *Journal of biomechanics, 43*(15), 2970-2977.

Bergmann, S. R., Fox, K. A., Ter-Pogossian, M. M., Sobel, B. E., & Collen, D. (1983). Clot-selective coronary thrombolysis with tissue-type plasminogen activator. *Science, 220*(4602), 1181-1183. doi:10.1126/science.6602378

Bhatia, R., Hill Michael, D., Shobha, N., Menon, B., Bal, S., Kochar, P., . . . Demchuk Andrew, M. (2010). Low Rates of Acute Recanalization With Intravenous Recombinant Tissue Plasminogen Activator in Ischemic Stroke. *Stroke, 41*(10), 2254-2258. doi:10.1161/STROKEAHA.110.592535

Bitar, A., & Kreutz, R. P. (2013). Role of Thrombelastography (TEG) in Risk Assessment and Guidance of Antithrombotic Therapy in Patients with Coronary Artery Disease. *Drug Development Research, 74*(8), 533-540. doi:10.1002/ddr.21112

Bivard, A., Lin, L., & Parsonsb, M. W. (2013). Review of stroke thrombolytics. *Journal of stroke, 15*(2), 90-98. doi:10.5853/jos.2013.15.2.90

Brenner, S. (1988). The molecular evolution of genes and proteins: a tale of two serines. *Nature, 334*(6182), 528-530. doi:10.1038/334528a0

Cadroy, Y., Horbett, T., & Hanson, S. (1989). Discrimination between platelet-mediated and coagulation-mediated mechanisms in a model of complex thrombus formation in vivo. *The Journal of laboratory and clinical medicine, 113*(4), 436-448.

Casa, L. D., Deaton, D. H., & Ku, D. N. (2015). Role of high shear rate in thrombosis. *Journal of vascular surgery, 61*(4), 1068-1080.

Casa, L. D., Gillespie, S., Meeks, S., & Ku, D. N. (2016). Relative contributions of von Willebrand factor and platelets in high shear thrombosis. *Journal of Hematology & Thromboembolic Diseases, 4*(4).

Casa, L. D., & Ku, D. N. (2014). Geometric design of microfluidic chambers: platelet adhesion versus accumulation. *Biomedical Microdevices, 16*(1), 115-126. doi:10.1007/s10544-013-9811-7

Casa, L. D., & Ku, D. N. (2017). Thrombus Formation at High Shear Rates. *Annu Rev Biomed Eng, 19*(1), 415-433. doi:10.1146/annurev-bioeng-071516-044539

Chapman, S. N., Mehndiratta, P., Johansen, M. C., McMurry, T. L., Johnston, K. C., & Southerland, A. M. (2014). Current perspectives on the use of intravenous recombinant tissue plasminogen activator (tPA) for treatment of acute ischemic stroke. *Vasc Health Risk Manag, 10*, 75-87. doi:10.2147/vhrm.S39213

Chen, J., Reheman, A., Gushiken, F. C., Nolasco, L., Fu, X., Moake, J. L., . . . Lopez, J. A. (2011). N-acetylcysteine reduces the size and activity of von Willebrand factor in human plasma and mice. *J Clin Invest, 121*(2), 593-603. doi:10.1172/jci41062

Chitsaz, A., Nejat, A., & Nouri, R. (2018). Three-Dimensional Numerical Simulations of Aspiration Process: Evaluation of Two Penumbra Aspiration Catheters Performance. *Artif Organs, 42*(12), E406-e419. doi:10.1111/aor.13300

Chueh, J. Y., Wakhloo, A. K., Hendricks, G. H., Silva, C. F., Weaver, J. P., & Gounis, M. J. (2011). Mechanical characterization of thromboemboli in acute ischemic stroke and laboratory embolus analogs. *AJNR Am J Neuroradiol, 32*(7), 1237-1244. doi:10.3174/ajnr.A2485

Collen, D., Topol, E. J., Tiefenbrunn, A. J., Gold, H. K., Weisfeldt, M. L., Sobel, B. E., . . . et al. (1984). Coronary thrombolysis with recombinant human tissue-type plasminogen activator: a prospective, randomized, placebo-controlled trial. *Circulation, 70*(6), 1012-1017. doi:10.1161/01.cir.70.6.1012

Coulter Stephanie, A., Cannon Christopher, P., Ault Kenneth, A., Antman Elliott, M., Van de Werf, F., Adgey, A. A. J., . . . Kleiman Neal, S. (2000). High Levels of Platelet Inhibition With Abciximab Despite Heightened Platelet Activation and Aggregation During Thrombolysis for Acute Myocardial Infarction. *Circulation, 101*(23), 2690-2695. doi:10.1161/01.CIR.101.23.2690

Crescente, M., Thomas, G. M., Demers, M., Voorhees, J. R., Wong, S. L., Ho-Tin-Noe, B., & Wagner, D. D. (2012). ADAMTS13 exerts a thrombolytic effect in microcirculation. *Thromb Haemost, 108*(3), 527-532. doi:10.1160/th12-01-0046

Davies, M. J., & Thomas, A. C. (1985). Plaque fissuring--the cause of acute myocardial infarction, sudden ischaemic death, and crescendo angina. *British Heart Journal, 53*(4), 363. doi:10.1136/hrt.53.4.363

Denorme, F., Langhauser, F., Desender, L., Vandenbulcke, A., Rottensteiner, H., Plaimauer, B., . . . De Meyer, S. F. (2016). ADAMTS13-mediated thrombolysis of t-PA-resistant occlusions in ischemic stroke in mice. *Blood, 127*(19), 2337-2345. doi:10.1182/blood-2015-08-662650

Deppermann, C., Cherpokova, D., Nurden, P., Schulz, J. N., Thielmann, I., Kraft, P., . . . Nieswandt, B. (2013). Gray platelet syndrome and defective thrombo-inflammation in Nbeal2-deficient mice. *J Clin Invest*. doi:10.1172/JCI69210

Deppermann, C., Nurden, P., Nurden, A. T., Nieswandt, B., & Stegner, D. (2013). The Nbeal2(-/-) mouse as a model for the gray platelet syndrome. *Rare Dis, 1*, e26561. doi:10.4161/rdis.26561

Di Martino, E., Mantero, S., Inzoli, F., Melissano, G., Astore, D., Chiesa, R., & Fumero, R. (1998). Biomechanics of abdominal aortic aneurysm in the presence of endoluminal thrombus: experimental characterisation and structural static computational analysis. *Eur J Vasc Endovasc Surg, 15*(4), 290-299. doi:10.1016/s1078-5884(98)80031-2

Diamond, S. L. (1999). Engineering Design of Optimal Strategies for Blood Clot Dissolution. *Annual review of biomedical engineering, 1*(1), 427-461. doi:10.1146/annurev.bioeng.1.1.427

Duffy, S., Farrell, M., McArdle, K., Thornton, J., Vale, D., Rainsford, E., . . . Gilvarry, M. (2017). Novel methodology to replicate clot analogs with diverse composition in acute ischemic stroke. *Journal of NeuroInterventional Surgery, 9*(5), 486. doi:10.1136/neurintsurg-2016-012308

Fernandez, M. F., Ginsberg, M. H., Ruggeri, Z. M., Batlle, F. J., & Zimmerman, T. S. (1982). Multimeric structure of platelet factor VIII/von Willebrand factor: the presence of larger multimers and their reassociation with thrombin-stimulated platelets. *Blood, 60*(5), 1132-1138. Retrieved from https://www.ncbi.nlm.nih.gov/pubmed/6982084

Flynn, D., Francis, R., Halvorsrud, K., Gonzalo-Almorox, E., Craig, D., Robalino, S., . . . White, P. (2017). Intra-arterial mechanical thrombectomy stent retrievers and aspiration devices in the treatment of acute ischaemic stroke: A systematic review and meta-analysis with trial sequential analysis. *European stroke journal, 2*(4), 308-318. doi:10.1177/2396987317719362

Folts, J. D., Crowell, E. B., Jr., & Rowe, G. G. (1976). Platelet aggregation in partially obstructed vessels and its elimination with aspirin. *Circulation, 54*(3), 365-370. doi:10.1161/01.cir.54.3.365

Fu, H., Jiang, Y., Yang, D., Scheiflinger, F., Wong, W. P., & Springer, T. A. (2017). Flow-induced elongation of von Willebrand factor precedes tension-dependent activation. *Nature Communications, 8*(1). doi:10.1038/s41467-017-00230-2

Gasser, T. C., Görgülü, G., Folkesson, M., & Swedenborg, J. (2008). Failure properties of intraluminal thrombus in abdominal aortic aneurysm under static and pulsating mechanical loads. *J Vasc Surg, 48*(1), 179-188. doi:10.1016/j.jvs.2008.01.036

Griffin, M. T., Kim, D., & Ku, D. N. (2019). Shear-induced platelet aggregation: 3D-grayscale microfluidics for repeatable and localized occlusive thrombosis. *Biomicrofluidics, 13*(5), 054106. doi:10.1063/1.5113508

Gunay-Aygun, M., Zivony-Elboum, Y., Gumruk, F., Geiger, D., Cetin, M., Khayat, M., . . . Falik-Zaccai, T. (2010). Gray platelet syndrome: natural history of a large patient cohort and locus assignment to chromosome 3p. *Blood, 116*(23), 4990. doi:10.1182/blood-2010-05-286534

Gunning, G. M., McArdle, K., Mirza, M., Duffy, S., Gilvarry, M., & Brouwer, P. A. (2018). Clot friction variation with fibrin content; implications for resistance to thrombectomy. *Journal of NeuroInterventional Surgery, 10*(1), 34. doi:10.1136/neurintsurg-2016-012721

Gurevitz, O., Goldfarb, A., Hod, H., Feldman, M., Shenkman, B., Varon, D., . . . Inbal, A. (1998). Recombinant von Willebrand factor fragment AR545C inhibits platelet aggregation and enhances thrombolysis with rtPA in a rabbit thrombosis model. *Arterioscler Thromb Vasc Biol, 18*(2), 200-207. doi:10.1161/01.atv.18.2.200

Harrison, P., & Cramer, E. M. (1993). Platelet alpha-granules. *Blood Rev, 7*(1), 52-62.

Harrison, P., & Martin Cramer, E. (1993). Platelet α-granules. *Blood Reviews, 7*(1), 52-62. doi:https://doi.org/10.1016/0268-960X(93)90024-X

Hastings, S. M., Deshpande, S. R., Wagoner, S., Maher, K., & Ku, D. N. (2016). Thrombosis in Centrifugal Pumps: Location and Composition in Clinical and in Vitro Circuits. *The International Journal of Artificial Organs, 39*(4), 200-204. doi:10.5301/ijao.5000498

Hastings, S. M., & Ku, D. N. (2017). Dissolution of Platelet-rich Thrombus by Perfusion of N-acetyl Cysteine. *Research and Practice in Thrombosis and Haemostasis, 1*(S1), 1-1451. doi:10.1002/rth2.12012

Hellums, J. D. (1994). 1993 Whitaker Lecture: biorheology in thrombosis research. *Annals of biomedical engineering, 22*(5), 445-455.

Henderson, N. M., & Thurston, G. B. (1993). A new method for the analysis of blood and plasma coagulation. *Biomedical sciences instrumentation, 29*, 95-102. Retrieved from http://europepmc.org/abstract/MED/8329642

Hinnen, J. W., Rixen, D. J., Koning, O. H. J., van Bockel, J. H., & Hamming, J. F. (2007). Development of fibrinous thrombus analogue for in-vitro abdominal aortic aneurysm studies. *Journal of biomechanics, 40*(2), 289-295. doi:https://doi.org/10.1016/j.jbiomech.2006.01.010

Hoylaerts, M., Rijken, D. C., Lijnen, H. R., & Collen, D. (1982). Kinetics of the activation of plasminogen by human tissue plasminogen activator. Role of fibrin. *Journal of Biological Chemistry, 257*(6), 2912-2919.

Jackson, S. P. (2007). The growing complexity of platelet aggregation. *Blood, 109*(12), 5087-5095. doi:10.1182/blood-2006-12-027698

Jackson, S. P. (2007). The growing complexity of platelet aggregation. *Blood, 109*(12), 5087-5095.

Jantunen, E., Hänninen, A., Naukkarinen, A., Vornanen, M., & Lahtinen, R. (1994). Gray platelet syndrome with splenomegaly and signs of extramedullary hematopoiesis: a case report with review of the literature. *Am J Hematol, 46*(3), 218-224. Retrieved from https://www.ncbi.nlm.nih.gov/pubmed/8192152

Johnson, S., Duffy, S., Gunning, G., Gilvarry, M., McGarry, J. P., & McHugh, P. E. (2017). Review of Mechanical Testing and Modelling of Thrombus Material for Vascular Implant and Device Design. *Annals of biomedical engineering, 45*(11), 2494-2508. doi:10.1007/s10439-017-1906-5

Kahr, W. H., Lo, R. W., Li, L., Pluthero, F. G., Christensen, H., Ni, R., . . . Gross, P. L. (2013). Abnormal megakaryocyte development and platelet function in Nbeal2(-/-) mice. *Blood, 122*(19), 3349-3358. doi:10.1182/blood-2013-04-499491

Khalil, I. S. M., Tabak, A. F., Sadek, K., Mahdy, D., Hamdi, N., & Sitti, M. (2017). Rubbing Against Blood Clots Using Helical Robots: Modeling and In Vitro Experimental Validation. *IEEE Robotics and Automation Letters, 2*(2), 927-934. doi:10.1109/LRA.2017.2654546

Kim, D., Bresette, C., Liu, Z., & Ku, D. N. (2019). Occlusive thrombosis in arteries. *APL bioengineering, 3*(4), 041502-041502. doi:10.1063/1.5115554

Kobayashi, S., Sekar, K., & Ku, D. (2016). occlusive thrombus growth at high shear rates: comparison of whole blood and platelet rich plasma at constant pressure: br02. *Journal of Thrombosis and Haemostasis, 14*, 6-7.

Ku, D. N., & Flannery, C. J. (2007). Development of a flow-through system to create occluding thrombus. *Biorheology, 44*(4), 273-284.

Kwon, O. K., Lee, K. J., Han, M. H., Oh, C.-W., Han, D. H., & Koh, Y. C. (2002). Intraarterially Administered Abciximab as an Adjuvant Thrombolytic Therapy: Report of Three Cases. *American Journal of Neuroradiology, 23*(3), 447. Retrieved from http://www.ajnr.org/content/23/3/447.abstract

Lam, W. A., Chaudhuri, O., Crow, A., Webster, K. D., Li, T.-D., Kita, A., . . . Fletcher, D. A. (2011). Mechanics and contraction dynamics of single platelets and implications for clot stiffening. *Nature Materials, 10*(1), 61-66. doi:10.1038/nmat2903

Lefkowitz, J. B. (2008). Coagulation pathway and physiology. *An algorithmic approach to hemostasis testing, 1*(1), 3-12.

Liu, Y., Zheng, Y., Reddy, A. S., Gebrezgiabhier, D., Davis, E., Cockrum, J., . . . Savastano, L. E. (2020). Analysis of human emboli and thrombectomy forces in large-vessel occlusion stroke. 1. doi:10.3171/2019.12.Jns192187

Liu, Z. (2020). *Multiscale Simulation of Molecular and Cellular Blood Flow and Clotting: from nano-drug delivery to arterial thrombosis.* (Doctoral). Georgia Institute of Technology, Proquest Dissertations and Theses Global.

Marder, V. J. (2011). Historical perspective and future direction of thrombolysis research: the re-discovery of plasmin. *J Thromb Haemost, 9 Suppl 1*, 364-373. doi:10.1111/j.1538-7836.2011.04370.x

Marder, V. J., Chute, D. J., Starkman, S., Abolian, A. M., Kidwell, C., Liebeskind, D., . . . Saver, J. L. (2006). Analysis of thrombi retrieved from cerebral arteries of patients with acute ischemic stroke. *Stroke, 37*(8), 2086-2093. doi:10.1161/01.Str.0000230307.03438.94

Martinez de Lizarrondo, S., Gakuba, C., Herbig, B. A., Repesse, Y., Ali, C., Denis, C. V., . . . Gauberti, M. (2017). Potent Thrombolytic Effect of N-Acetylcysteine on Arterial Thrombi. *Circulation, 136*(7), 646-660. doi:10.1161/circulationaha.117.027290

Matsuo, O., Rijken, D. C., & Collen, D. (1981a). Comparison of the relative fibrinogenolytic, fibrinolytic and thrombolytic properties of tissue plasminogen activator and urokinase in vitro. *Thromb Haemost, 45*(3), 225-229.

Matsuo, O., Rijken, D. C., & Collen, D. (1981b). Thrombolysis by human tissue plasminogen activator and urokinase in rabbits with experimental pulmonary embolus. *Nature, 291*(5816), 590-591. doi:10.1038/291590a0

Mauri, L., Kereiakes, D. J., Yeh, R. W., Driscoll-Shempp, P., Cutlip, D. E., Steg, P. G., . . . Massaro, J. M. (2014). Twelve or 30 months of dual antiplatelet therapy after drug-eluting stents. *N Engl J Med, 371*(23), 2155-2166. doi:10.1056/NEJMoa1409312

McCarty, W. J., Luan, A., Siddiqui, M., Hansen, B. C., Masuda, K., & Sah, R. L. (2011). Biomechanical properties of mixtures of blood and synovial fluid. *J Orthop Res, 29*(2), 240-246. doi:10.1002/jor.21209

Mehrabadi, M., Casa, L. D., Aidun, C. K., & Ku, D. N. (2016). A predictive model of high shear thrombus growth. *Annals of biomedical engineering, 44*(8), 2339-2350.

Moake, J. L., Turner, N. A., Stathopoulos, N. A., Nolasco, L., & Hellums, J. D. (1988). Shear-induced platelet aggregation can be mediated by vWF released from platelets, as well as by exogenous large or unusually large vWF multimers, requires adenosine diphosphate, and is resistant to aspirin. *Blood, 71*(5), 1366-1374. Retrieved from https://www.ncbi.nlm.nih.gov/pubmed/3258770

Mokin, M., Waqas, M., Fifi, J., De Leacy, R., Fiorella, D., Levy, E. I., . . . Mocco, J. (2020). Clot perviousness is associated with first pass success of aspiration thrombectomy in the COMPASS trial. *Journal of NeuroInterventional Surgery*, neurintsurg-2020-016434. doi:10.1136/neurintsurg-2020-016434

Mozaffarian, D., Benjamin, E. J., Go, A. S., Arnett, D. K., Blaha, M. J., Cushman, M., . . . Turner, M. B. (2015). Heart disease and stroke statistics--2015 update: a report from the American Heart Association. *Circulation, 131*(4), e29-322. doi:10.1161/cir.0000000000000152

Muia, J., Zhu, J., Gupta, G., Haberichter, S. L., Friedman, K. D., Feys, H. B., . . . Sadler, J. E. (2014). Allosteric activation of ADAMTS13 by von Willebrand factor. *Proc Natl Acad Sci U S A, 111*(52), 18584-18589. doi:10.1073/pnas.1413282112

Narins, C. R., & Topol, E. J. (1997). Attention shifts to the white clot. *The Lancet, 350*, SIII2. doi:10.1016/S0140-6736(97)90035-0

Nurden, A. T., & Nurden, P. (2007). The gray platelet syndrome: clinical spectrum of the disease. *Blood Rev, 21*(1), 21-36. doi:10.1016/j.blre.2005.12.003

Para, A. N., Bark, D., Lin, A., & Ku, D. (2011). Rapid platelet accumulation leading to thrombotic occlusion. *Annals of biomedical engineering, 39*(7), 1961-1971.

Para, A. N., & Ku, D. N. (2013). A low-volume, single pass in-vitro system of high shear thrombosis in a stenosis. *Thromb Res, 131*(5), 418-424. doi:10.1016/j.thromres.2013.02.018

Perez-Vilar, J., & Hill, R. L. (1999). The structure and assembly of secreted mucins. *J Biol Chem, 274*(45), 31751-31754. doi:10.1074/jbc.274.45.31751

Pettersson, K., & Bergstrand, H. (2003). The antiatherogenic effect of DiNAC: experimental findings supporting immunomodulation as a new treatment for atherosclerosis related diseases. *Cardiovasc Drug Rev, 21*(2), 119-132. doi:10.1111/j.1527-3466.2003.tb00110.x

Piebalgs, A., Gu, B., Roi, D., Lobotesis, K., Thom, S., & Xu, X. Y. (2018). Computational Simulations of Thrombolytic Therapy in Acute Ischaemic Stroke. *Scientific Reports, 8*(1), 15810. doi:10.1038/s41598-018-34082-7

Pikija, S., Magdic, J., Trkulja, V., Unterkreuter, P., Mutzenbach, J. S., Novak, H. F., . . . Sellner, J. (2016). Intracranial Thrombus Morphology and Composition Undergoes Time-Dependent Changes in Acute Ischemic Stroke: A CT Densitometry Study. *International journal of molecular sciences, 17*(11), 1959. doi:10.3390/ijms17111959

Prabhakaran, S., Ruff, I., & Bernstein, R. A. (2015). Acute stroke intervention: a systematic review. *Jama, 313*(14), 1451-1462. doi:10.1001/jama.2015.3058

Prowse, C., Pepper, D., & Dawes, J. (1982). Prevention of the platelet alpha-granule release reaction by membrane-active drugs. *Thrombosis research, 25*(3), 219-227. doi:https://doi.org/10.1016/0049-3848(82)90241-9

Rack, K., Huck, V., Hoore, M., Fedosov, D. A., Schneider, S. W., & Gompper, G. (2017). Margination and stretching of von Willebrand factor in the blood stream enable adhesion. *Scientific Reports, 7*(1). doi:10.1038/s41598-017-14346-4

Raychev, R., & Saver, J. L. (2012). Mechanical thrombectomy devices for treatment of stroke. *Neurology. Clinical practice, 2*(3), 231-235. doi:10.1212/CPJ.0b013e31826af206

Riha, P., Wang, X., Liao, R., & Stoltz, J. F. (1999). Elasticity and fracture strain of whole blood clots. *Clinical Hemorheology and Microcirculation, 21*, 45-49.

Ruggeri, Z. M., Orje, J. N., Habermann, R., Federici, A. B., & Reininger, A. J. (2006). Activation-independent platelet adhesion and aggregation under elevated shear stress. *Blood, 108*(6), 1903-1910.

Ryan, E. A., Mockros, L. F., Weisel, J. W., & Lorand, L. (1999). Structural origins of fibrin clot rheology. *Biophys J, 77*(5), 2813-2826. doi:10.1016/s0006-3495(99)77113-4

Sakariassen, K. S., Houdijk, W. P., Sixma, J. J., Aarts, P. A., & de Groot, P. G. (1983). A perfusion chamber developed to investigate platelet interaction in flowing blood with human vessel wall cells, their extracellular matrix, and purified components. *The Journal of laboratory and clinical medicine, 102*(4), 522-535.

Santoro, S. A. (1981). Adsorption of von Willebrand factor/factor VIII by the genetically distinct interstitial collagens. *Thrombosis research, 21*(6), 689-693.

Santos Emilie, M. M., Marquering Henk, A., den Blanken Mark, D., Berkhemer Olvert, A., Boers Anna, M. M., Yoo Albert, J., . . . Csizmadia, M. (2016). Thrombus Permeability Is Associated With Improved Functional Outcome and Recanalization in Patients With Ischemic Stroke. *Stroke, 47*(3), 732-741. doi:10.1161/STROKEAHA.115.011187

Savage, B., Ginsberg, M. H., & Ruggeri, Z. M. (1999). Influence of Fibrillar Collagen Structure on the Mechanisms of Platelet Thrombus Formation Under Flow. *Blood, 94*(8), 2704-2715. doi:10.1182/blood.V94.8.2704.420k41_2704_2715

Saver, J. L., Goyal, M., Bonafe, A., Diener, H.-C., Levy, E. I., Pereira, V. M., . . . Jahan, R. (2015). Stent-Retriever Thrombectomy after Intravenous t-PA vs. t-PA Alone in Stroke. *New England Journal of Medicine, 372*(24), 2285-2295. doi:10.1056/NEJMoa1415061

Schmitt, C., Hadj Henni, A., & Cloutier, G. (2011). Characterization of blood clot viscoelasticity by dynamic ultrasound elastography and modeling of the rheological behavior. *J Biomech, 44*(4), 622-629. doi:10.1016/j.jbiomech.2010.11.015

Schneider, S. W., Nuschele, S., Wixforth, A., Gorzelanny, C., Alexander-Katz, A., Netz, R. R., & Schneider, M. F. (2007). Shear-induced unfolding triggers adhesion of von

Willebrand factor fibers. *Proceedings of the National Academy of Sciences, 104*(19), 7899-7903. doi:10.1073/pnas.0608422104

Silver, M. D., Baroldi, G., & Mariani, F. (1980). The relationship between acute occlusive coronary thrombi and myocardial infarction studied in 100 consecutive patients. *Circulation, 61*(2), 219-227. doi:10.1161/01.CIR.61.2.219

Slaboch, C. L., Alber, M. S., Rosen, E. D., & Ovaert, T. C. (2012). Mechano-rheological properties of the murine thrombus determined via nanoindentation and finite element modeling. *J Mech Behav Biomed Mater, 10*, 75-86. doi:10.1016/j.jmbbm.2012.02.012

Soejima, K., Nakamura, H., Hirashima, M., Morikawa, W., Nozaki, C., & Nakagaki, T. (2006). Analysis on the Molecular Species and Concentration of Circulating ADAMTS13 in Blood. *The Journal of Biochemistry, 139*(1), 147-154. doi:10.1093/jb/mvj013

Stamler, J., Neaton, J. D., & Wentworth, D. N. (1989). Blood pressure (systolic and diastolic) and risk of fatal coronary heart disease. *Hypertension, 13*(5).

Sturgeon, S. A., Jones, C., Angus, J. A., & Wright, C. E. (2006). Adaptation of the Folts and electrolytic methods of arterial thrombosis for the study of anti-thrombotic molecules in small animals. *J Pharmacol Toxicol Methods, 53*(1), 20-29. doi:10.1016/j.vascn.2005.06.006

Tasci, T. O., Disharoon, D., Schoeman, R. M., Rana, K., Herson, P. S., Marr, D. W. M., & Neeves, K. B. (2017). Enhanced Fibrinolysis with Magnetically Powered Colloidal Microwheels. *Small, 13*(36), 1700954. doi:10.1002/smll.201700954

Teng, Z., Feng, J., Zhang, Y., Huang, Y., Sutcliffe, M. P., Brown, A. J., . . . Lu, Q. (2015). Layer- and Direction-Specific Material Properties, Extreme Extensibility and Ultimate Material Strength of Human Abdominal Aorta and Aneurysm: A Uniaxial Extension Study. *Ann Biomed Eng, 43*(11), 2745-2759. doi:10.1007/s10439-015-1323-6

Tersteeg, C., de Maat, S., De Meyer, S. F., Smeets, M. W., Barendrecht, A. D., Roest, M., . . . Maas, C. (2014). Plasmin cleavage of von Willebrand factor as an emergency bypass for ADAMTS13 deficiency in thrombotic microangiopathy. *Circulation, 129*(12), 1320-1331. doi:10.1161/circulationaha.113.006727

The GUSTO Angiographic Investigators. (1993). The effects of tissue plasminogen activator, streptokinase, or both on coronary-artery patency, ventricular function, and survival after acute myocardial infarction. *N Engl J Med, 329*(22), 1615-1622. doi:10.1056/nejm199311253292204

The GUSTO Investigators. (1993). An international randomized trial comparing four thrombolytic strategies for acute myocardial infarction. *N Engl J Med, 329*(10), 673-682. doi:10.1056/nejm199309023291001

Uchida, Y., Uchida, Y., Sakurai, T., Kanai, M., Shirai, S., & Morita, T. (2011). Characterization of coronary fibrin thrombus in patients with acute coronary syndrome using dye-staining angioscopy. *Arterioscler Thromb Vasc Biol, 31*(6), 1452-1460. doi:10.1161/atvbaha.110.221671

Upton, G., & Cook, I. (2006). *A Dictionary of Statistics* (2e ed.). Oxford, United Kingdom: Oxford Unversity Press.

van Dam, E. A., Dams, S. D., Peters, G. W., Rutten, M. C., Schurink, G. W., Buth, J., & van de Vosse, F. N. (2006). Determination of linear viscoelastic behavior of abdominal aortic aneurysm thrombus. *Biorheology, 43*(6), 695-707.

Wagberg, M., Jansson, A. H., Westerlund, C., Ostlund-Lindqvist, A. M., Sarnstrand, B., Bergstrand, H., & Pettersson, K. (2001). N,N'-diacetyl-L-cystine (DiNAC), the disulphide dimer of N-acetylcysteine, inhibits atherosclerosis in WHHL rabbits: evidence for immunomodulatory agents as a new approach to prevent atherosclerosis. *J Pharmacol Exp Ther, 299*(1), 76-82.

Wechsler, L. R. (2011). Intravenous Thrombolytic Therapy for Acute Ischemic Stroke. *New England Journal of Medicine, 364*(22), 2138-2146. doi:10.1056/NEJMct1007370

Wei, W., Dong, C., Morabito, M., Cheng, X., Zhang, X. F., Webb, E. B., & Oztekin, A. (2018). Coarse-Grain Modeling of Shear-Induced Binding between von Willebrand Factor and Collagen. *Biophysical journal, 114*(8), 1816-1829.

Wellings, P. J., & Ku, D. N. (2012). Mechanisms of platelet capture under very high shear. *Cardiovascular Engineering and Technology, 3*(2), 161-170. doi:10.1007/s13239-012-0086-6

Whitaker, S. (1986). Flow in porous media I: A theoretical derivation of Darcy's law. *Transport in Porous Media, 1*(1), 3-25. doi:10.1007/BF01036523

Whiteheart, S. W. (2011). Platelet granules: surprise packages. *Blood, 118*(5), 1190-1191. doi:10.1182/blood-2011-06-359836

Wootton, D. M., Markou, C. P., Hanson, S. R., & Ku, D. N. (2001). A Mechanistic Model of Acute Platelet Accumulation in Thrombogenic Stenoses. *Annals of biomedical engineering, 29*(4), 321-329. doi:10.1114/1.1359449

Wufsus, A. R., Macera, N. E., & Neeves, K. B. (2013). The hydraulic permeability of blood clots as a function of fibrin and platelet density. *Biophys J, 104*(8), 1812-1823. doi:10.1016/j.bpj.2013.02.055

Xie, H., Kim, K., Aglyamov, S. R., Emelianov, S. Y., O'Donnell, M., Weitzel, W. F., . . . Rubin, J. M. (2005). Correspondence of ultrasound elasticity imaging to direct mechanical measurement in aging DVT in rats. *Ultrasound Med Biol, 31*(10), 1351-1359. doi:10.1016/j.ultrasmedbio.2005.06.005

Xu, J., Murphy, S. L., Kochanek, K. D., & Arias, E. (2020). Mortality in the United States, 2018. *NCHS Data Brief, No. 355*.

Yago, T., Lou, J., Wu, T., Yang, J., Miner, J. J., Coburn, L., . . . McIntire, L. V. (2008). Platelet glycoprotein Ibα forms catch bonds with human WT vWF but not with type 2B von Willebrand disease vWF. *The Journal of clinical investigation, 118*(9), 3195-3207.

Yago, T., Lou, J., Wu, T., Yang, J., Miner, J. J., Coburn, L., . . . Zhu, C. (2008). Platelet glycoprotein Ibalpha forms catch bonds with human WT vWF but not with type 2B von Willebrand disease vWF. *J Clin Invest, 118*(9), 3195-3207. doi:10.1172/jci35754

Yang, L., Yihao, Z., Adithya, S. R., Daniel, G., Evan, D., Joshua, C., . . . Luis, E. S. (2020). Analysis of human emboli and thrombectomy forces in large-vessel occlusion stroke. *Journal of Neurosurgery JNS*, 1-9. doi:10.3171/2019.12.JNS192187

Yao, X., Dong, Q., Song, Y., Wang, Y., Deng, Y., & Li, Y. (2014). Thrombelastography Maximal Clot Strength Could Predict One-Year Functional Outcome in Patients with Ischemic Stroke. *Cerebrovascular Diseases, 38*(3), 182-190. doi:10.1159/000365652

Yeo, L. L. L., Bhogal, P., Gopinathan, A., Cunli, Y., Tan, B., & Andersson, T. (2019). Why Does Mechanical Thrombectomy in Large Vessel Occlusion Sometimes Fail? *Clinical Neuroradiology, 29*(3), 401-414. doi:10.1007/s00062-019-00777-1